Effects of Loading Path on the Biaxial Fatigue Behavior of Thin Walled Carbon Fiber Composite Tubes

by

Dale William Oleschuk

A Thesis submitted to the Faculty of Graduate Studies of

The University of Manitoba

in partial fulfillment of the requirements of the degree of

MASTER OF SCIENCE

Department of Mechanical Engineering

University of Manitoba

Winnipeg

Abstract

Composite structures are subjected to multi-axial fatigue loads while in service. The objective of this thesis is to study the effect of load path (sequence of application of load) on biaxial fatigue behavior of multi-directional composites. The fatigue behavior of thin walled $[\pm 45]_{2s}$ graphite fiber composite tube was experimentally studied under uniaxial and biaxial loading. The sequence of application of, and the phase difference between the tensile and torsional loads was varied. While an in-phase torque, superposed on to the tensile load, extended the fatigue life, an out-of-phase torque, superposed onto the tensile load, reduced the fatigue life, with respect to uniaxial fatigue life. An out-of-phase torque applied prior to the tensile load had the most impact on the fatigue life, when compared to the torque applied after the tensile load. These results establish the effect of load path on the fatigue life of composites under biaxial loading.

Acknowledgments

I would like to thank the following organizations and people who assisted me during my studies:

- Magellan Aerospace, Winnipeg for their financial support and flexible work hours
- Composites Innovation Centre for their assistance in manufacturing the ASTM-D-7078 samples and loaning the test fixture for testing
- Stress Engineering Services Inc. for loaning their thermocouple card
- University of Manitoba Mechanical and Manufacturing Engineering Department's technical staff
- University of Manitoba Graduate Studies staff for their administrative assistance
- Fellow graduate students Alastair Komus, Amir Asadi, and Darryl Stoyko for passing on their knowledge
- Dr. Meera Singh and Dr. Raghavan Jayaraman for agreeing to be my co-advisors and providing invaluable assistance
- Finally, to my family and friends for their support and understanding

Contents

List of Figures **vi**

List of Tables **xii**

Nomenclature **xiii**

1 Introduction **1**

2 Literature Review **5**

2.1 Summary of Literature Review and Thesis Objectives 16

3 Experimental Details **18**

3.1 Samples 18

3.1.1 Laminate Layup 18

3.1.2 Material 19

3.1.3 Geometry 19

3.1.4 Manufacture 23

3.2 Test Equipment 24

3.2.1 Load Frames 25

3.2.2 Strain Measurement 29

3.3 Test Procedure 32

3.3.1 Quasi-Static Testing 32

3.3.2 Laminate Properties 34
3.3.3 Fatigue Testing 35

4 Results and Discussion 39

4.1 Lamina Properties 39
4.1.1 Longitudinal Lamina Properties 40
4.1.2 Transverse Lamina Properties 41
4.1.3 Lamina Shear Properties 42
4.2 End Effects and Design Parameters 44
4.2.1 Effect of Specimen Geometry and Clamped End Constraints . 44
4.3 Quasi-Static Test Results 48
4.3.1 Tension Test Results 48
4.3.2 Type V Torsion Loading 54
4.3.3 Type I Combined Tension/Torsion Test Results 72
4.4 Fatigue Test Results 76
4.5 Uniaxial Fatigue Data 84
4.5.1 Type IV - Uniaxial Tension Fatigue Loading 84
4.5.2 Type V - Uniaxial Torsion Fatigue Loading 90
4.6 Biaxial Fatigue Data 98
4.6.1 Type I - Biaxial Tension-Torsion Fatigue Loading 98
4.6.2 Type II - Biaxial Out-of-Phase Tension-Torsion Fatigue Loading 104
4.6.3 Type III - Biaxial Out-of-Phase Torsion-Tension Fatigue Loading 110
4.7 Discussion 117

5 Conclusions 124

5.1 Summary 125
5.2 Final Conclusions 127
5.3 Recommended Future Work 128

Appendices **129**

A Failure Envelope Calculations **129**

A.1

Determination of Failure Envelope for $[\pm 45]_{2s}$ Laminate 130

A.1.1 Laminate Properties 130

A.1.2 Failure Envelope 137

A.1.3 Failure Mode and Loads for Uniaxial Loading of 45° ply and −45° ply 146

A.1.4 Failure Mode and Loads for Biaxial Loading of 45° ply and −45° ply 147

B Incremental Load Analysis **150**

Bibliography **152**

List of Figures

2.1 Fatigue life diagram for unidirectional composites for axial tension-tension loading (Figure 1 from Ref. [1]) — Image removed due to copyright 6

2.2 Fatigue life diagram for unidirectional carbon-epoxy (a) and high-modulus carbon-epoxy (b) loaded in cyclic tension along fibers (Figure 2–3 from Ref. [1]) — Image removed due to copyright 7

2.3 Phase shift example 9

2.4 Comparison of failure torques under torsion and tension-torsion (Figure 6 from Ref. [2]) — Image removed due to copyright 11

2.5 Comparison of failure twist angles under torsion and tension-torsion (Figure 7 from Ref. [2]) — Image removed due to copyright 11

2.6 Torque versus twist angle curves of CFRP and GFRP under a constant tensile axial load (0, 20 kN) (Figure 3 from Ref. [3]) — Image removed due to copyright 12

2.7 Torque versus twist angle under cyclic torsion fatigue tests (Figure 5 from Ref. [3]) — Image removed due to copyright 12

2.8 Torsional fatigue life of unidirectional CFRP and GFRP under a constant axial tensile load. Fatigue life is defined as 10% or 20% reduction of torsional rigidity (Figure 8 from Ref. [3]) — Image removed due to copyright 13

2.9 Fatigue life curves for glass fiber in bending/torsion (Figure 11 from Ref. [4]) — Image removed due to copyright 14
2.10 Three types of cyclic load path (Figure 2 from Ref. [5]) — Image removed due to copyright 15

3.1 Biaxial fatigue test sample 21
3.2 $[0]_8$ samples used in tension testing to measure longitudinal properties 21
3.3 $[90]_{16}$ samples used in tension testing to measure transverse properties 22
3.4 $[0\backslash 90]_{6s}$ sample used in shear testing to measure the in-plane shear properties 22
3.5 Instron 8562 servo-electric load frame 26
3.6 ASTM-D-7078 shear test fixture 27
3.7 As designed test fixture 28
3.8 As built specimen holding fixture 29
3.9 ARAMIS Camera Set-up (showing supplemental lights required with sample loaded in Instron 8822 load frame) 30
3.10 Vishay S7000 DAQ 31
3.11 Lamina coordinate system 32
3.12 Load Path Visualization for Type I-III 36
3.13 Failure envelope for first ply failure 37
3.14 Failure envelope for first ply failure denoted ABCD 38

4.1 τ vs. γ for Sample 5 of ASTM-D-7078 [6] testing 42
4.2 Distribution in ϵ_x along the gage length of the test specimen at various times during quasi-static loading 45
4.3 Distribution in ϵ_y along the gage length of the test specimen at various times during quasi-static loading 45

4.4 Samples 16 and 21 showing gage section failure with and without complete separation . . . 47

4.5 Sample 16 showing crack growth in the gage section during fatigue testing . . . 47

4.6 Stress vs. strain plot of Sample 20 loaded in quasi-static tension to failure . . . 49

4.7 Stress vs. strain plot of sample 20 in quasi-static tension until debonding of the strain gage . . . 50

4.8 Failure surface of Sample 20 . . . 50

4.9 Sample 20 ϵ_y just before failure during quasi-static tension test . . . 51

4.10 Sample 20 ϵ_{xy} just before failure during quasi-static tension test . . . 52

4.11 Failure completion at the chamfered end of the steel plug in Sample 9 53

4.12 Stress vs. Strain plot of Sample 7 in pure torsion . . . 55

4.13 Exterior and interior surfaces of Sample 7 . . . 55

4.14 Sample 7 ϵ_{xy} at peak strain prior to failure . . . 56

4.15 Sample 7 ϵ_y at peak strain prior to failure . . . 57

4.16 Linear position change of 1018 steel during rotation . . . 58

4.17 A schematic of the Instron 8822 load frame . . . 60

4.18 The load, torque, cross-head displacement, and angle of twist recorded during torque loading of a 1018 steel specimen with the rotary actuator under load control and linear actuator under position control . . . 61

4.19 The strains recorded during during torque loading of a 1018 steel specimen with the rotary actuator under load control and linear actuator under position control . . . 62

4.20 The load, torque, cross-head displacement, and angle of twist recorded during torque loading of a 1018 steel specimen with the rotary actuator under load control and linear actuator under load control . . . 63

4.21 The strains recorded during torque loading of a 1018 steel specimen with the rotary actuator under load control and linear actuator under load control 64
4.22 The load, torque, cross-head displacement, and angle of twist recorded during tension loading of a 1018 steel specimen with the rotary actuator under load control and linear actuator under load control 66
4.23 The strains recorded during tension loading of a 1018 steel specimen with the rotary actuator under load control and linear actuator under load control 67
4.24 Axial cross-head position and torque during quasi-static testing of Sample 7 68
4.25 A schematic representing machine coupling between the rotary and linear actuators 69
4.26 The axial load and the axial strain measured on 1018 Steel sample due to machine coupling during torque loading 70
4.27 A free body diagram for the 1018 steel sample illustrating the introduction of axial compressive load due to machine coupling 71
4.28 Shear and normal stress-strain plots for sample 9 under combined tension-torsion loading 74
4.29 Fractured halves of Sample 9 highlighting the fracture modes 74
4.30 Comparison of experimental and predicted stress-strain curves, for Sample 9 subjected to combined tension - torsion quasi-static loading 75
4.31 S-N curve for Type I, II, III, IV, and V loading 78
4.32 Variation of Young's Modulus, E_{yy}, during fatigue testing 80
4.33 Variation of shear modulus, G_{xy}, during fatigue testing 81
4.34 Fatigue sample failures grouped by loading type 82
4.35 Examples of failure modes 83

4.36 Type IV test levels overlaid on Sample 20 stress vs. strain graph . . . 84
4.37 Sample 27 (Type IV [50% of σ_{yy}^{max}]) hysteresis 86
4.38 Sample 30 (Type IV [60% of σ_{yy}^{max}]) hysteresis 87
4.39 Sample 29 (Type IV [75% of σ_{yy}^{max}]) hysteresis 88
4.40 Samples failed under tensile fatigue (Type IV loading) 89
4.41 Type V test levels overlaid on Sample 7 stress vs. strain graph 90
4.42 Sample 28 position plotted as a function of load applied during the first two loading cycles 93
4.43 Sample 28 (Type V [75% of τ_{xy}^{max}]) hysteresis 94
4.44 Sample 31 (Type V [80% of τ_{xy}^{max}]) hysteresis 95
4.45 Sample 32 (Type V [90% of τ_{xy}^{max}]) hysteresis 96
4.46 Samples failed under torsional fatigue (Type V Loading) 97
4.47 Tube failure under shear load 97
4.48 Sample 12 (Type I [75% of σ_{yy}^{max} and τ_{xy}^{max}]) hysteresis 100
4.49 Sample 13 (Type I [60% of σ_{yy}^{max} and τ_{xy}^{max}]) hysteresis 101
4.50 Sample 14 (Type I [50% of σ_{yy}^{max} and τ_{xy}^{max}]) hysteresis 102
4.51 Samples failed after in-phase tension-torsion fatigue (Type I loading) 103
4.52 Sample 21 (Type II [75% of σ_{yy}^{max} then 75% of τ_{xy}^{max}]) hysteresis 105
4.53 Sample 16 (Type II [60% of σ_{yy}^{max} then 60% of τ_{xy}^{max}]) hysteresis 106
4.54 Sample 17 (Type II [50% of σ_{yy}^{max} then 50% of τ_{xy}^{max}]) hysteresis 107
4.55 Sample 25 (Type II [50% of σ_{yy}^{max} then 50% of τ_{xy}^{max}]) hysteresis 108
4.56 Samples failed under out-of-phase tension-torsion fatigue (Type II loading) 109
4.57 Sample 23 (Type III [75% of τ_{yy}^{max} then 75% of σ_{xy}^{max}]) hysteresis . . . 111
4.58 Sample 19 (Type III [60% of τ_{yy}^{max} then 60% of σ_{xy}^{max}]) hysteresis . . . 112
4.59 Sample 22 (Type III [40% of τ_{yy}^{max} then 40% of σ_{xy}^{max}]) hysteresis . . . 113
4.60 Sample 18 (Type III [50% of τ_{yy}^{max} then 50% of σ_{xy}^{max}]) hysteresis . . . 114

4.61 Sample 24 (Type III [40% of τ_{yy}^{max} then 40% of σ_{xy}^{max}]) hysteresis . . . 115

4.62 Samples failed under out-of-phase torsion-tension fatigue (Type III loading) 116

List of Tables

3.1 Properties of lamina made up of Grafil Inc. Pyrofil^{TM} HR40 12K carbon fibers and Newport 301 resin 19
3.2 Sample geometries used in previous studies (Figure 2 of Ref. [4], Figure 1 of Ref. [5], and Figure 1 of Ref. [7]) — Images removed due to copyright 20
3.3 List of all samples used 24
3.4 Samples Used for Biaxial Fatigue Tests 36
3.5 Samples Used for Uniaxial Fatigue Tests 37

4.1 Lamina longitudinal properties 40
4.2 Lamina transverse properties 41
4.3 Lamina Shear Values 43
4.4 Quasi-static test results for laminate tube samples 48
4.5 Fatigue Results of all Tube Samples 77

Nomenclature

α Ratio of axial stress to shear stress

ν_{12} Poisson's ratio in material 12 plane

σ Axial stress

τ Shear stress

CV Coefficient of variation

E_1 Young's Modulus in material 1 direction

E_2 Young's Modulus in material 2 direction

G_{12} Shear modulus in material 12 plane

G_a Shear modulus calculated on the front side during ASTM 7078 testing

G_b Shear modulus calculated on the back side during ASTM 7078 testing

S_{12}^{+} Shear stress at failure in positive material 12 plane

S_{12}^{-} Shear stress at failure in negative material 12 plane

S_1^{+} Tensile stress at failure in material 1 direction

S_1^{-} Compressive stress at failure in material 1 direction

S_2^{+} Tensile stress at failure in material 2 direction

S_2^- Compressive stress at failure in material 2 direction

S_{n-1} Standard deviation

$[\overline{Q}]$ Stiffness matrix of a ply terms of the global x-y coordinates

$[\overline{Q}^{\theta}]$ Stiffness matrix of a ply in terms of the global x-y coordinates where the 1-2 material coordinates is at an angle θ to the global x-y coordinates

$[T_\epsilon]$ Transformation matrix used to transform in-plane strain

$[T_\sigma]$ Transformation matrix used to transform in-plane stresses

$[Q]$ Stiffness matrix of a ply terms of the material 1-2 coordinates

$[Q^\theta]$ Stiffness matrix of a ply terms of the material 1-2 coordinates that is at an angle θ to the global x-y coordinates

ϵ_x° Strain in the global x direction at the reference plane

ϵ_y° Strain in the global y direction at the reference plane

γ_z° Strain in the global xy direction at the reference plane

κ_{xy} Curvature in the global xy direction of the reference plane

κ_x Curvature in the global x direction of the reference plane

κ_y Curvature in the global y direction of the reference plane

A_{ij} Stiffness matrix terms linking in-plane forces to in-plane deformations

a_{ij} Compliance matrix terms linking in-plane forces to in-plane deformations

B_{ij} Stiffness matrix terms linking in-plane forces to curvatures and moments to in-plane deformations

b_{ij}	Compliance matrix terms linking in-plane forces to curvatures and moments to in-plane deformations
D_{ij}	Stiffness matrix terms linking moments to curvatures
d_{ij}	Compliance matrix terms linking moments to curvatures
M_{xy}	Moment per unit length applied in the global xy direction
M_x	Moment per unit length applied in the global x direction
M_y	Moment per unit length applied in the global y direction
N_{xy}	Force per unit length applied in the global xy direction
N_x	Force per unit length applied in the global x direction
N_y	Force per unit length applied in the global y direction
P	Load applied to sample in global y direction
T	Torsion applied to sample in global xy direction
λ_1	Stress ratio
λ_2	Stress ratio
$\sigma_{1,a}$	Amplitude of normal stress in material 1 direction
$\sigma_{2,a}$	Amplitude of normal stress in material 2 direction
$\sigma_{6,a}$	Amplitude of shear stress in material 6 direction
D_i	Fatigue sample inside diameter
l	Fatigue sample overall length
t	Fatigue sample thickness

Chapter 1

Introduction

A composite is made of two or more dissimilar materials. One of the earlier examples of a composite is bricks, built by mixing straw with mud and baked in the sun. These early composite bricks were used as a building material. In today's world, composites are still used as a building material for beams and walls made with concrete mixed with long steel rods (rebar). A composite used in engineering applications typically consists of a matrix and a reinforcement. In the previous examples the fiber would be the straw or rebar, and the matrix would be the mud or concrete.

Composites can be of four different types: chopped or short fiber composites, continuous fiber composites, woven fiber composites, and hybrid composites. Chopped fiber composites are composites where the fiber is short; the fiber length divided by the fiber diameter is less than 1000. Continuous fiber composites are composites where the fiber is long; the fiber length divided by the fiber diameter is greater than 1000. Woven fiber composites are composites where continuous fibers have been woven together. Hybrid composites are any composites that have been formed by mixing any two of the previously described composites.

In the case of continuous fiber composites, thin sheets of fibers oriented within a matrix are stacked together and laminated to get the composite. This study is focused on non-woven continuous fiber multidirectional composite laminates. Each individual sheet is referred to as a ply or lamina. The group of lamina stacked together is called the laminate. The laminate properties can be tailored by orientating the fibers in various plies in a specific direction to maximize the load that the fibers share while the matrix keeps everything together and protects the fibers.

In the aerospace, automotive, and industrial sectors, composites have been made with a variety of fibers and matrixes. Fibers have been made from glass, carbon, aramid, ceramics, flax, and hemp. These fibers have been added to a number of different matrix materials: thermoset resins such as polyester, vinyl ester, and epoxy; and thermoplastic resins such as polyethylene, polystyrene, polypropylene, and polyetheretherketone. This study is focused on epoxy resin reinforced with graphite fibers.

Once a laminate is built it is possible to calculate the strength of the composite by analyzing the component parts and determining the maximum load that the composite can take without failure. When a load is repeatedly applied, the composite is said to be under fatigue loading. Calculating the number of loading cycles that it would take for the composite to fail for a given load amplitude is a difficult task and has been the basis of study for a number of researchers.

Some of the difficulty that exists with composite components in fatigue service is the lack of a large fatigue life data and lack of compliant analytical tools for use in composite fatigue design. The "work around" is to conduct extensive tests and studies for the particular design that is being evaluated rather than being able to iterate that design at the drawing board stage. This results in added cost and time and hinders the ability to harness the potential of composites.

There has been extensive research on composite components subjected to repeated loading in one direction, or uniaxial loading. The analysis of composites subjected to multiaxial loading, one or more directions, remains a largely open field. This is critically important for composites in the aerospace industry as composites are being used more in the primary structure where the multiaxial load cycles are observed. As an example, the Airbus A380 structure is made of 20–30% composite materials by weight and was the first commercial aircraft to use a carbon fiber reinforced composite as the material for the aircraft wing box. The wing box is the primary structure that connects the aircraft's wings to the fuselage. While the aircraft is in flight, it is capable of six degrees of freedom and exerts a multiaxial state of stress on the wing box, and the ground-air-ground cycle that the aircraft goes through results in multiple components that are under fatigue loading. The various loads can be acting in-phase or out-of-phase.

There is still extensive research being conducted on the behavior of homogeneous components such as metals that are subjected to multiaxial cyclic loads. One of the complexities of performing fatigue analysis of metallic components in the low cycle fatigue regime is that they are load path dependent at high loads. A material is load path dependent when the final stress state at a point is dependent on the magnitude and sequence of load application. In calculating the fatigue life, it is necessary to account for such factors as whether the loading components are applied proportionally or non-proportionally and / or whether or not they are applied at the same time.

Studies on the effect of load path on the fatigue behavior of composites are still evolving. Wafa[4] and Inoue[5], for example, have reported conflicting results for the fatigue life of a glass fibre composite under out-of-phase loadings. Quaresimin et al.[8] in his review paper cites a lack of papers able to draw conclusive statements regarding the effect of load path on biaxial fatigue.

This thesis will explore the role of load path on the fatigue behavior of carbon fiber reinforced epoxy composites subjected to biaxial cyclic loading. The investigation will be aimed at discovering what effects load path has on the damage accumulation, cyclic properties, and fatigue life of the composite.

For this purpose, an 8 ply $[\pm 45]_{2S}$ layup of carbon fiber epoxy was selected since this material is commonly used in aerospace structures. The sample geometry was chosen to be a thin walled tube, as this allows for comparisons to existing literature.

Static tests to failure and uniaxial fatigue tests to failure will be used to generate the baseline data in fatigue and failure modes in both tension and torsion.

Biaxial fatigue tests will be conducted using three load paths: tension-torsion applied proportionally, tension first then torsion, and torsion first then tension. These loadings are similar to that used by Inoue[5]. However, loading levels over a larger range will be used to evaluate damage progression in both low and high cycle fatigue.

In Chapter 2, a literature review will be outlined. In Chapter 3, the experimental procedures will be covered including sample definition, test equipment used, quasi-static testing procedure, and fatigue test procedure. In Chapter 4, the results of the testing will be documented and discussed. Finally, in Chapter 5, conclusions based on the reasons presented in Chapter 6 will be presented.

Chapter 2

Literature Review

In this chapter a review of available literature on the subject of biaxial composite fatigue is presented. This will serve to identify knowledge gaps that exist in the area of biaxial fatigue that would serve as the basis for the objectives of this thesis study.

First, two review papers on composite biaxial fatigue research are summarized. Next, biaxial testing with superimposed loads and out-of-phase loads are reviewed. Then the prospect of a single theory on fatigue life prediction is discussed. Finally, this body of knowledge is shown benefit from more research in the area of load path testing of carbon fiber composites.

There has been a significant amount of research conducted in the area of multiaxial fatigue of composites and Talreja[1] and Quaresimin et al.[8] provide a good summary of the current state of research.

Talreja[1] offers a review of his work and involvement in composite fatigue research spanning the 80s, 90s, and post 2001. The paper is focused on unidirectional external reversed loads and its effects on the fatigue of composites. It serves well to highlight the differences in composites fatigue to metal fatigue. The review is biased to the authors' work and quotes independent research that supports claims made.

Talreja[1] describes the early years of research in the 80s as misguided by the rules of metals. He believed that:

> . . . the absence in polymer matrix composites of crystalline structure and plasticity should have directed fatigue studies in other directions, such as focusing on the role of fiber and interface failure.

Talreja[1] quotes Dharan's[9] 1975 work as influential in progressing the area of research of fatigue in composites. Dharan's[9] 1975 work clarified the roles of fibers and matrix, and their interface, in causing composite fatigue.

Attempting to shift studies way from Wöhler (S-N) curves and use Dharan's[9] work, Talreja[10] introduces the fatigue life diagram, as shown in Figure 2.1

Figure 2.1: Fatigue life diagram for unidirectional composites for axial tension-tension loading (Figure 1 from Ref. [1]) — Image removed due to copyright

The life diagrams were intended to be used as a design tool to replace the Wöhler curves. Their usefulness can be seen in understanding the properties of a carbon composite vs. high modulus carbon composite. Figure 2.2 shows that for a high-modulus carbon-epoxy, Region II, the progressive region of fiber bridging and debonding, is squeezed out by fibre breakage.

Figure 2.2: Fatigue life diagram for unidirectional carbon-epoxy (a) and high-modulus carbon-epoxy (b) loaded in cyclic tension along fibers (Figure 2–3 from Ref. [1]) — Image removed due to copyright

Damage in composites following the fracture mechanics based Paris law approach (developed for metals) was the second area into which Talreja[1] provides insight. With composites, there generally is not a single crack that causes failure as in metals, which discredits the Paris law approach. Talreja[11] in 1985 combined two research areas to form the basis for the field of continuum damage mechanics(CDM) in composites. Specifically, he used both Aveston et. al's[12] paper that reviewed why a single crack could form vs. multiple cracks normal to the fibre; and Krajcinovic's[13] work that defined continuum damage mechanics (CDM) for solids, to define CDM for composites.

Talreja[1] continues to describe advances made in CDM in the 90s and a new field synergistic damage mechanics (SDM). SDM is CDM using micromechanics to examine the microstructural damage. It has been noted, however, that solving all problems of damage with micromechanics is not a realistic proposition[1].

Talreja[1] briefly discusses SDM's extension into linear and nonlinear viscoelastic cross ply laminates. He mainly discusses what he envisions for future research in sustainable development of composites; and that is is for designers and engineers to take a step back and incorporate environmentally sound practices in their efforts. He ends the review encouraging environmental responsibility. In short, the central theme in the paper is the misguided efforts of researchers to treat composite fatigue as they previously treated metal fatigue.

Quaresimin et al.[8] highlighted the research associated with the type of multiaxiality, sample design parameters, and notches.

Quaresimin et al.[8] suggests that two different multiaxial states can be identified: the local (inherent) multiaxial stress state and the global (external) multiaxiality meaning the loads are applied in more than one direction. An external loading system will only yield geometrically identical internal stress state if the two components being used have the same material and layup. Inherent multiaxial stress state can induced by a single external load.

Quaresimin et al.[8] defines two multiaxial factors for use in the local multiaxial stress state. These factors are given as:

$$\lambda_1 = \frac{\sigma_{2,a}}{\sigma_{1,a}} \tag{2.1}$$

$$\lambda_2 = \frac{\sigma_{6,a}}{\sigma_{1,a}} \tag{2.2}$$

Where the terms $\sigma_{1,a}$ and $\sigma_{2,a}$ are the amplitudes of normal stress in the material 1 and 2 direction. The term $\sigma_{6,a}$ is the amplitude of shear stress in the material 6 direction (the plane of material 1 and 2 direction).

Quaresimin et al.[8] then states that for any two loading cases where λ_1 and λ_2 are equal then the fatigue results may be considered identical. This statement is to say that results are independent of the method of loading and depend only on the local state of stress multiaxiality.

In Quaresimin et al.[8], a phase shift is said to occur if two different systems are applied to a component that do not share the same starting or ending points in time. The phase shift is the difference between these two starting, or ending, points.

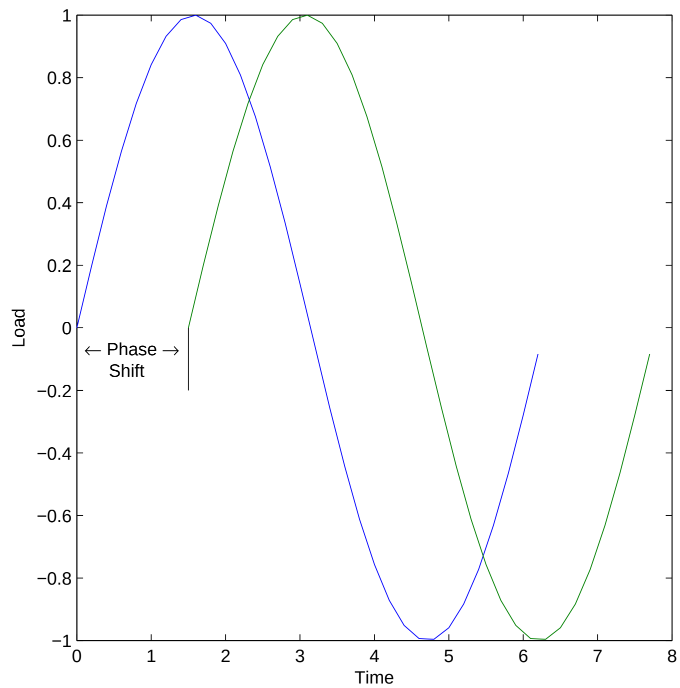

Figure 2.3: Phase shift example

A visual of this is shown in Figure 2.3. It is well known that when homogeneous materials such as metals undergo reversed plastic deformation, their fatigue life is highly dependent on loading path and therefore phase shift.

Quaresimin et al.[8] cites that there is a lack of experimental results in the literature to allow for any conclusive statements to be made in regards to the effects of a phase shift in external loads on the fatigue life of composite materials. Of the papers available, they show that different materials react differently to a phase shift. Thus, phase shifting becomes similar to a change in material and layup, and fundamentally changes the fatigue behavior. This is an area worth further investigation.

Quaresimin et al.[8] takes a large body of testing history, and using the multitude of applicable failure theories developed, shows that while some provide fair accuracy there are a number that are unsafe. They state that:

> ...this put[s] under question the general validity of the models investi-

gated, highlighting the need of a deeper understanding of damage mechanics.

Both of the review papers delve in the history of composite fatigue and conclude that no one method or model is currently available to describe composite fatigue. There is a lot of impressive ground work that has been laid out but many areas are open for exploration. Quaresimin et al.[8] leaves the avenue of load path quite open in stating that the load path research to date is full of conflicting results and the studies are not sufficiently broad in their scope.

Operating loads for a flexbeam in a helicopter rotor system requires a member to act in torsion while under a constant tension load. This loading condition has been studied by Sen[2] under quasi-static conditions and by Ogasawara[14, 15, 3] under cyclic fatigue.

Sen[2] found that the presence of a tensile load (21–24%UTS) increased the torsional rigidity of the system, and the allowable torque to failure of the system for all laminate configurations examined. The increased rigidity and allowable torque to failure of the system can be seen in Figure 2.4 and 2.5

Ogasawara[3] also found that the presence of a tensile load increased the torsional rigidity of the system as shown in Figure 2.6. Under a fatigue load, the CFRP and GFRP both show a degradation of the torsional rigidity as the number of cycles increases as shown in Figure 2.7.

In torsional fatigue testing, Ogasawara[3] showed that the addition of a constant tensile load has a positive benefit to the fatigue lives for the CFRP and GFRP materials. The CFRP showed a stronger positive reaction to the load as evidenced in Figure 2.8. It is noted that both the glass and carbon fiber composites used the same resin system with the carbon fibre composite outperforming the glass fibre composite. This leads to the conclusion that the carbon fibers in the composite are able to take more of a load and thus more of the damage of the load during the test. It is this

Figure 2.4: Comparison of failure torques under torsion and tension-torsion (Figure 6 from Ref. [2]) — Image removed due to copyright

Figure 2.5: Comparison of failure twist angles under torsion and tension-torsion (Figure 7 from Ref. [2]) — Image removed due to copyright

Figure 2.6: Torque versus twist angle curves of CFRP and GFRP under a constant tensile axial load (0, 20 kN) (Figure 3 from Ref. [3]) — Image removed due to copyright

Figure 2.7: Torque versus twist angle under cyclic torsion fatigue tests (Figure 5 from Ref. [3]) — Image removed due to copyright

load shed from the matrix that increases the performance of the composite.

Figure 2.8: Torsional fatigue life of unidirectional CFRP and GFRP under a constant axial tensile load. Fatigue life is defined as 10% or 20% reduction of torsional rigidity (Figure 8 from Ref. [3]) — Image removed due to copyright

Out-of-phase loading has been analyzed by Wafa[4] for glass fiber composites in bending/torsion and shown in Figure 2.9. He found that for high stress levels—thus low cycle fatigue—out-of-phase loading of glass fibers greatly reduces fatigue life. This agrees with analysis of metals by Ellyin[16]. Ellyin found that out-of-phase loading increased damage and reduced fatigue life. Ellyin[16] stated:

> This can be attributed to the circular stain path which attempts to force dislocation movements along all possible crystal slip planes.

Wafa also found that for fatigue life beyond 20,000 cycles, the out-of-phase loading provided an increased life. Wafa commented that this increased life could then be ignored as it would be conservative to assume in-phase loading. This condition should be studied in greater detail to remove that conservatism and provide better life estimates for materials.

Figure 2.9: Fatigue life curves for glass fiber in bending/torsion (Figure 11 from Ref. [4]) — Image removed due to copyright

Inoue[5] studied the load path response of glass fiber/vinyl ester resin composite in low cycle fatigue. Inoue[5] used three different load paths as detailed in Figure 2.10

Inoue[5] stated that:

- No significant effect of loading path on the fatigue life exists.
- The modulus decay in shear with respect to the number of loading cycles is affected by the loading path while the modulus decay in tension was not significantly affected
- The models created predicted that as the damage progressed that strains in unloaded directions would appear. These strains were attributed to matrix cracking damage.

This result differs greatly from the research of Wafa[4] in 1997 where it was found that out-of-phase loading greatly reduced the fatigue life. It is noted that the matrix

Figure 2.10: Three types of cyclic load path (Figure 2 from Ref. [5]) — Image removed due to copyright

material used by Wafa[4] was polyester and Inoue[5] used vinyl ester. While Inoue[5] found that the fatigue life was not affected by load path in low cycle fatigue, the extension of this conclusion to high cycle fatigue remains unanswered.

Inoue[5] refers to peculiarities observed in the tensile or shear strain as the one load is applied or removed. This multiaxial stress state is expected in a non-isotropic material that is under a load; however, the variations in this behavior led Inoue to conclude that structural inhomogeneity and internal damage of the material might have caused these phenomena.

This is in agreement with the comments later made by Quaresimin et al.[8] and Talreja[1] that inconclusive results were obtained when conducting research in this area.

The prediction of cycles to failure of the composite laminate through the understanding of the effects of the load history on the material properties or damage is the ultimate goal of biaxial fatigue research. The prediction of failure has been based on multiple methods including: extending polynomial failure theories for static failure to fatigue[17, 4, 18], strain energy[19, 20], and damage mechanics[21, 22, 23], to name a few. Yet Amijima et al.[24] reported that:

> ...in certain conditions, the failure surface in the multiaxial stress state at a given cycle is not proportional to the static one...

This observation demands that to be able to reliably predict failure, one must understand the mechanisms of failure occurring to validate that assumptions used in the failure theory would adequately extend to many different cases. This statement has been made by Talraja[1] in 2000:

> The only rational way forward for developing predictive criteria of general validity is to base these on systematic studies of damage mechanisms

2.1 Summary of Literature Review and Thesis Objectives

The review presented above suggests that the past work on multiaxial fatigue is limited. Within this body of published literature, studies on the effect of load path are limited further. These few studies present conflicting conclusions on the effect of load path on fatigue life of structural composites. Further investigation is required to delineate the effect of load path on fatigue behavior in both low cycle fatigue (high stress amplitude) as well as high cycle fatigue (low stress amplitude) regions. Further, insight into damage development during multiaxial fatigue and mechanisms that result in these damages is required in order to reliably develop models to predict fatigue stress or life of structural composites under multi-axial loading conditions encountered during service. Hence, the objectives of this thesis are:

(a) To experimentally study the effect of load path on biaxial fatigue behavior of a graphite fiber reinforced epoxy composite

(b) Experimentally study the uniaxial fatigue of this composite to generate baseline data to evaluate the biaxial data

(c) To experimentally study the various damage modes that develop during fatigue and its effect of material properties

(d) Use (b) and (c) along with (a) to evaluate the effect of load path on biaxial fatigue.

Chapter 3

Experimental Details

The experiments performed to meet the objectives of this work are described in this chapter. The samples that were manufactured for the experiments are described in Section 3.1. A list and description of the equipment used are detailed in Section 3.2. Finally, Section 3.3 describes the tests that were performed.

3.1 Samples

This section describes the samples used for the fatigue tests discussed in Section 3.3. The choice of layup is described in Section 3.1.1, followed by the sample geometry in Section 3.1.3. The material and manufacturing method is described in Sections 3.1.2 and 3.1.4 respectively.

3.1.1 Laminate Layup

The layup choice for a composite heavily influences its properties. One of the main attractions of a composite is the ability to tailor the properties to meet the design requirements. For example, running the fibers in the direction of the maximum load will allow the designer to maximize the strength in that direction. A layup sequence of

$[0\backslash 90]_s$, known as a cross-ply layup, is useful for loadings that are longitudinally and transversely dominated. A layup sequence of $[\pm 45]_s$, known as an angle-ply layup, is useful for loadings that are shear dominated.

A majority of previous multiaxial fatigue studies have focused on$[0\backslash 90]_s$ [24, 25, 7, 17, 23, 21, 4]. The $[\pm 45]_s$ laminate use is limited [26, 27, 28, 21, 4]. However, $[\pm 45]_s$ plies are part of quasi-isotropic laminates widely used in aerospace application. Hence, $[\pm 45]_{4s}$ laminate was chosen for the experimental samples.

3.1.2 Material

Prepregs made up of high modulus carbon fibers and Newport 301 resin were used to manufacture the $[0]_8$, $[90]_{16}$, and $[0\backslash 90]_{6s}$ plates, as well as the $[\pm 45]_{4s}$ tubes. The properties of the lamina were provided by the material supplier and are tabulated in Table 3.1.

S_1^+	2920.	MPa
S_1^-	-1340.	MPa
S_2^+	60.	MPa
S_2^-	-169.	MPa
S_{12}^+	70.1	MPa
S_{12}^-	-70.1	MPa
E_1	228.	GPa
E_2	7.2	GPa
G_{12}	3.52	GPa
ν_{12}	.3	

Table 3.1: Properties of lamina made up of Grafil Inc. Pyrofil^{TM} HR40 12K carbon fibers and Newport 301 resin

3.1.3 Geometry

One common geometry used in multiaxial fatigue is tubular geometry. Some selected geometries that have been used in previous studies on biaxial fatigue are shown in Table 3.2. Based on these studies, the dimensions of the tubes used in this work are

Author	Sample
Wafa[4]	
Fujii[5]	
Fujii[7]	

Table 3.2: Sample geometries used in previous studies (Figure 2 of Ref. [4], Figure 1 of Ref. [5], and Figure 1 of Ref. [7]) — Images removed due to copyright

shown in Figure 3.1.

The sizing of the tube was based on previous studies and the assumptions used in those designs were quoted as being based on Vicario et al.[29]. Vicario et al.[29] stated that tube designs for testing should maintain $l/D > 3$ and $t/D \leqslant 0.05$. This thesis exceeds those guidelines and maintains $l/D = 4.9 > 3$ and $t/D = .024 \leqslant 0.05$.

Pagano[30] states in his paper that “One cannot define an acceptable or standard value of $\frac{R}{h}$ which is sufficiently general to encompass all anisotropic materials and orientations without stipulating the desired degree of precision. However…it appears

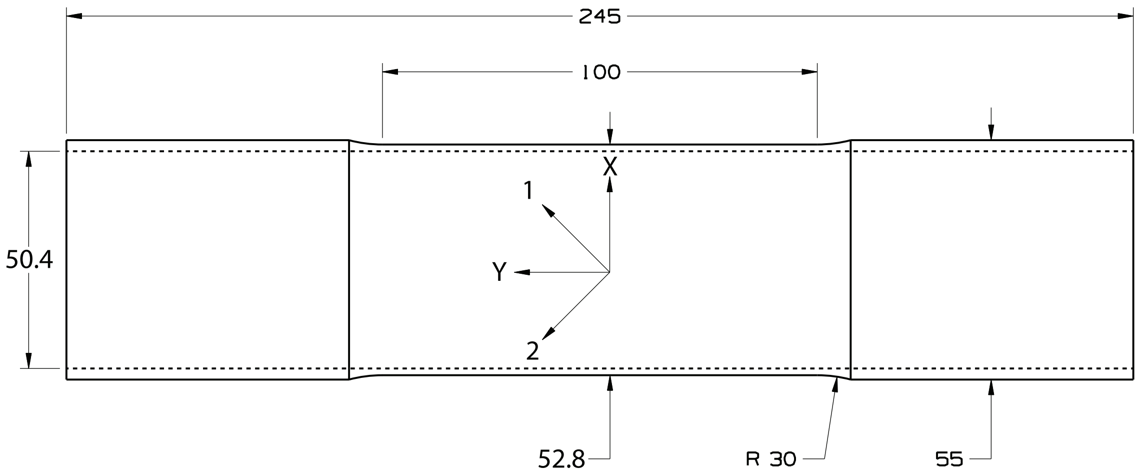

Figure 3.1: Biaxial fatigue test sample (dimensions shown in millimeters)

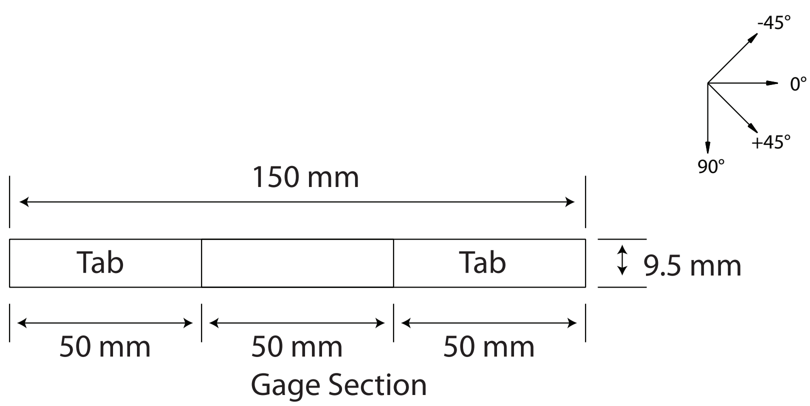

Figure 3.2: $[0]_8$ samples used in tension testing to measure longitudinal properties

that a conservative estimate of specimen length L is given by $L = 4R + l$ where l is the desired gage length."

This thesis exceeds that guideline and maintains a specimen length of $L = 5.8R+l$. These relations for length were experimentally derived to ensure that end effects are eliminated in the gage section. This will be discussed in Chapter 4.

Lamina properties were measured in accordance with the American Society of Testing and Materials (ASTM) specifications for tension, ASTM D3039[31], and shear, ASTM D7078[6]. The dimensions of the samples used in measuring lamina properties testing are given in Figures 3.2-3.4.

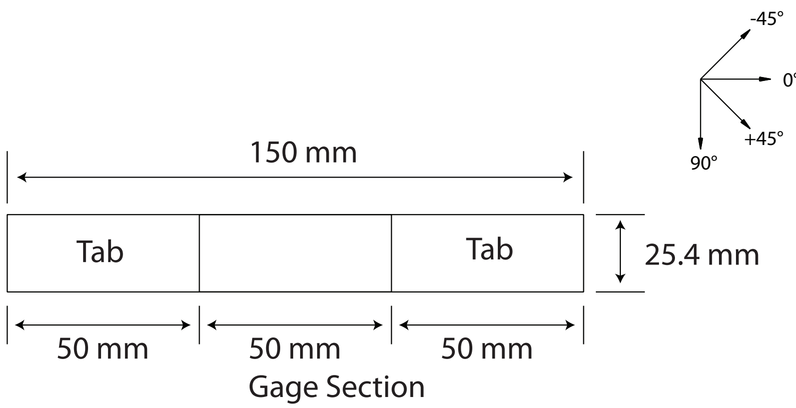

Figure 3.3: $[90]_{16}$ samples used in tension testing to measure transverse properties

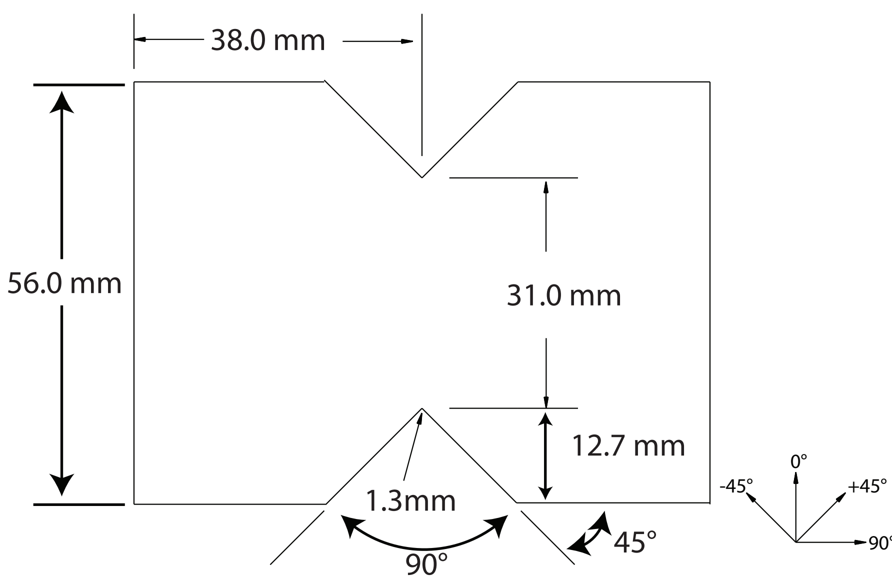

Figure 3.4: $[0\backslash 90]_{6s}$ sample used in shear testing to measure the in-plane shear properties

3.1.4 Manufacture

Innovative Composites Engineering (ICE) was selected to manufacture the samples following a competitive solicitation for bids. ICE is an ISO9001 certified company based in White Salmon, Washington that was founded in 1989 and manufactures composite tubes and shapes for the aerospace, industrial, automotive, recreational, defense and oil & gas industries[32].

The composite samples were manufactured by roll wrapping. Roll wrapping the $[\pm 45]_{2s}$ composite tube was achieved by wrapping the Grafil unidirectional fibers at a ± 45 degree angle around a slightly tapered mandrel. At specific intervals along the length of the mandrel a carbon fibre weave was rolled on to serve as filler for the grip section. This layup was then covered with a breather cloth, vacuum bagged and placed in an autoclave. The cure cycle used was 345 kPa pressure at $135°C$ for 60 minutes. Once cured, the mandrel was removed, the resulting tube ends squared off, and the tube was sectioned into individual samples.

The original process for this called for grinding the samples to achieve the proper dimensions and ply count needed. Following a miscalculation of the ply count in the layup, the samples were further machined at the University of Manitoba machine shop by lathe, machining the inside and outside diameter to achieve the dimensions shown in Figure 3.1 and a ply count of 8.

Hand laid panels of unidirectional lamina $[0]_8$ and $[90]_{16}$ were cured in a platen press and supplied by ICE. Sample ends were bonded with tabs made of a woven carbon fibre composite using 3m Scotch-Weld structural adhesive film AF-31 (10 mil thick) and cured in a platen press. The Wabash model number 350-H24-CLX platen press at the University of Manitoba was used. Tensile test samples, shown in Figures 3.2 and 3.2, were cut using a Micro-Matic precision wafering machine at the University of Manitoba.

A hand laid panel of unidirectional lamina $[\pm 45]_{6S}$ was cured in a platen press supplied by ICE. Shear test samples, shown in Figure 3.4, were cut by the Composite Innovation Centre at a 45 degree angle from the sheet to get $[0\backslash 90]_{6S}$ laminates. The samples were cut using diamond edge tooling in a computer numeric controlled 3-axis milling machine.

All of the test specimens that were used are documented in Table 3.3.

Quasi-static Tests				
Load Type	Specimen Type	Specimen Details	Number of Specimens	Properties Measured
Uniaxial	Lamina	$[0]_8$	5	σ_1^{max}, E_1, ν_{12}
Uniaxial	Lamina	$[90]_{16}$	5	σ_2^{max}, E_2, ν_{21}
Uniaxial	Lamina	$[0/90]_{6s}$	5	τ_{12}^{max}, G_2
Uniaxial	Laminate tube	$[\pm 45]_{2s}$	1	σ_{yy}^{max}, E_{yy}, ν_{xy}
Uniaxial	Laminate tube	$[\pm 45]_{2s}$	1	τ_{xy}^{max}, G_{xy}
Biaxial	Laminate tube	$[\pm 45]_{2s}$	2	σ_{yy}^{max}, τ_{xy}^{max}
Fatigue Tests				
Load Type	Specimen Type	Specimen Details	Number of Specimens	Properties Measured
Type IV (uniaxial)	Laminate tube	$[\pm 45]_{2s}$	3	N
Type V (uniaxial)	Laminate tube	$[\pm 45]_{2s}$	3	N
Type I (biaxial)	Laminate tube	$[\pm 45]_{2s}$	4	N
Type II (biaxial)	Laminate tube	$[\pm 45]_{2s}$	4	N
Type III (biaxial)	Laminate tube	$[\pm 45]_{2s}$	5	N

Table 3.3: List of all samples used

3.2 Test Equipment

The various pieces of equipment used during the static and fatigue testing included an Instron 8822 biaxial load frame, Instron Fast Track 8800 materials test control system, Vishay S7000 data acquisition system (DAQ), and GOM Aramis digital image correlation system. The tests were conducted at the University of Manitoba. Details of each piece of equipment are given in the following sub-sections.

3.2.1 Load Frames

Three different load frames were used in this investigation. These included the Instron 5500R, Instron 8562, and Instron 8822, each as described below:

Instron 5500R Load Frame

Static tests, to determine lamina properties, were carried out on an Instron 5550R screw driven load frame. The Instron 5500R was interfaced with a personal computer running Instron's Bluehill software version 2.5 software. The Instron 5500R was equipped with a ± 25 kN load cell. The Instron 5500R was equipped with mechanical wedge grips for clamping flat specimens.

The Bluehill software is capable of data collection and can store positional and load data of the cross-head.

Instron 8562 Load Frame

Static tests to determine lamina properties were carried out on a Instron 8562 servo-electric load frame, shown in Figure 3.5. The Instron 8562 was interfaced only by a man-machine interface (MMI) panel. The Instron 8562 was equipped with a ± 25 kN load cell, and with mechanical wedge grips for clamping flat specimens.

The Vishay S7000 DAQ, discussed in Section 3.2.2, was used in conjunction with this load frame during testing for data acquisition.

Instron 8822 Load Frame and Test Fixture

The fatigue tests were performed using an Instron 8822 servo hydraulic load frame controlled by an 8800 materials test system controller[33]. The Instron 8822 load frame had collet style grips that accepted a 1 inch diameter post and clamped using hydraulic grips. The system was capable of ± 250 kN axial force and ± 2.5 $kN \cdot m$

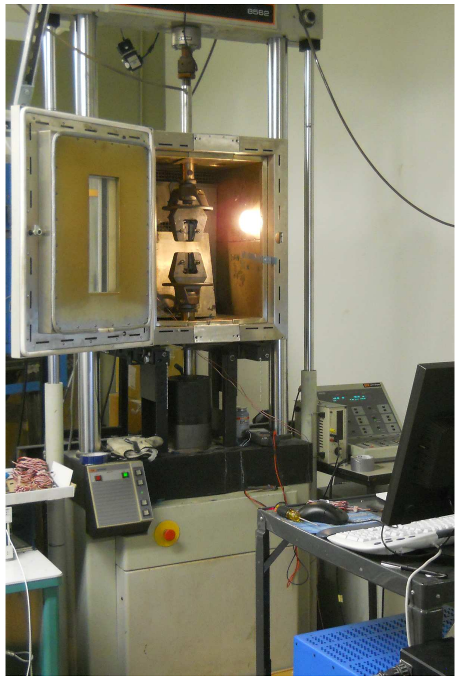

Figure 3.5: Instron 8562 servo-electric load frame

rotational force. While the collet grips could be used over the full range of the axial force, they were rated for $\pm 2\ kN \cdot m$ rotational force.

The 8800 material test system could be interfaced using either man-machine interface (MMI) panels or an attached personal computer running the Fast Track 2 materials test software[34]. The MMI panels were used for shear testing lamina properties, and static testing the laminate properties. The Fast Track 2 software module 'simple fatigue - MAX' was used for the fatigue testing as specific wave form generation was required, and data collection could be completed by the software. Also, the Fast Track 2 software system greatly automated the loop tuning process for determining the required proportional, derivative, integral gain, and lag required by the controller.

A custom fixture, shown in Figure 3.6, was used for shear testing. The fixture was equipped with an Instron D style connector that required the use of an adapter to switch from the Instron D connector to a 1 inch post to enable clamping by the Instron 8822 load frame.

Figure 3.6: ASTM-D-7078 shear test fixture

As described in Section 3.1.3, the fatigue sample had an outside diameter of 53 *mm*, whereas the collet grips of the Instron could accommodate a maximum 25.4 *mm* (1 *inch*) cylinder. This necessitated the design of holding fixture to clamp the sample and mate with the load frame.

The first design iteration of the specimen holding fixture was as shown in Figure 3.7. This fixture was machined out of solid stainless steel (17-7 PH condition H1150). The stainless steel was selected as it is a high strength metal with excellent fatigue resistance. The fixture was designed to hold the specimen with side pressure to keep the clamps out of the loading path to guard against loss of clamping fatigue cycles. The center plug was aligned via a pin in the base to keep the sample axially aligned with the Instron.

After a few tests on samples (not included in this thesis) the fixture was slightly redesigned with reinforcing side walls, shown in Figure 3.8. These walls still allowed for specimen loading and unloading and reduced fixture movement that was occurring

Notes:

1. Item 3 to be press fit into item 1.
2. (△2) Carbon fiber sample is shown in assembly for reference only

Parts List

Item	Description	Quantity
1	Clamp Base	2
2	Clamp	4
3	Post	2

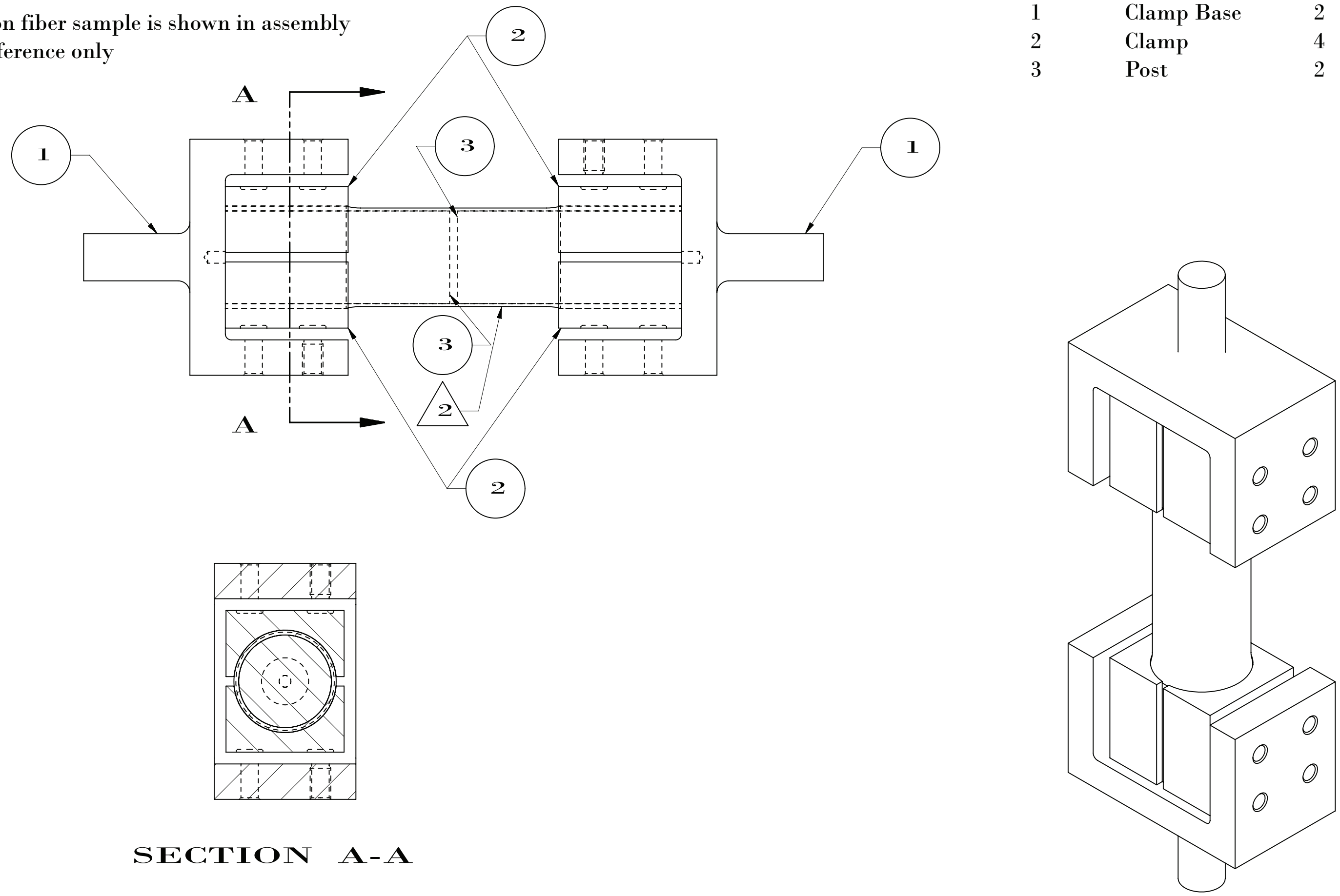

Figure 3.7: As designed test fixture

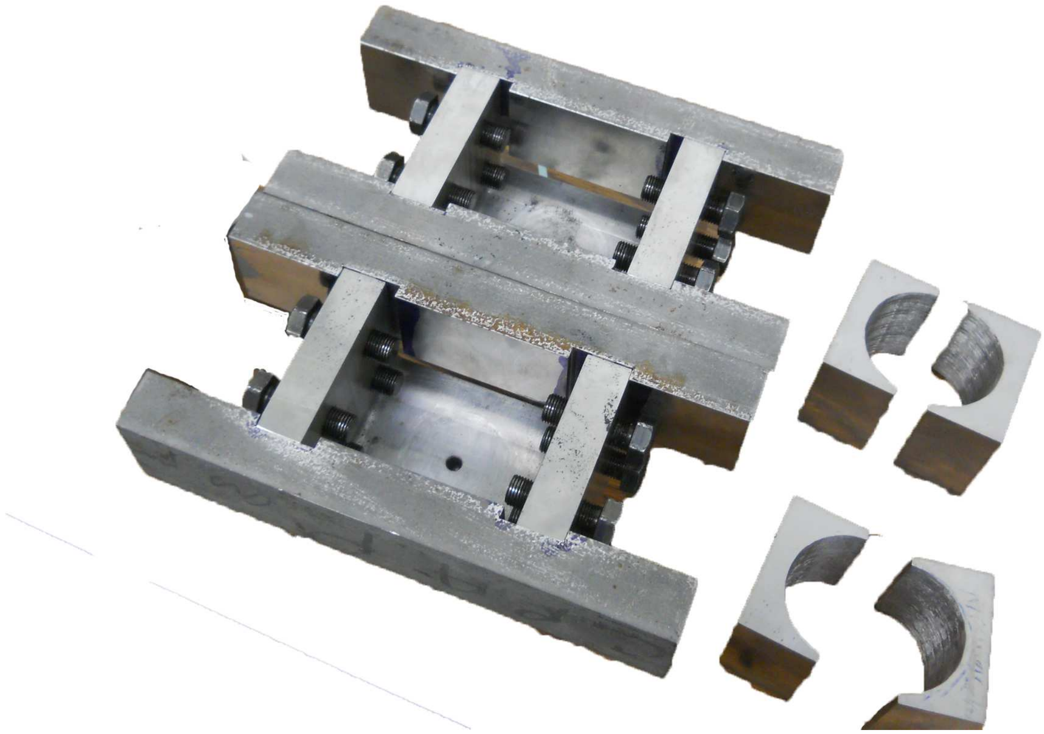

Figure 3.8: As built specimen holding fixture

at the top of the fixture, resulting in uneven clamping pressure and sample movement. The side walls also allowed for easier shimming during sample loading to keep the specimen properly aligned in the Instron.

3.2.2 Strain Measurement

ARAMIS System

The ARAMIS system is produced and maintained by Gesellschaft für Optische Messtechnik mit beschränkter Haftung (GOM mbH). The GOM mbH web-site[35] describes the ARAMIS system as:

> ARAMIS is a non-contact and material independent measuring system providing, for static or dynamically loaded test objects, accurate:
>
> - 3D surface coordinates
> - 3D displacements and velocities

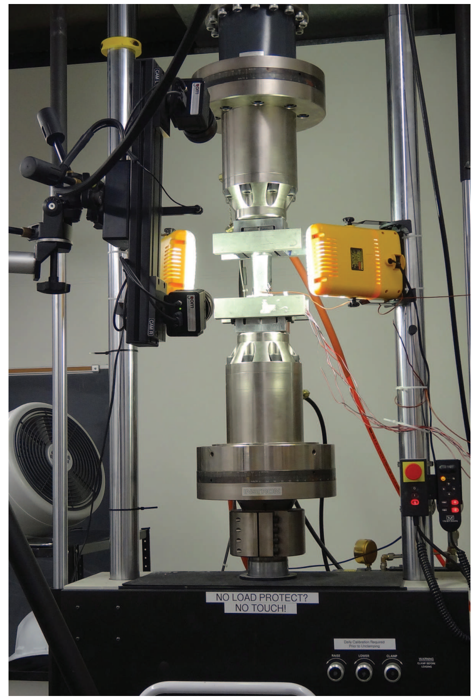

Figure 3.9: ARAMIS Camera Set-up (showing supplemental lights required with sample loaded in Instron 8822 load frame)

- Surface strain field values
- Strain rates

The ARAMIS cameras are shown in Figure 3.9. The system works by taking a pair of stereo images of the target object after the object has been painted white and sprayed with a black stochastic dot pattern. The system is then able to map the dot pattern and track the relative movements of the dots and thus map a strain field on the object without having to contact the surface.

Vishay S7000 DAQ

The Vishay S7000 DAQ, shown in Figure 3.10, is capable of logging: high level inputs, ±10 Volts; strain gages, with automatic bridge completion of quarter, half, and full bridges for 120, 350, and 1000Ω strain gages; and thermocouple inputs. Each input type is capable of measuring eight (8) inputs, each at a rate of 10–2048 Hz.

The high level input card was used to measure the output of linear and rotary position, and linear and rotary force from the Instron 8800 controller. The Instron

Figure 3.10: Vishay S7000 DAQ

8800 controller was set to track those values and output a ±10 Volt signal to the Vishay S7000.

The strain gage card was used to measure the values of strain on the samples using a strain gage rosette. A Vishay Micro-Measurements C2A-06-125LR-350 3 element strain gage rosette was used. This strain gage is a 350Ω resistance gage with an active length of $^1/_8$ inch. Samples were monitored using a bridge excitation of 1 Volt. Previous experimentation with this material and strain gage have demonstrated stable measurements with 1 Volt after 1 hour of sampling to allow for strain gage heating effects. A bridge excitation of 2 Volts, the next selectable step, displayed a steady strain increase of 11 microstrain/hour over an 8 hour period with the strain still increasing after sampling for 19 hours.

The thermocouple card was used to measure the values of temperature of the lab and sample using a J type thermocouple. The temperature of both the lab and sample were measured to ensure that the sample temperature did not rise significantly above the lab temperature.

3.3 Test Procedure

The procedures followed for performing testing are documented below. The quasi-static testing performed to determine the lamina properties is described in Section 3.3.1. These properties include ultimate strength and modulus in the longitudinal, transverse, and shear directions. Then, the quasi-static testing, to determine properties of the laminate, are described in Section 3.3.2. Finally, the uniaxial and biaxial fatigue tests conducted to meet the objectives of this work are described in Section 3.3.3.

3.3.1 Quasi-Static Testing

The mechanical properties of the lamina provided by the material supplier are tabulated in Table 3.1. Testing to confirm these properties were conducted. The longitudinal, transverse, and shear properties are documented in the following sub-sections. The longitudinal properties were measured in a direction parallel to the fiber axis (1-direction in Figure 3.11). The transverse properties were measured perpendicular to the fiber axis (2-direction in Figure 3.11). Shear properties were measured in response to the shear forces applied in the 1-2 plane.

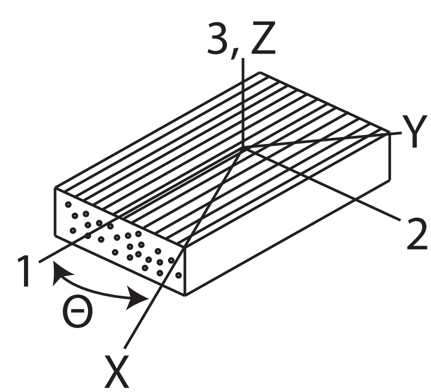

Figure 3.11: Lamina coordinate system

Longitudinal Lamina Properties

The longitudinal properties of the lamina were obtained by testing five $[0]_8$ samples, shown in Figure 3.2, in accordance with American Society of Testing and Materials (ASTM) Standard ASTM-D-3039[31], Standard Test Method for Tensile Properties of Polymer Matrix Composite Materials, using the Instron 8562 load frame. Specimen testing was in accordance with ASTM-D-3039[31] procedures except that all specimens were unconditioned. It should be noted that the specimens were stored and tested at room temperature.

The samples were instrumented with C2A-06-125LR-350 strain gages to record the sample strains. The strains, load frame force, and load frame position were collected by the Vishay S7000 DAQ. All the specimens' dimensions of width, thickness, and length were recorded. Specimens were then loaded using wedge grips taking care to align the sample edge with the grips to ensure proper loading in the test direction. The loading was applied a rate of 1.5 $\frac{millimeters}{minute}$ to achieve sample failure within the recommended 1-10 minutes.

Transverse Lamina Properties

The transverse properties of the lamina were obtained by testing five $[90]_{16}$ samples, shown in Figure 3.3 in accordance with ASTM-D-3039[31] using the Instron 5500R load frame. Specimen testing was in accordance with ASTM-D-3039[31] procedures except that all specimens were unconditioned. Specimens were stored and tested at room temperature.

The samples were instrumented with C2A-06-125LR-350 strain gages to record the sample strains. The strains, load frame force, and load frame position were collected by the Vishay S7000 DAQ. All the specimens' dimensions of width, thickness, and length were recorded. Specimens were then loaded using wedge grips taking care to align the sample edge with the grips to ensure proper loading in the test direction.

The loading was applied a rate of 0.3 $\frac{millimeters}{minute}$ to achieve sample failure within the recommended 1-10 minutes.

Shear Lamina Properties

The shear properties of the lamina were obtained by testing five $[0\backslash 90]_{6s}$ samples, shown in Figure 3.4, in accordance with ASTM-D-7078[6], Standard Test Method for Shear Properties of Composite Materials by V-Notched Rail Shear Method, using the Instron 8822 load frame. Specimen testing was in accordance with ASTM-D-7078[6] procedures except that all specimens were unconditioned. Specimens were stored and tested at room temperature.

The samples were instrumented with C2A-06-125LR-350 strain gages to record the sample strains. The strains, load frame force, and load frame position were collected by the Vishay S7000 DAQ. All specimen dimensions required were recorded. Specimens were then loaded in the test fixture using the supplied spacers. The loading was applied a rate of 2.0 $\frac{millimeters}{minute}$ to achieve sample failure within the recommended 1-10 minutes.

The first tested sample instrumented with two strain gages to ensure sample bending was below the required 3.0%. This sample showed a bending value of 0.38%, hence, all remaining samples were tested with only one strain gage.

3.3.2 Laminate Properties

The Instron 8822 load frame, described in Section 3.2.1, was used for all quasi-static laminate testing. These tests were conducted at room temperature. Samples were bonded with a C2A-06-125LR-350 strain gage to record strains during testing and to aid in sample loading. Samples were also painted with spray paint to allow for ARAMIS system data capture.

Three tests were conducted to support the damage evaluation of selected fatigue samples. Specifically, a quasi-static tension test to failure, a quasi-static torsion test to failure, and a quasi-static combined tension-torsion test to failure. The combined tension-torsion test to failure was conducted at a stress ratio of $\alpha = \frac{3}{1}$ where α is defined as the ratio of global tensile stress to global shear stress, see Equation (3.1).

$$\alpha = \frac{\sigma_y}{\tau_{xy}} \tag{3.1}$$

3.3.3 Fatigue Testing

The Instron 8822 load frame and specimen holding fixture, discussed in Section 3.2.1, was used for all fatigue tests. These tests were conducted at room temperature. Type J thermocouples were attached to each sample and the load frame to measure sample temperature and ambient temperature. The thermocouple was attached to the sample using 3M brand PCT-2M mylar tape and plastic zip ties. Samples were equipped with C2A-06-125LR-350 strain gages to record strains during testing and to aid in sample loading. Samples were also painted with spray paint to allow for ARAMIS system data capture. Tests were conducted at number of different stress levels to obtain both low and high cycle fatigue data. All fatigue tests were conducted at a stress ratio, α, of $\alpha = \frac{3}{1}$ where α is defined as the ratio of tensile stress to shear stress. A test frequency of 3 Hz and a load ratio of $R = 0$ were used for all fatigue tests. Three different biaxial load paths, shown in Figure 3.12, were used to evaluate the effect that load path has on fatigue life.

Type I A biaxial load is proportionally applied to the specimen. Specifically, the tension and torsion loads are increased simultaneously while maintaining the stress ratio $\alpha = 3$.

Type II A tensile load is first applied and held, the matching torsion load for a stress ratio of $\alpha = 3$ is loaded and unloaded, and finally the tensile load is removed.

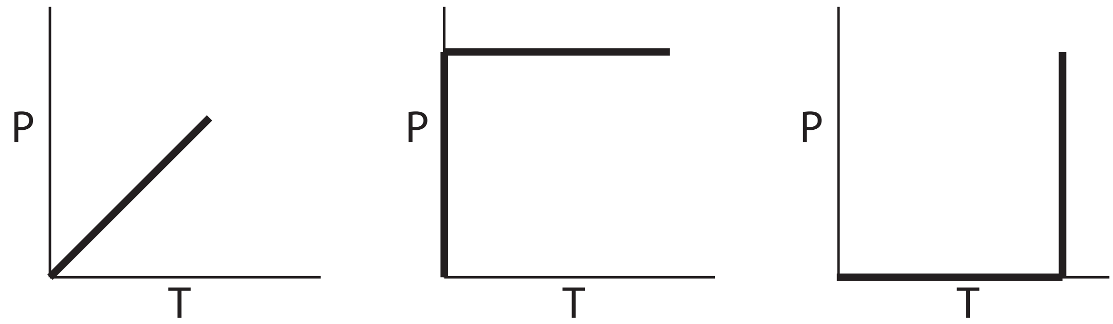

(a) Type I (b) Type II (c) Type III

Figure 3.12: Load Path Visualization for Type I-III

Biaxial Fatigue Tests			
$\sigma_{yy}^{applied}/\sigma_{yy}^{max} \times 100$	Type I	Type II	Type III
75%	Sample 12	Sample 21	Sample 23
60%	Sample 13	Sample 16	Sample 19
50%	Sample 14	Sample 17,25	Sample 18
40%			Sample 22,24
33%	Sample 1		

Table 3.4: Samples Used for Biaxial Fatigue Tests

Type III A torsional load is first applied and held, the matching tension load for a stress ratio of $\alpha = 3$ is loaded and unloaded, and finally the torsion load is removed.

The load paths are the same as those used by Inoue[5]. In addition, samples were also subjected to uniaxial fatigue to understand the damage progression during biaxial fatigue.

Type IV Tensile load only is loaded and unloaded.

Type V Torsion load only is loaded and unloaded.

Using the lamina properties given in Section 3.3.2, specimen geometry given in Section 3.1.3, lamination theory, and maximum stress criterion, loads required for various failure modes in [+45] and [−45] plies are derived in equations (A-62) - (A-72) in Appendix. These loads for each failure mode in [+45] and [−45] plies are

Uniaxial Fatigue Tests		
${}^{\sigma^{applied}}/_{\sigma^{max}} \times 100$	Type IV	Type V
90%		Sample 32
80%		Sample 31
75%	Sample 29	Sample 28
60%	Sample 30	
50%	Sample 27	

Table 3.5: Samples Used for Uniaxial Fatigue Tests

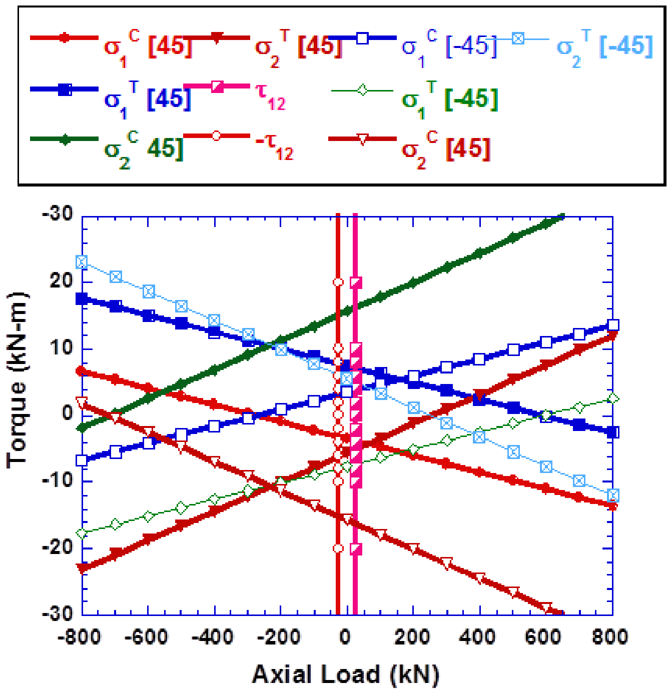

Figure 3.13: Failure envelope for first ply failure

represented by lines in Figure 3.13. The loads correspond to the values of global axial and torsional loads applied to the tube that would cause the stresses in the material coordinates to exceed the allowable and result in corresponding failure. The various failure modes are longitudinal compressive failure if σ_1^C is exceeded, longitudinal tensile failure if σ_1^T is exceeded, transverse compressive failure if σ_2^C is exceeded, transverse tensile failure if σ_2^T is exceeded, positive shear failure if τ_{12}^+ is exceeded, and negative shear failure if τ_{12}^- is exceeded.

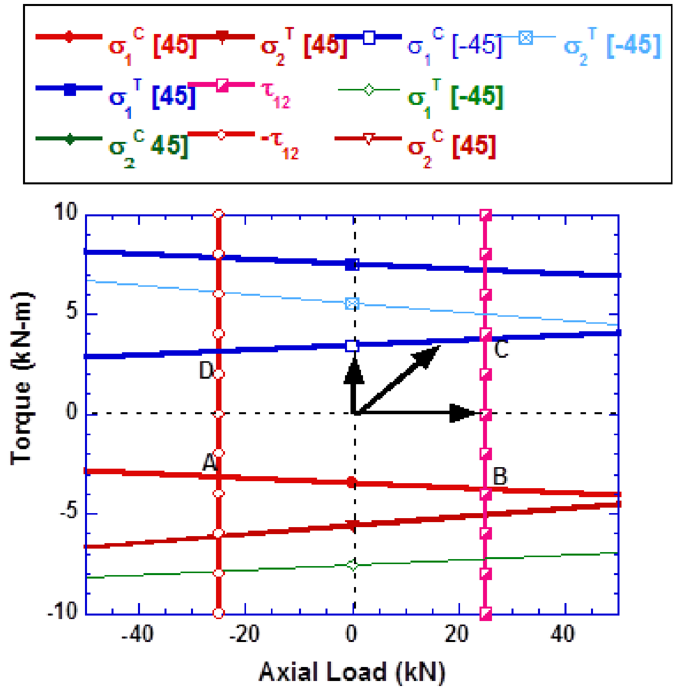

Figure 3.14: Failure envelope for first ply failure denoted ABCD

Intersection of various lines define the failure envelope for first ply failure, ABCD, shown in Figure 3.14

It can be inferred that the first ply failure is predicted to be by in-plane shear during axial loading and longitudinal compressive failure during torsional loading. Both are possible under biaxial loading depending on the α defined previously. The failure envelope, ABCD, identifies the load space within which no failure will occur. Some fatigue tests were done at loads within this envelope. Other loads were chosen beyond this envelope; this means samples developed damage during the first fatigue cycle, which grew in size and number during the subsequent cycles leading to final failure.

The load levels used in biaxial and uniaxial fatigue testing are tabulated in Tables 3.4 and 3.5 respectively. All tests were done at an R ($\sigma_{min}/\sigma_{max}$) of 0. The load paths for uniaxial and biaxial testing are shown by arrows in Figure 3.14.

Chapter 4

Results and Discussion

In this chapter the results of testing described in Section 3.3 are presented and discussed. Initially, the static test results for lamina properties are presented and discussed in Section 4.1. Next, the effects of clamped end constraints and specimen geometry on the test results are presented in Section 4.2 to confirm the validity of test results obtained using the tube geometry. In Section 4.3, the results of the quasi-static test on the $[\pm 45]_{2s}$ laminate tubes are presented and discussed. An incremental analysis using lamination theory and the lamina properties, mentioned in Section 4.1, is presented to explain the non-linearity observed in the quasi-static test results. Subsequently, uniaxial fatigue data are presented and discussed. Finally, multiaxial fatigue data are presented and discussed to delineate the effect of load path on multiaxial fatigue of multidirectional laminates.

4.1 Lamina Properties

This section details the test results for lamina properties. These properties were used to determine the laminate modulus and stress-strain curves, which in turn were compared with experimental results to delineate (i) the effect of specimen geometry on measured laminate properties and (ii) the effect of damage evolution on the observed non-linearity in the stress-strain curves.

4.1.1 Longitudinal Lamina Properties

The longitudinal properties were determined by testing five (5) $[0]_8$ samples in accordance with ASTM-D-3039[31]. The results of these tests include the ultimate tensile strength in the fiber direction, σ_1^{max}, Young's Modulus in the fiber direction, E_1, and Poisson's Ratio in the 1-2 plane, ν_{12} which are tabulated in Table 4.1. The average value of Young's Modulus, denoted E^{mean}, was found to be 210 GPa with a standard deviation, S_{n-1} of 22 GPa for a coefficient of variation (CV) of 10%. This value is lower than the values provided by the manufacturer in Table 3.1 by 8%; however, it is within the standard deviation. The modulus varied by a large magnitude, from 177–233 GPa. Since the longitudinal modulus would decrease rapidly if the load axis is off-set with respect to fiber axis even by few degrees (instead of being zero), error in manufacturing [0] test specimens is believed to be the reason for the observed scatter. The increase in strength with increase in modulus, observed in Table 4.1, confirms this reasoning. The average strength value σ_1 of 2746 MPa is lower than the reported value by 6%. The average Poisson's ratio, ν_{12}, is 0.28.

Specimen	Longitudinal Strength σ_1^{max} (MPa)	Longitudinal Modulus E_1 (GPa)	Poisson's Ratio ν_{12}
S1	2235	177	.282
S2	2787	215	.246
S3	2992	225	.294
S4	2472	202	.280
S5	3245	233	.312
Mean	2764	210	.283
S_{n-1}	402	22	.024
CV	15%	10%	9%

Table 4.1: Lamina longitudinal properties

4.1.2 Transverse Lamina Properties

The transverse Young's modulus E_2 was determined by testing five (5) $[90]_{16}$ samples in accordance with ASTM-D-3039[31]. The results of these tests include the ultimate tensile strength perpendicular to the fiber direction, σ_2^{max}, the transverse Young's Modulus perpendicular to the fiber direction, E_2; and the Poisson's ratio in the 2-1 plane, ν_{21} which are tabulated in Table 4.2. The average value of the Young's Modulus, denoted E^{mean} is found to be 8.01 GPa with a standard deviation, S_{n-1} of 1.09 GPa for a coefficient of variation, CV, of 14%. This value is higher than that reported in Table 3.1 by 11% but is within the standard deviation. The scatter within reported values is attributed to the misalignment of fibers while cutting the samples, as mentioned in Section 4.1.1.

The average transverse tensile strength and Poisson's ratio, ν_{12}, are 43.5 MPa and .013 respectively. Specimen S5 yielded a strength that was much lower than the values obtained using other samples. Since transverse strength is affected significantly by any edge defects introduced during specimen preparation, the lower strength of S5 was believed to be due to manufacturing defects. Hence, the strength of S5 was not included in determining the average strength.

Specimen	Transverse Strength σ_2^{max} (MPa)	Transverse Modulus E_2 (GPa)	Poisson's Ratio ν_{21}
S1	51.2	7.46	.013
S2	45.9	7.40	.012
S3	36.9	6.98	.015
S4	39.9	8.54	.013
S5*	24.9	9.67	.005
Mean	43.5	8.01	.013
S_{n-1}	6.4	1.09	.001
CV	15%	14%	9%

*Not included in population statistics

Table 4.2: Lamina transverse properties

4.1.3 Lamina Shear Properties

The in-plane shear properties were determined by testing five (5) $[0/90]_{6S}$ samples per ASTM-D-7078M05 [6]. A representative shear stress-strain result in shown in Figure 4.1. The curve exhibits a drop at 2.5% engineering strain and the stress and strain corresponding to this drop are taken to be the values corresponding to fracture, as per ASTM-D-7078M05. The data beyond this point is due to reorientation of fibers and is neglected as per the ASTM-D-7078M05. Considering the data until the point of drop in stress, it can be inferred that the lamina exhibit a substantial non-linearity under shear than under tension, which is expected.

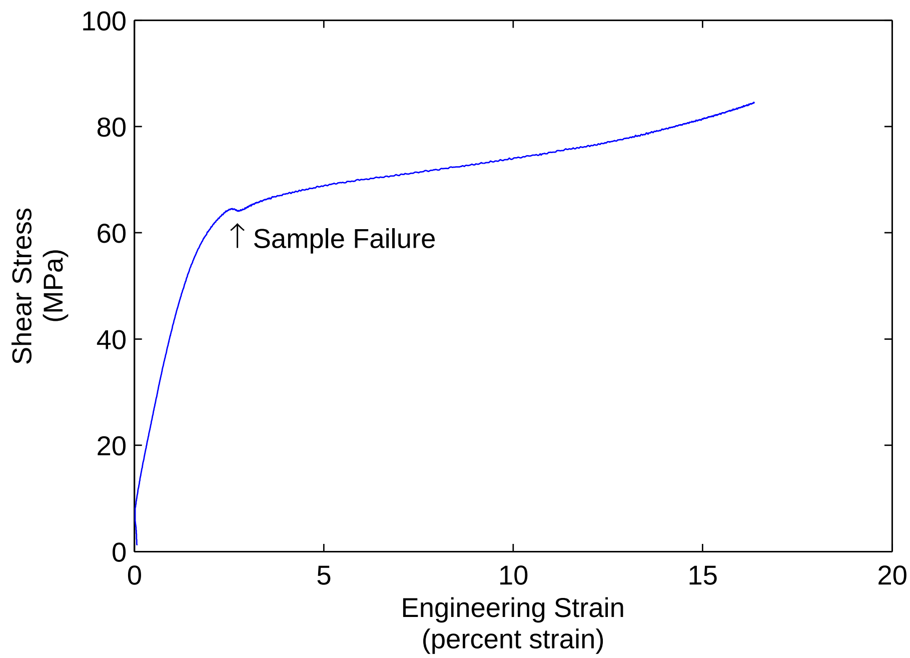

Figure 4.1: τ vs. γ for Sample 5 of ASTM-D-7078 [6] testing

Sample S3 was evaluated for percent twist as recommended in Paragraph 6.3 of ASTM-D-7078M05[6] using Equation 4.1

$$\begin{aligned}
\text{Percent Twist } S3 =& |(G_a - G_b)/(G_a + G_b)| \times 100 \\
=& |(3.60 - 3.57)/(3.60 + 3.57)| \times 100 \\
=& 0.37\%,
\end{aligned} \tag{4.1}$$

where G_a is the shear modulus calculated using strain gages on the front side of the sample and G_b is the shear modulus calculated using strain gages on the back side of the sample. The percent twist of the sample is a measure of how much twist is occurring during the test and is an indicator of damage to fixture, misalignment of the load frame, or improperly manufactured samples.

The value of percent twist from Sample S3 was below the recommended 3% and thus the remaining samples were evaluated using strain gages on one side of the test specimen.

The average value of shear modulus, G^{mean}, was found to be 3.49 GPa with a standard deviation, S_{n-1} of 0.13 GPa for a coefficient of variation, CV, of 3.9%. The material property datasheet for this material did not list an expected G_{12} and thus this value was compared to the shear modulus of another carbon fiber epoxy composite from MIL-HDBK-17[36], which list values for G_{12} ranging from 3.4 GPa to 6.5 GPa. This material is within the range of possible values at the lower end of

Specimen	τ_{12}^{Max}	G_{12}
S1	70.6	3.60
S2	68.7	3.60
S3	68.3	3.27
S4	72.0	3.48
S5	70.8	3.49
Mean	70.1	3.49
S_{n-1}	1.5	0.13
CV	2.2%	3.9%

Table 4.3: Lamina Shear Values

the spectrum.

4.2 End Effects and Design Parameters

The multidirectional laminate was tested in tubular form and steel plugs were used to prevent crushing the ends during gripping. The effect of the specimen geometry and end constraints on the accuracy of the test results are discussed first before presenting the test results for quasi-static testing under tension and torsion.

4.2.1 Effect of Specimen Geometry and Clamped End Constraints

A symmetric and balanced laminate such as the one used in this thesis, $[\pm 45]_{2s}$, would not exhibit any coupling between in-plane and out-of-plane stress/strain components if flat specimen geometry used. However, a tubular geometry would show coupling since the axis of the tube is not co-incident with the neutral axis of the laminate. Herakovich[37] calculates the magnitude of this coupling to be minimal. Vicario and Rizzo[29] state that tube designs for testing should maintain $l/D > 3$ and $t/D \leqslant 0.05$. This thesis exceeds those guidelines and maintains $l/D = 4.9 > 3$ and $t/D = .024 \leqslant 0.05$.

Steel plug inserts were used at either ends of the tubes during testing to prevent crushing of hollow tubes during clamping. However, these plugs constrained the Poisson's contraction of the tubes at the clamped ends. Although the thickness of the laminate at the clamped ends was higher than the gage section to minimize the stress at the clamped ends, the above-mentioned constraint to Poisson's contraction introduced a gradient in gage-section strains.

The variation in transverse (ϵ_x) and longitudinal (ϵ_y) strains was measured using ARAMIS, and is shown in Figures 4.2 and 4.3 respectively.It can be observed that the

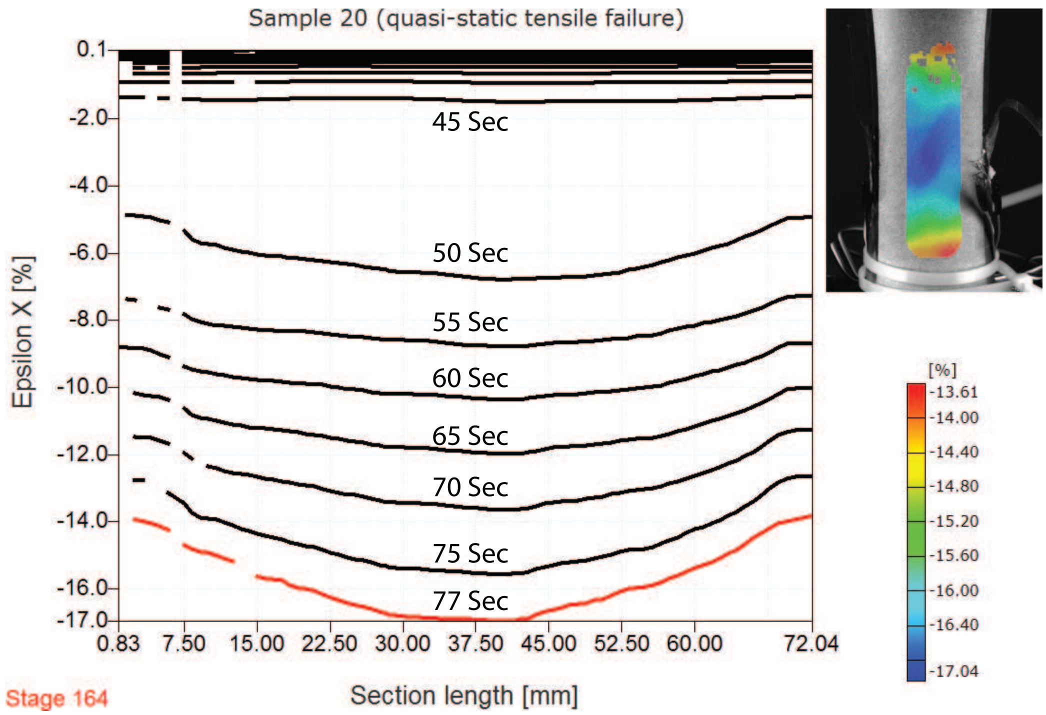

Figure 4.2: Distribution in ϵ_x along the gage length of the test specimen at various times during quasi-static loading

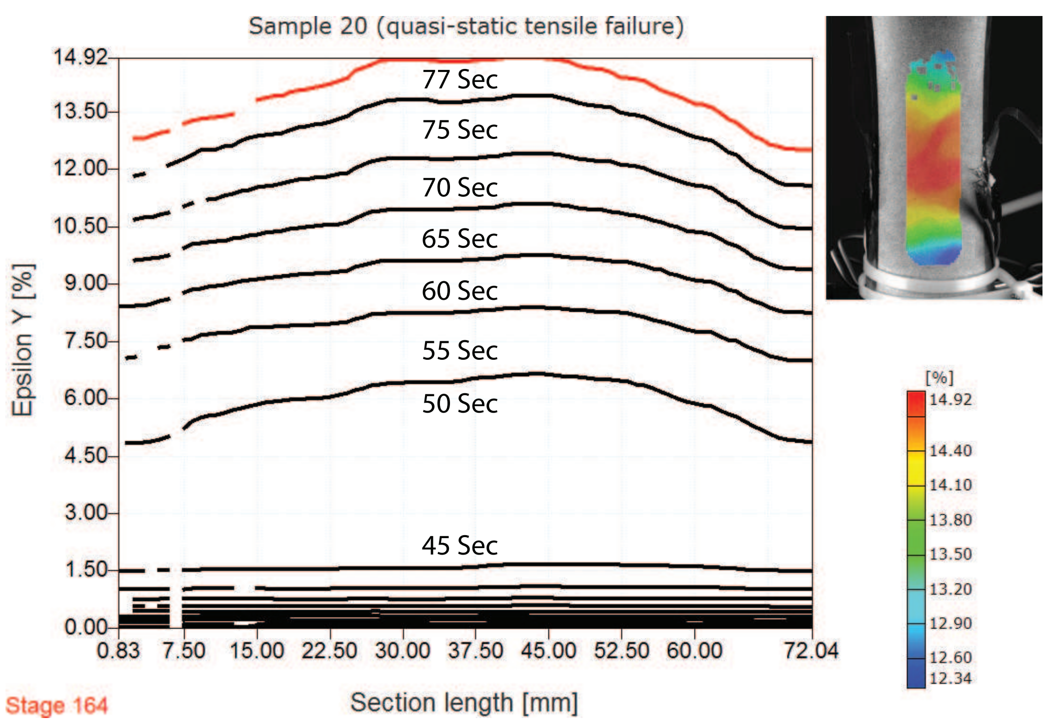

Figure 4.3: Distribution in ϵ_y along the gage length of the test specimen at various times during quasi-static loading

strains are maximum at the center of the gage section and minimum at the ends of the gage section. The difference between the maximum and minimum strains increased with the applied load. It can be inferred that the maximum difference in the strain along the gage section is about 15% for longitudinal strain and 18% for transverse strain. The maximum strain was also observed to be constant along 15–20 mm of the gage section at the center and hence the strain at the center of the gage section was used in determining the modulus of the laminate.

Whitney, Grimes, and Francis[38] investigated what effects the end attachment has on strength and concluded that:

> For angle-ply laminates with a very high effective Poisson's ratio, the stress-strain concentration at the gage-section end of the tab does not appear from the shell analysis to be large, but severe increases are predicted in the tube under the tab.

.

The tests conducted in this thesis show peak stresses and failure initiation occurring in the middle of the gage section. This can be seen in Figure 4.4. When tests have not been stopped immediately following failure and the sample is allowed to separate in two halves, final failure does occur under the tab (see Sample 16 in Figure 4.4) supporting Whitney's[38] calculation of a stress-strain concentration. The fact that Sample 16 begins failure in the gage section is supported by the Aramis image shown in Figure 4.5.

Figure 4.4: Samples 16 and 21 showing gage section failure with and without complete separation

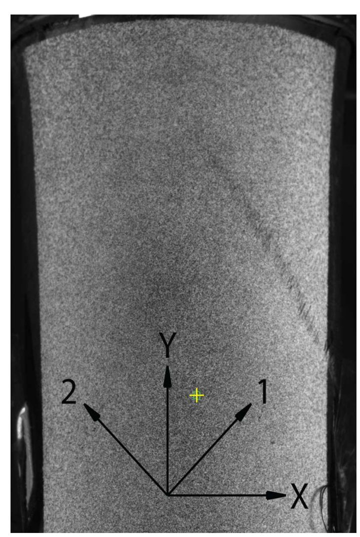

Figure 4.5: Sample 16 showing crack growth in the gage section during fatigue testing

4.3 Quasi-Static Test Results

Laminate tubes were subjected to quasi-static loading to failure under tension (Sample 20), torsion (Sample 7) and combined tension and torsion (Samples 9 and 11). Results of these tests are summarized in Table 4.4 and discussed in detail in the following sections.

Sample	Type	σ_{yy} at failure (MPa)	τ_{xy} at failure (MPa)
9	1	199	67
11	1	242	79
20	4	233	0
7	5	0	325

Table 4.4: Quasi-static test results for laminate tube samples

4.3.1 Tension Test Results

Experimental stress-strain curve for Sample 20 loaded in tension is shown in Figure 4.6. The sample exhibited a transition from linear to non-linear stress-strain around 100 MPa, which can be observed clearly in Figure 4.6. Figure 4.7 shows the initial portion of the curve where the strain data from four different sensors (Instron cross-head displacement, ARAMIS, left strain gage, and right strain gage) show good agreement during the initial loading phase.

This highlights the accuracy of strain measurement using ARAMIS. The strain gages on both the left and right sides of the sample debonded from the sample beyond $\sim 140\ MPa$ when the strain on the sample exceeded the strain limit for the strain gages. After 30000 $\mu\epsilon$, at any given load level, the ARAMIS plot shows higher strain values than calculated from the cross-head displacement. While ARAMIS determines the strain from a small computational length ($^1/_8$ inch) at the center of the sample, the cross-head displacement strain is averaged over the entire length of the tube. This is to be expected since a strain gradient was observed, as shown in Figure 4.3, along the gage length with the maximum strain at the center of the sample. The averaging over the entire gage length resulted in a lower strain than in the case of ARAMIS. Sample 20 reached a maximum normal stress, σ_{yy}, of 233 MPa before failure.

The non-linearity observed in Figure 4.6 beyond 130 MPa is due to damage that develops in the specimen during loading. The first damage mode to develop is matrix cracking parallel to fibers in the [+45] and [−45] plies as shown in Figure 4.8(a). This damage mode develops first in the inner plies and then develops in the outer plies at load levels closer to the failure load. This damage develops rapidly causing a sudden increase in strain resulting in the linear - non-linear transition beyond 100 MPa.

The rapid development of strain was captured by the ARAMIS system during the test. A plot of the global Y direction strain as a function of time for Sample 20 is shown in Figure 4.9, and plot of the global XY direction strain as a function of time for Sample 20 is shown in Figure 4.10. The plots in Figure 4.9 and 4.10 were

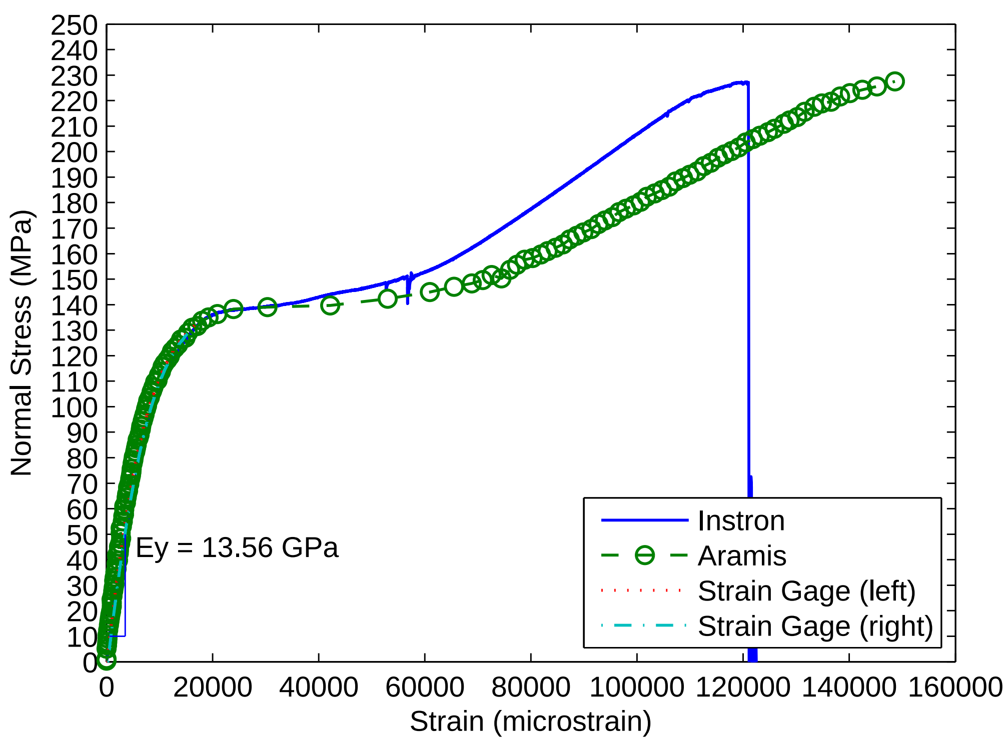

Figure 4.6: Stress vs. strain plot of Sample 20 loaded in quasi-static tension to failure

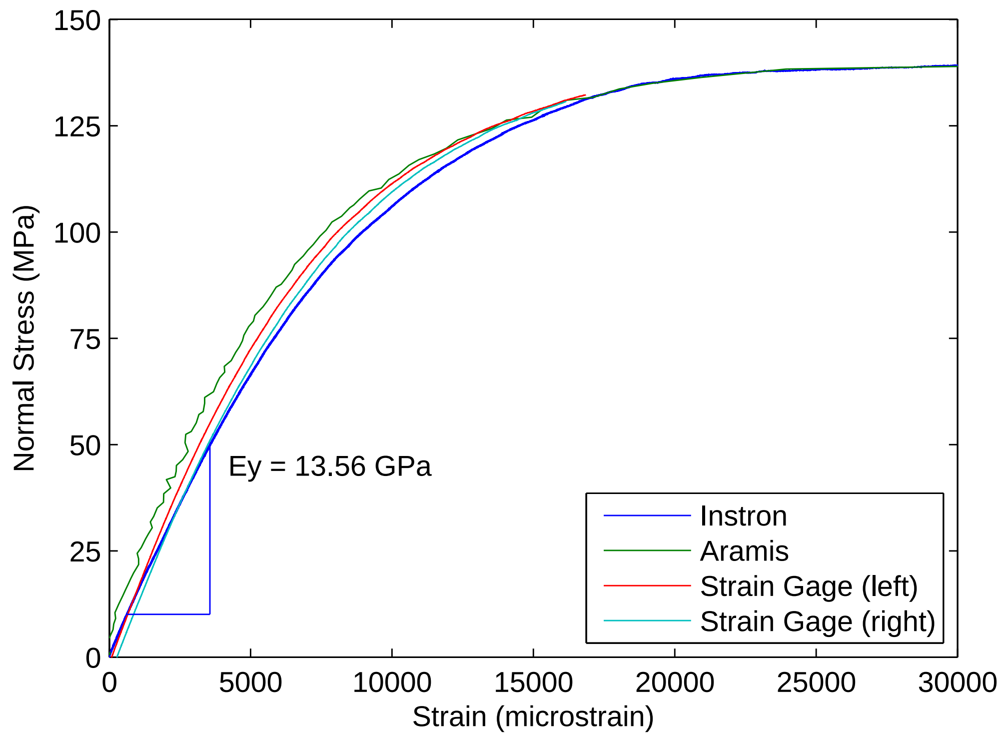

Figure 4.7: Stress vs. strain plot of sample 20 in quasi-static tension until debonding of the strain gage

(a) Interior Surface

(b) Exterior Surface

Figure 4.8: Failure surface of Sample 20

generated using the strain from a single point on the sample, Stage Point 0, shown on the right of the figure. The image of the sample on the right of the figure shows the strain distribution at the end of the test corresponding to the vertical red dashed line shown in Figures 4.9 and 4.10.

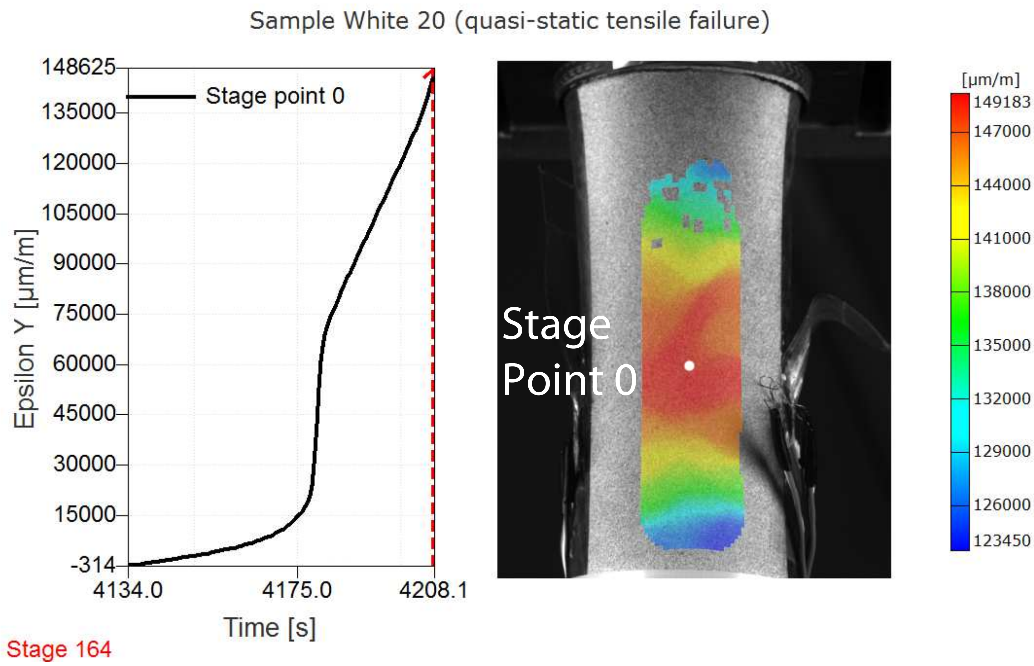

Figure 4.9: Sample 20 ϵ_y just before failure during quasi-static tension test

In order to confirm that the change in the stress-strain curve is due to the damage and not due to non-linear constitutive behavior of the lamina, the stress-strain curve of the laminate was predicted. This prediction was done using the lamina elastic properties assuming no damage through an incremental analysis, and is presented in Appendix B. The predicted curve is compared with experimental curve with very good correlation in the linear region. While the predicted longitudinal tensile modulus of the tube is 13.2 GPa, as per Equation (A.31), the experimental modulus is 13.6 GPa, confirming the accuracy of the prediction. Note that the last predicted data point in the lamination theory corresponds to the 5% limit imposed by the ASTM standard on the maximum experimental shear strain obtainable from shear testing (see paragraph 11.9 of ASTM-D-7078[6]). Substantial deviation of the experimental curve from the curve predicted using the no-damage assumption confirms that the non-linearity observed in the experimental stress-strain curve is due to progressive damage development during loading beyond $\sim 100\ MPa$.

Beyond $\sim$ 40000 microstrains, the modulus of the stress-strain curve starts to increase. This is due to the gradual rotation and re-alignment of the fibers along the test axis, due to progressive damage.

Since the laminate is balanced and symmetric, the tensile load should not introduce shear strain. However, the measured shear strain is observed to fluctuate by $\pm$90 microstrains between 4134 and 4175 seconds in Figure 4.10. This is due to the coupling between the linear and rotary actuators, which will be discussed in detail in Section 4.3.2. However, a sharp increase in shear strain is observed beyond 4175 seconds in Figure 4.10 when substantial damage starts to occur. With increasing damage, localized reorientation of fibers occurs resulting in loss of balanced layup and shear strain, due to material coupling between the normal load and the shear strain. The sudden increase in shear strain in Figure 4.10 concomitant with the large

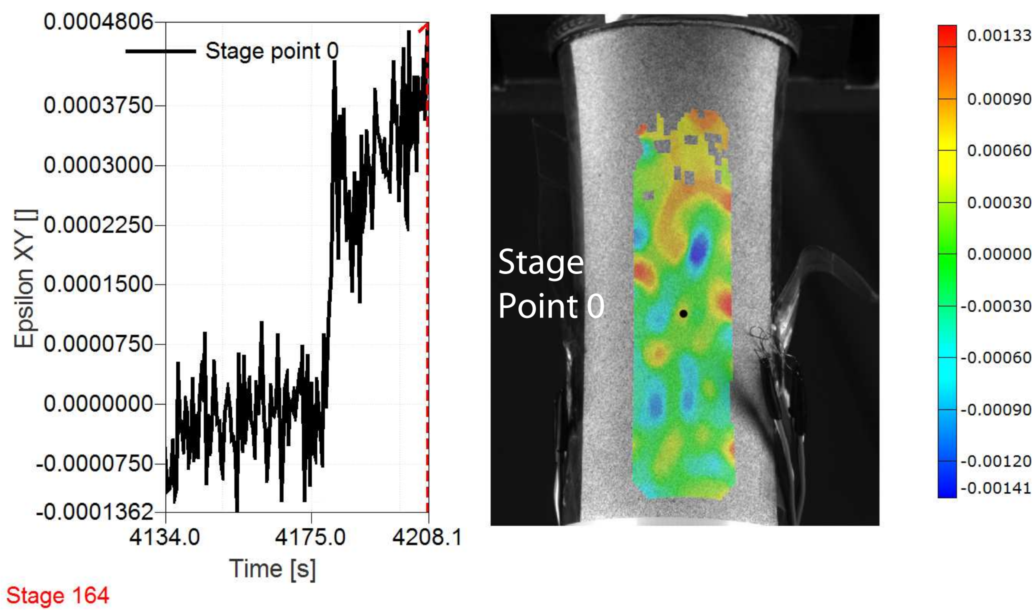

Figure 4.10: Sample 20 ϵ_{xy} just before failure during quasi-static tension test

increase in axial strain in Figure 4.9 supports this supposition. Although the symmetric layup precludes any coupling between normal and shear forces and deformation, the tube geometry used in this study can result in a very weak coupling. However, the magnitude of strain due to this weak coupling will be negligible compared to the magnitude observed in Figure 4.14. Hence, the rotation of the fibers due to damage is believed to be the reason for increase in shear strain and in the axial modulus of the tube.

Failure of Sample 20 was in the grip section close to the chamfered edge of the steel plug, as illustrated in Figure 4.11. It should be noted that Figure 4.11 is that of Sample 9 and shows some delamination which does not occur in Sample 20, as observed in Figure 4.8 (b).The failure surface showed clean fiber failure, which was

Figure 4.11: Failure completion at the chamfered end of the steel plug in Sample 9

not precipitated by any delamination or matrix cracking propagating from the gage section suggesting a sudden failure. A large acoustic emission (bang) heard during this failure event supports this conclusion. All specimens loaded in tension failed in this way. The Poisson's ratio, ν_{xy}, for the tubular laminate specimen is 0.89, which results in a substantial reduction in the diameter of the sample. Due to the use of plugs to load the specimens, the tubes were constrained from contracting due to Poisson's effect in the grip section. Maximum contraction occurred at the center of the specimen due to a lack of such constraint. As a result of damage in the specimens loaded to failure, the transverse deformation due to Poisson contraction is not recovered. This lack of recovery results in the pseudo-necking observed in Figure 4.8b. The stress concentration at the grip due to Poisson's contraction is believed to be the reason for the failure of the tubes near the gripped region.

4.3.2 Type V Torsion Loading

The shear stress-strain plot for Sample 7 loaded in torsion is shown in Figure 4.12. The shear strain measured using ARAMIS varied marginally from the shear strain measured using strain gages. The strain measured from ARAMIS corresponds to a point on the front of the sample (between the two strain gages), while the strain from the stain gage corresponds to the average strain determined over the area of the strain gage. This is believed to be the reason for the lower strain measured using strain gages. The shear modulus of the laminate tube was determined by taking the slope of the linear portion of the stress strain curve, as shown in Figure 4.12. Due to the difference in strain, the shear modulus determined using ARAMIS data is slightly higher than the modulus determined using the strain gage data.

Unlike non-linear tensile stress-strain curve, the shear stress-strain curve was linear for the major portion of the applied torsional load. This is a result of the high stiffness fibers orientated at ±45 degrees taking the majority of the load away from the matrix. Owing to this load sharing by the fibers, normal or shear failure of the matrix (i.e. transverse cracks) were not observed; the interior surface of Sample 7 was relatively smooth as observed in Figure 4.13(b). This is in contrast to the interior of Sample 20 that displayed extensive damage at failure sites, shown in Figure 4.8(a). Due to the orientation of the fibers at 45° to the loading axis, the shear modulus of the $[\pm 45]_{2s}$ tubes (46 GPa) are much higher than the axial modulus of the tubes (13 GPa). The sample fractured at a maximum shear stress of 327 MPa. Since this fracture plane was within the gage section at 45° to the tube axis, fibers in one set of plies (+45) would have fractured while the matrix in the other set of plies (-45) would have cracked

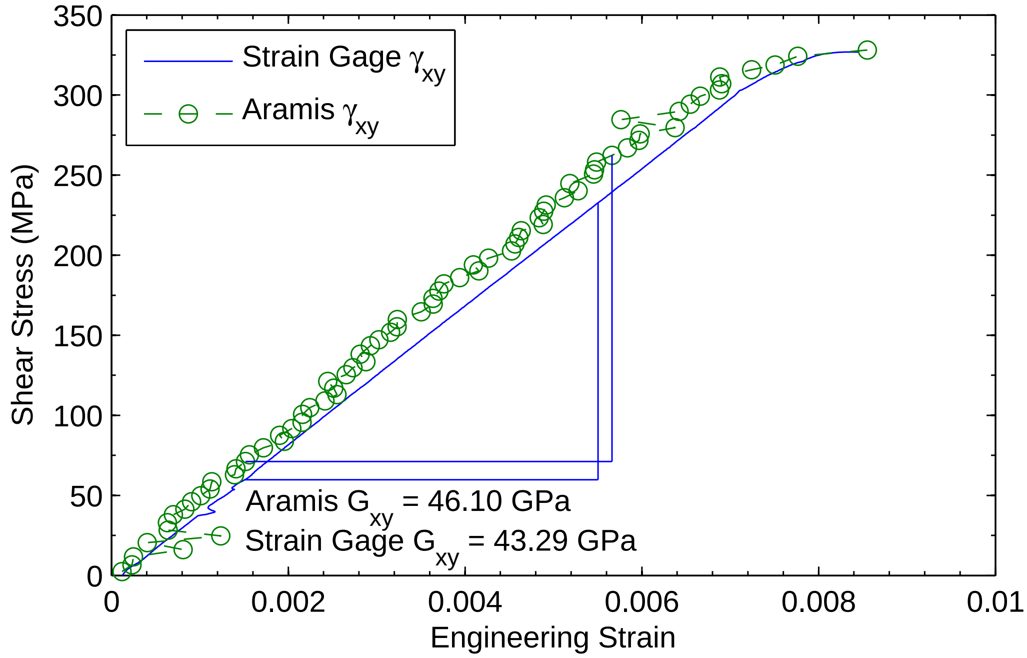

Figure 4.12: Stress vs. Strain plot of Sample 7 in pure torsion

(a) Exterior (b) Interior

Figure 4.13: Exterior and interior surfaces of Sample 7

parallel to the fibers in those layers, resulting in the observed single fracture plane. Fiber failure requires higher load due to higher strength of the fibers. The failure surface area in Sample 9 was higher than that in Sample 20, suggesting a largerf number of fibers failing in Sample 9 than in Sample 20. This is believed to be the reason for the higher strength in torsion than in tension.

A plot of the global shear strain as a function of time for Sample 7 is shown in Figure 4.14, and plot of the global axial strain as a function of time for Sample 7 is shown in Figure 4.15. The plots in Figure 4.14 and 4.15 were generated using the strain from a single point on the sample, Stage Point 0, shown in Figures 4.14 and 4.15. These Figures show the strain distribution at peak strains prior to failure of the sample, corresponding to the vertical red dashed line in Figures 4.14 and 4.15.

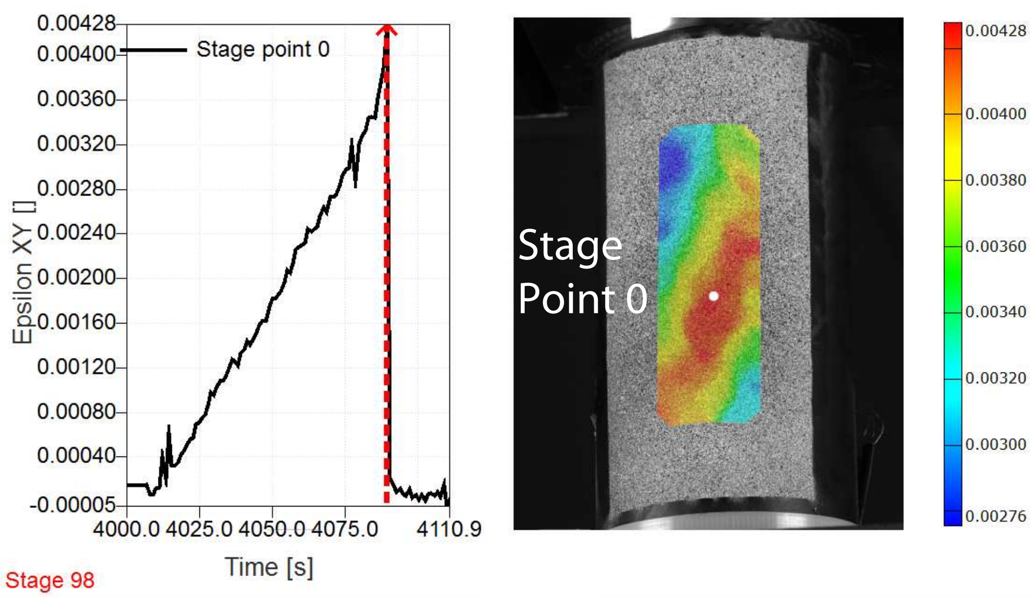

Figure 4.14: Sample 7 ϵ_{xy} at peak strain prior to failure

It can be inferred from Figures 4.14 and 4.15 that the torsional load resulted in compressive axial strain, suggesting a coupling between torsional load and normal strain. As discussed in the previous section, the material coupling should be marginal. The torsional strain of 1600 microstrains observed after fracture is believed to be due to the damage in the sample after fracture.

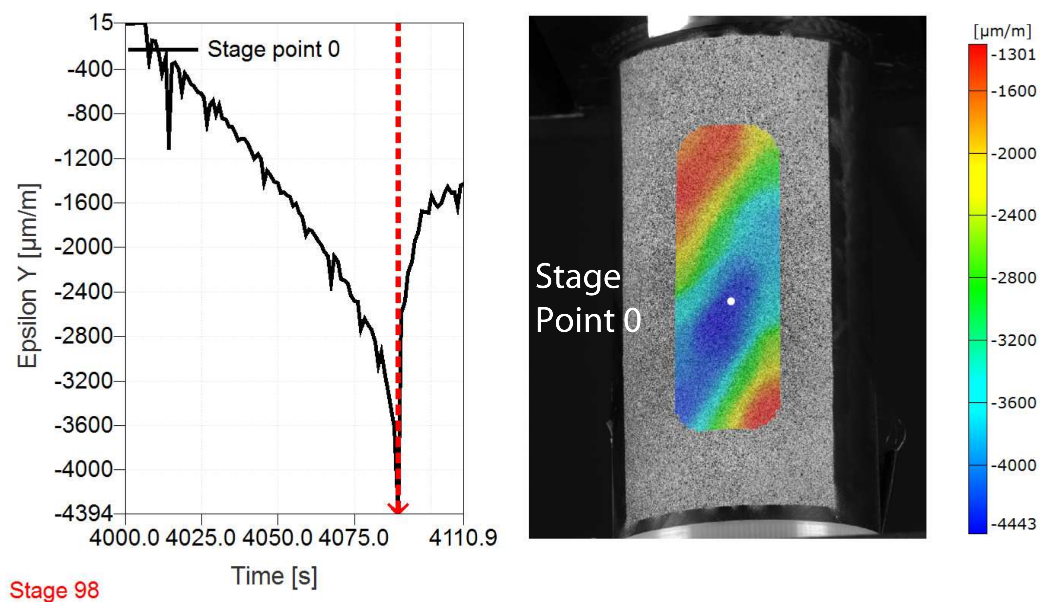

Figure 4.15: Sample 7 ϵ_y at peak strain prior to failure

In order to understand this, additional tests were completed using 1018 steel, where such a material coupling is not possible. One end of the sample was clamped to the lower moving cross-head, while the other end was not clamped. Maintaining both the rotary and linear actuators under position control, the sample was rotated in steps of 0.1 degrees and the resulting axial position of the sample was monitored using ARAMIS. The linear actuator was commanded to maintain the position of the cross-head at the same location while the torque was applied. Although the cross-head position hardly changed in the range of 0.004 mm, the position of the sample, as measured by the ARAMIS, changed as shown in Figure 4.16.

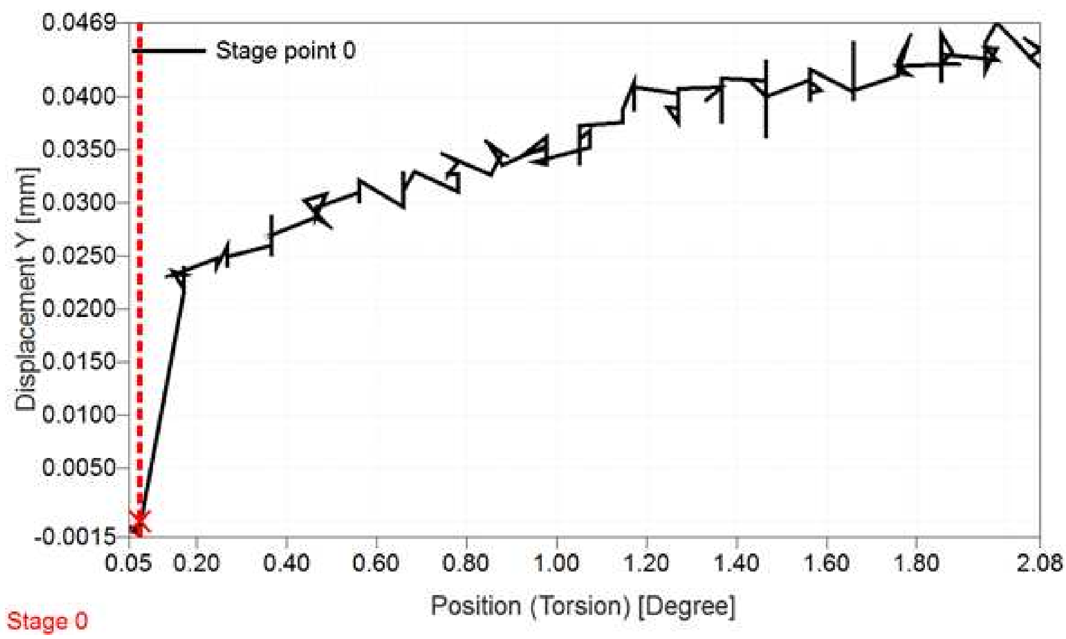

Figure 4.16: Linear position change of 1018 steel during rotation

During the first rotational angle increment of 0.1 degree, the sample's position suddenly changed by 0.024 mm. The positive value corresponds to downward displacement. The position of the top grip was also measured by ARAMIS and changed by similar amount and hence, there was no relative displacement between the top grip bottom and the sample during this rotation. However, the sample's axial displacement, relative to the top grip, increased further by 0.02 mm as the rotational angle was increased to 2 degrees. Since the position of the linear actuator position did not change during this rotation through 0.1–2 degrees, the observed displacement of the sample must be relative to the position of the linear actuator (i.e., the position of the moving cross-head attached to the linear actuator shown in the schematic of the load frame in Figure 4.17). The cause for this relative displacement is unknown at this time and is believed to be related to the machine design; elimination of this displacement was beyond the control of the author.

When the top end of the sample is gripped, this relative displacement results in a tensile load in the specimen. For example, the steel sample was clamped between the hydraulic grips and loaded to 500 Nm while commanding the linear actuator to maintain its position. The resulting torque, rotational angle, axial load, and axial position of the moving cross-head are plotted in Figure 4.18. Although the axial position of the moving cross-head (and hence the linear actuator) was maintained around “zero” , the sample recorded a maximum tensile force of 2583 Newtons due to the relative downward motion of the sample with respect to the moving cross-head. The strain recorded in the sample using the strain gages is plotted in Figure 4.19.

The axial strain (ϵ_Y) is positive and corresponds to a relative displacement of 0.006 mm over a gage length of 148.08 mm. The observed difference between the strains recorded by the strain gages on the right and left sides of the sample suggests some level of bending of the sample. The lateral strain (ϵ_X) is negative and due to Poisson’s contraction.

The above experiment clearly points to coupling between the linear displacement and the rotational actuation.

A third test, mimicking the torsional testing of Sample 7, was completed using the steel sample. The sample was torqued to 500 N-m, while commanding the linear actuator to maintain zero load. The resulting data is plotted in Figure 4.20.

Due to the tensile load recorded by the load cell caused by the relative displace-

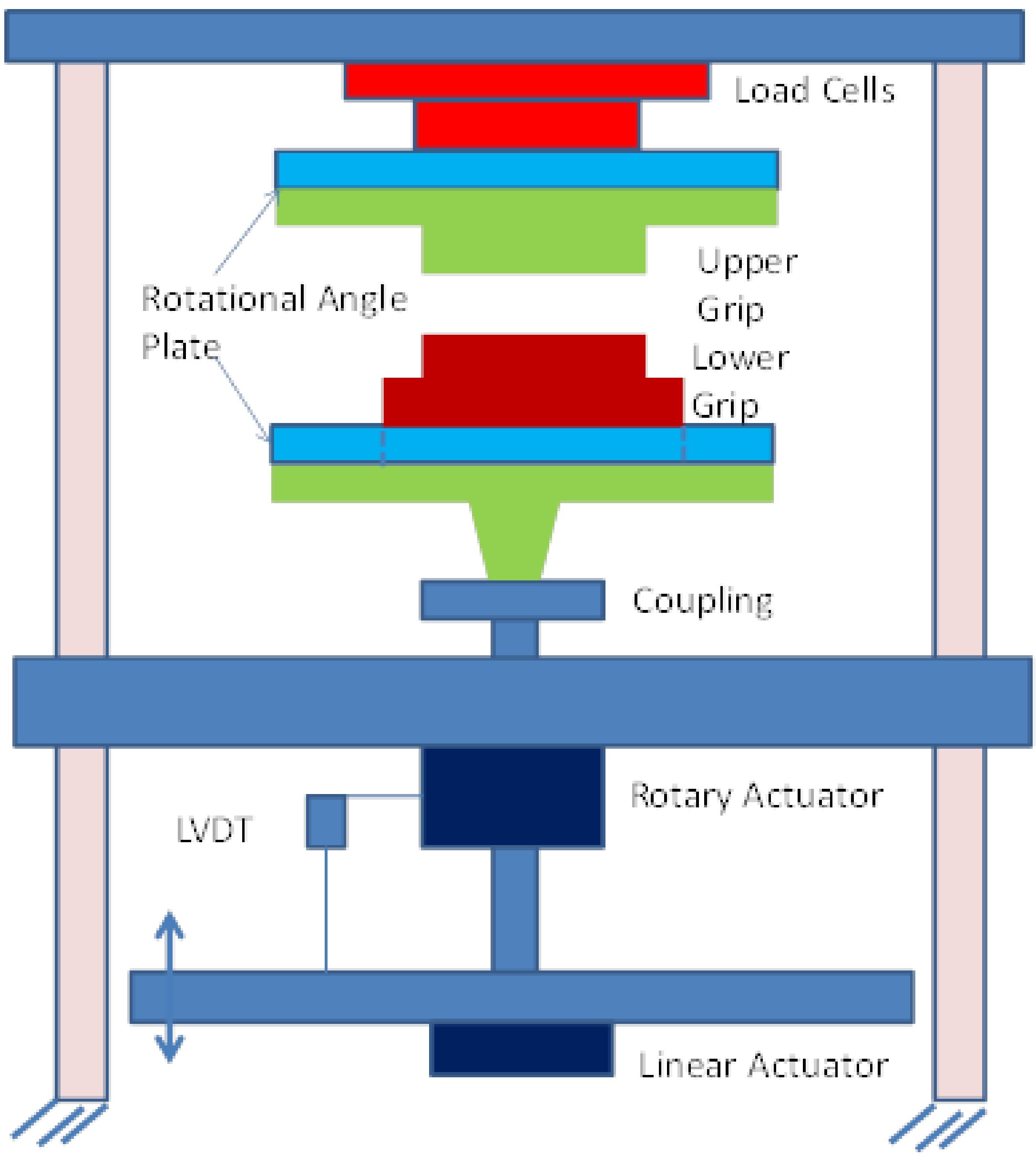

Figure 4.17: A schematic of the Instron 8822 load frame

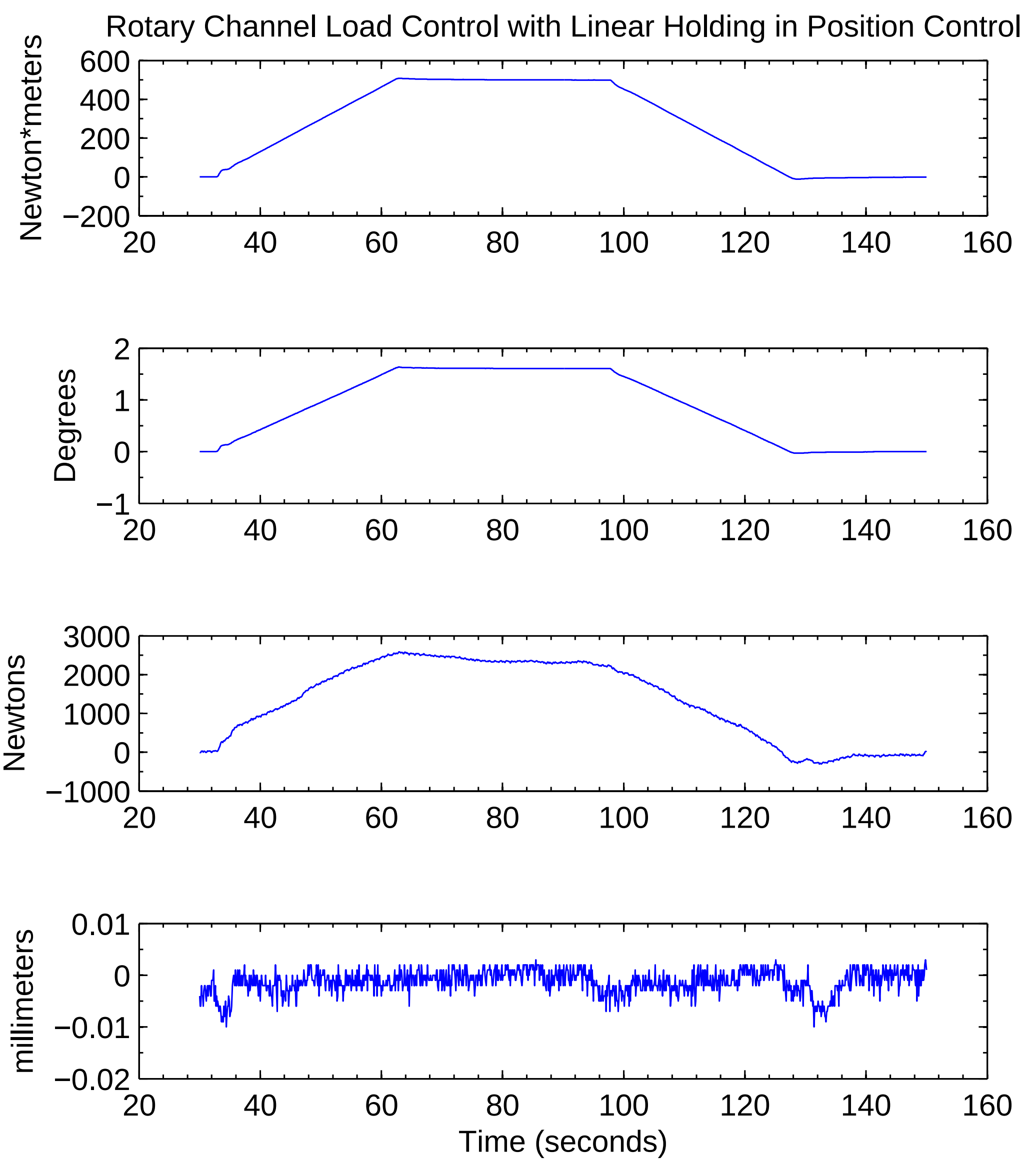

Figure 4.18: The load, torque, cross-head displacement, and angle of twist recorded during torque loading of a 1018 steel specimen with the rotary actuator under load control and linear actuator under position control

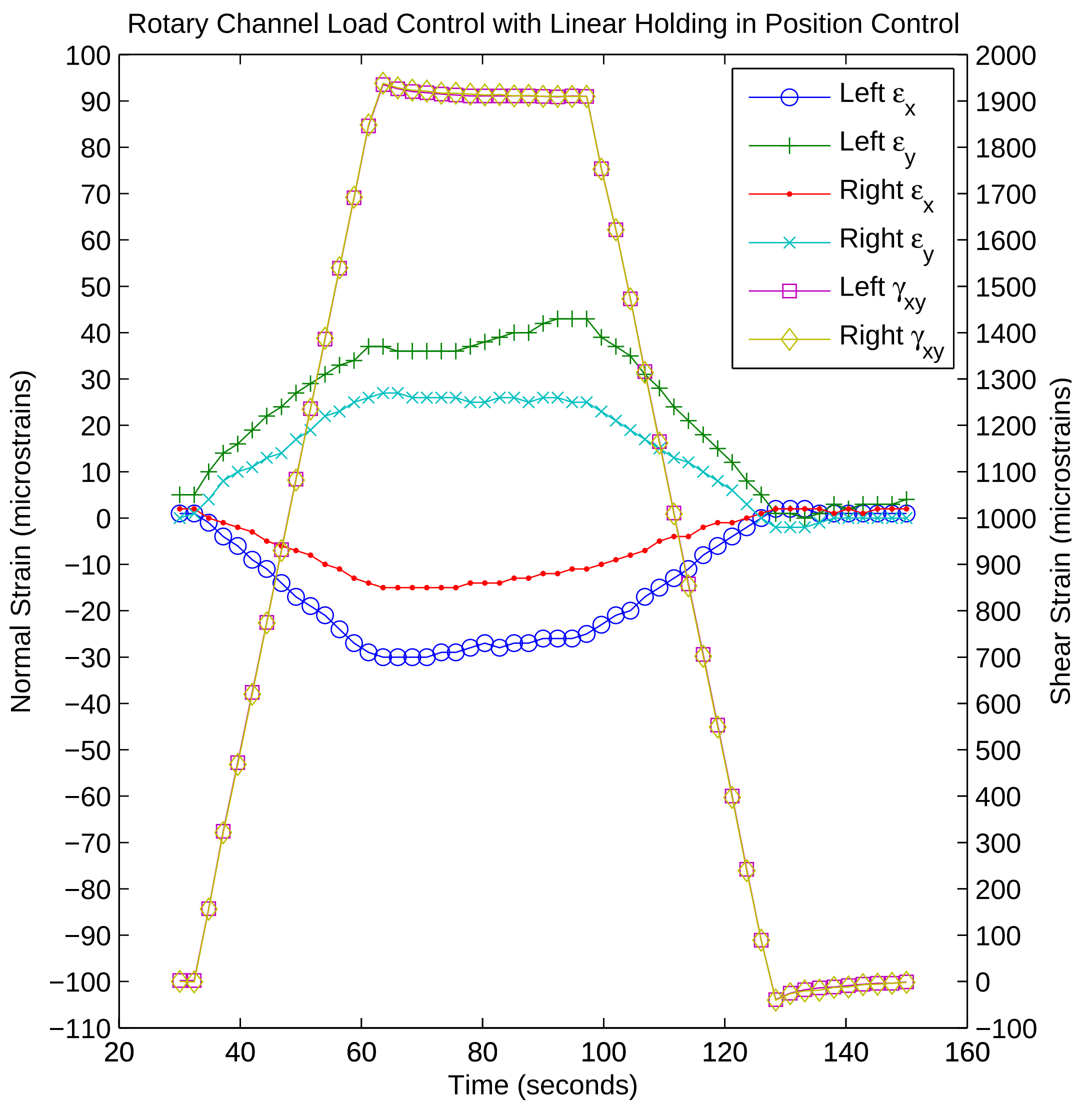

Figure 4.19: The strains recorded during during torque loading of a 1018 steel specimen with the rotary actuator under load control and linear actuator under position control

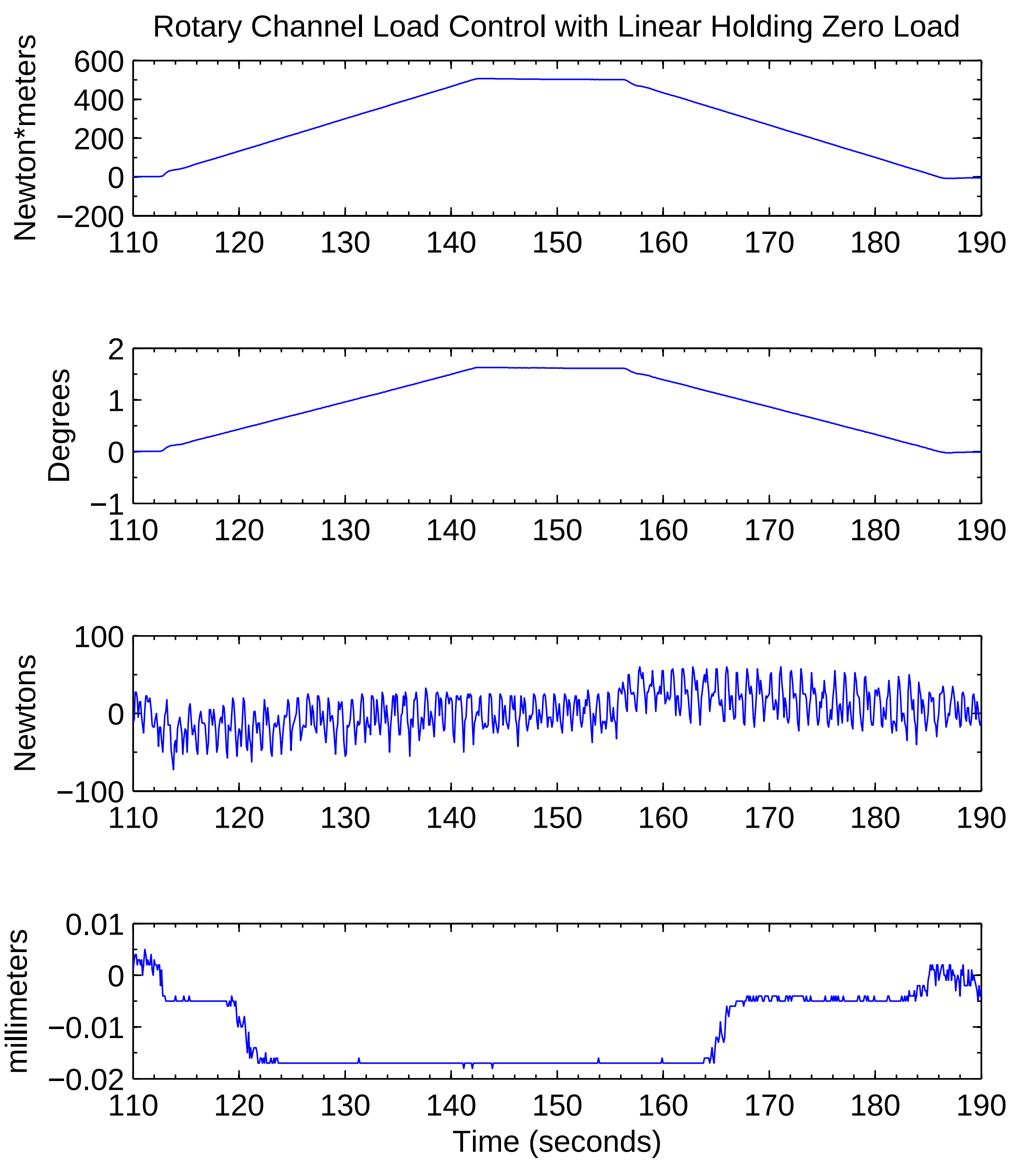

Figure 4.20: The load, torque, cross-head displacement, and angle of twist recorded during torque loading of a 1018 steel specimen with the rotary actuator under load control and linear actuator under load control

ment of the sample, with respect to the position of the moving cross-head, in response to the applied torque, the linear actuator would move up the cross-head in the negative direction to reduce this load to zero. This is observed in Figure 4.20. The strain on the sample measured using the strain gage was close to zero as shown in Figure 4.21.

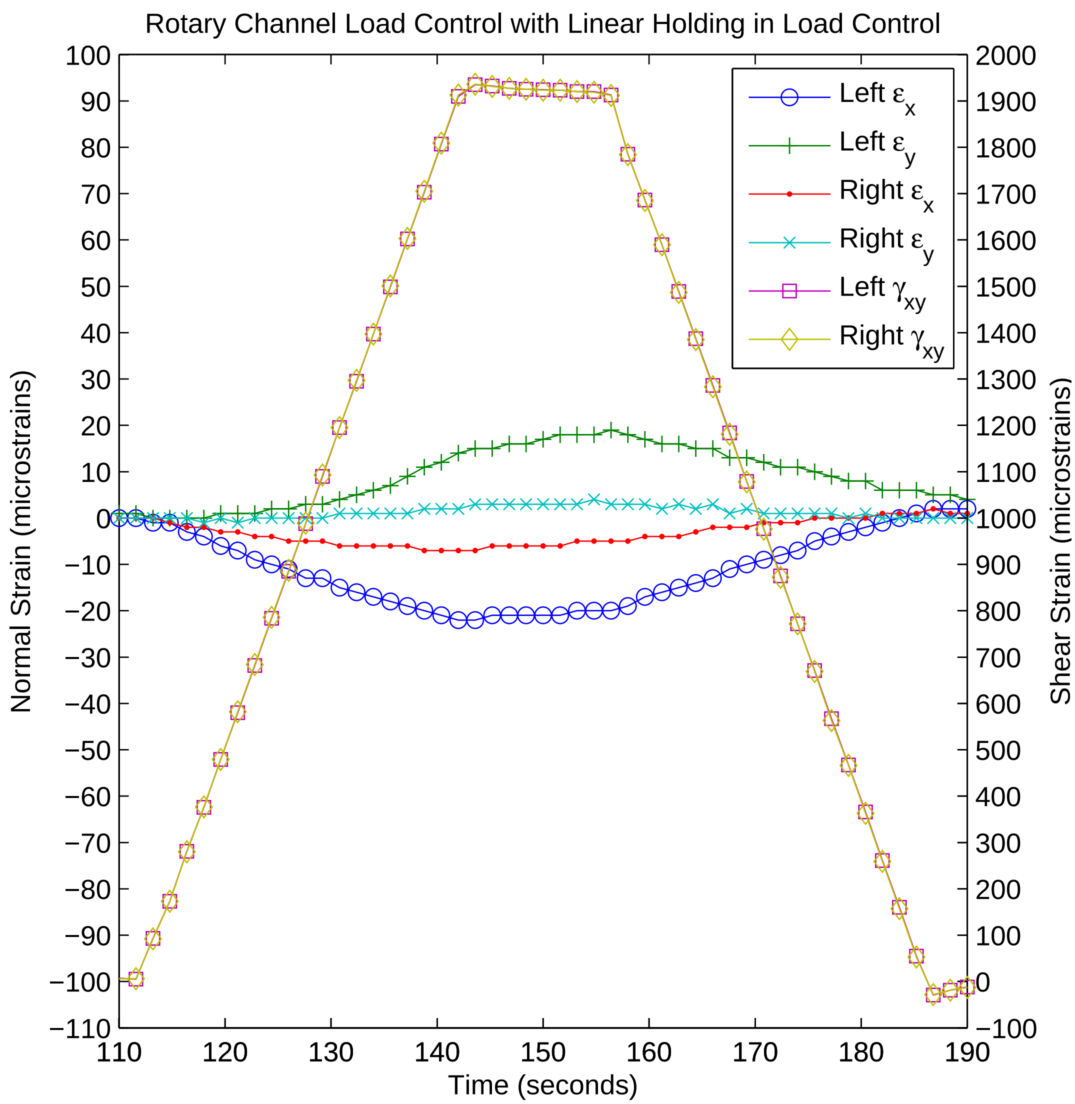

Figure 4.21: The strains recorded during torque loading of a 1018 steel specimen with the rotary actuator under load control and linear actuator under load control

Such coupling between rotational angle and linear actuation was also observed as shown in Figure 4.22. The steel sample was loaded to 100 kN while the rotary actuator was commanded to maintain the position of zero torque.

The strains measured using the strain gages are plotted in Figure 4.23. The measured shear strain due to this coupling is negligible.

A similar increase in the axial displacement of the moving cross-head due to the coupling discussed above, was observed during torsion testing of composite Sample 7, as shown in Figure 4.24, with the linear actuator commanded to maintain zero axial load on the sample.

Ideally, this should have resulted in zero axial strain in the sample. The negative axial strain observed can be explained as follows. Consider the a sample of L_0, shown in Figure 4.25 (a), is subjected to a torque while not allowing the cross-head positions to change. This will lead to extension of the sample by δ_S to a new length of L_1, as shown in Figure 4.25 (b), due to coupling discussed in the previous paragraphs. This will introduce a tensile force of N in the sample.

If the linear actuator is commanded to maintain zero load, then the moving cross-head will move up by δ_C to introduce a compressive force, N_c such that

$$\begin{gathered} P = N - N_c = 0 \\ N_c = N \\ \delta_c \frac{EA}{L_1} = \delta_s \frac{EA}{L_0}. \end{gathered} \tag{4.2}$$

It is assumed that the stiffness of the assembly of grips, coupling, and shafts is much greater than that of the sample; hence, the deflection is assumed to only occur in the sample.

$$\delta_c = \delta_s \frac{L_1}{L_0} = \delta_s \frac{L_0 + \delta s}{L_0} = \delta_s + \frac{{\delta_s}^2}{L_0}. \tag{4.3}$$

Note that δ_c is upward while δ_s is downward; alternatively, while δ_c is the contrac-

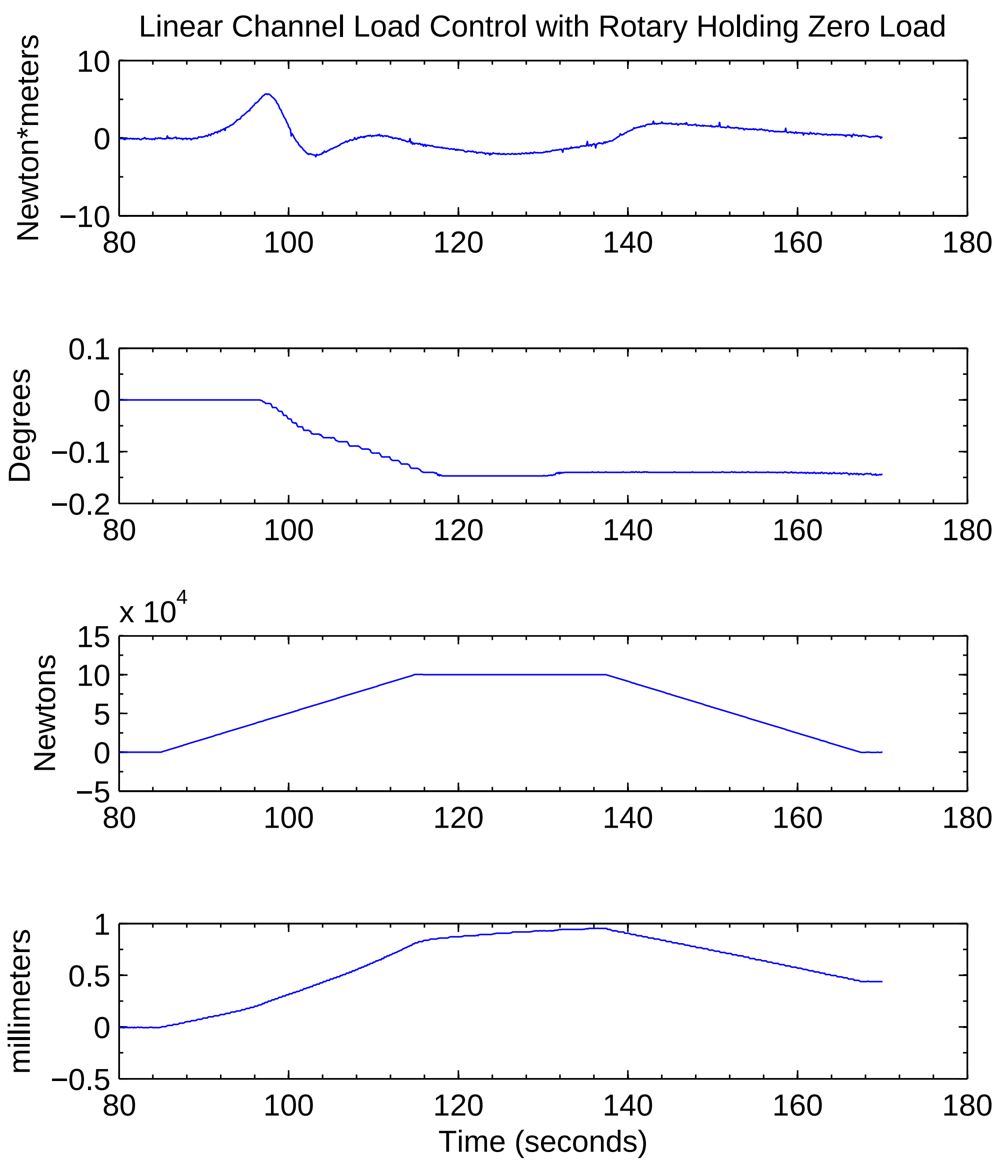

Figure 4.22: The load, torque, cross-head displacement, and angle of twist recorded during tension loading of a 1018 steel specimen with the rotary actuator under load control and linear actuator under load control

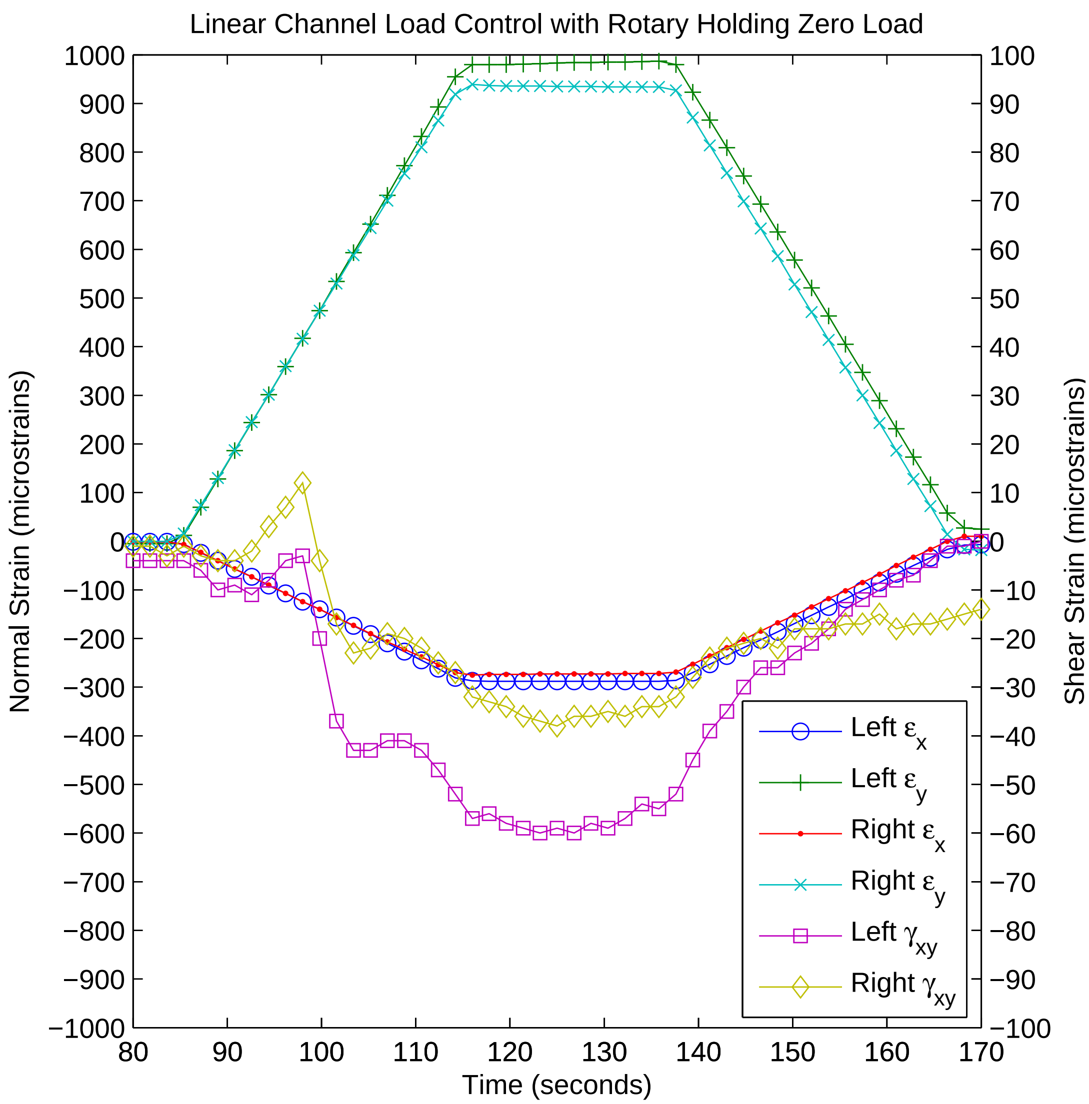

Figure 4.23: The strains recorded during tension loading of a 1018 steel specimen with the rotary actuator under load control and linear actuator under load control

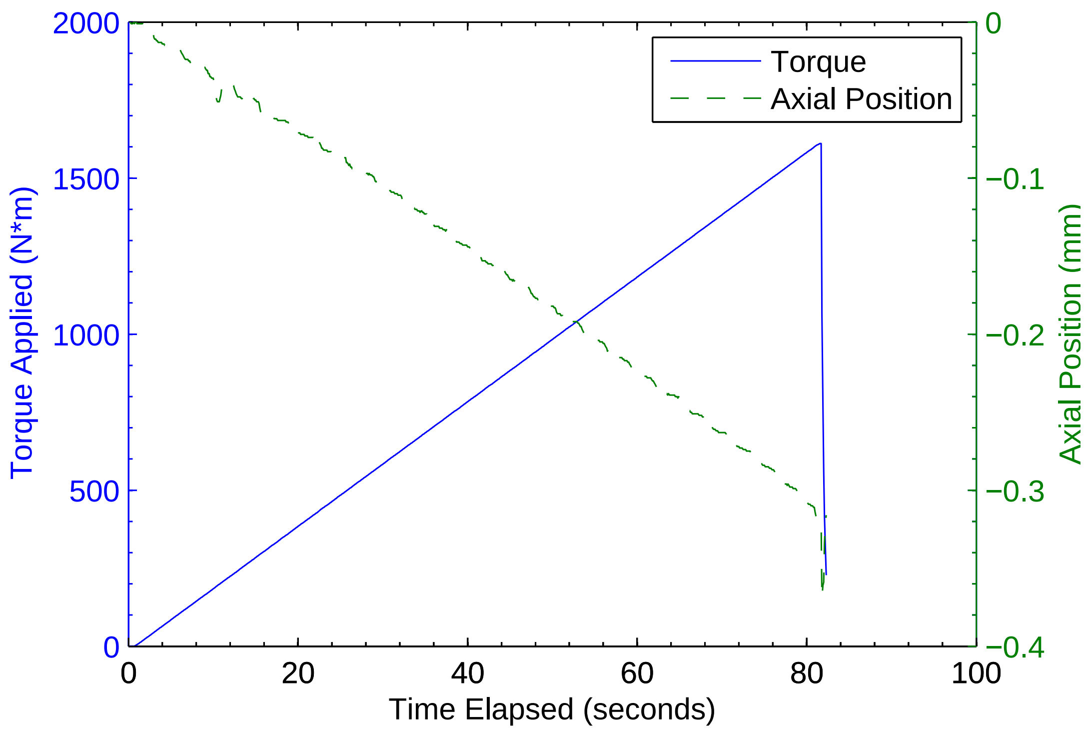

Figure 4.24: Axial cross-head position and torque during quasi-static testing of Sample 7

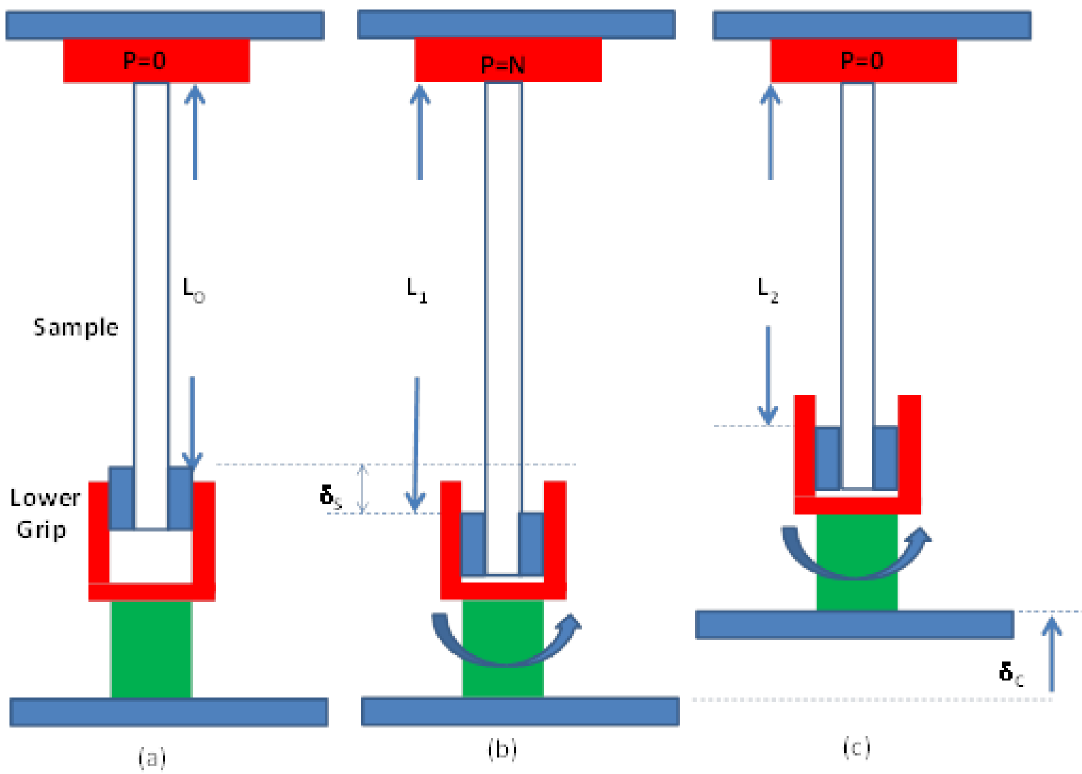

Figure 4.25: A schematic representing machine coupling between the rotary and linear actuators

tion in the sample due to upward movement of the cross-head, δ_s is the extension in the sample due to coupling. Hence, the contraction should be more than that of the extension to maintain a zero load on the load cell.

Now,

$$L_2 = L_1 - \delta c = L_1 - \delta s - \frac{{\delta_s}^2}{L_0} = L_0 - \frac{{\delta_s}^2}{L_0}. \tag{4.4}$$

Thus, the final length of the sample after compensating the load to zero is less than the original length. The net strain on the sample is

$$\frac{L_2 - L_0}{L_0} = -\frac{{\delta_s}^2}{{L_0}^2}. \tag{4.5}$$

This strain is compressive while the load registered by the load cell is zero as shown in the Figure 4.26.

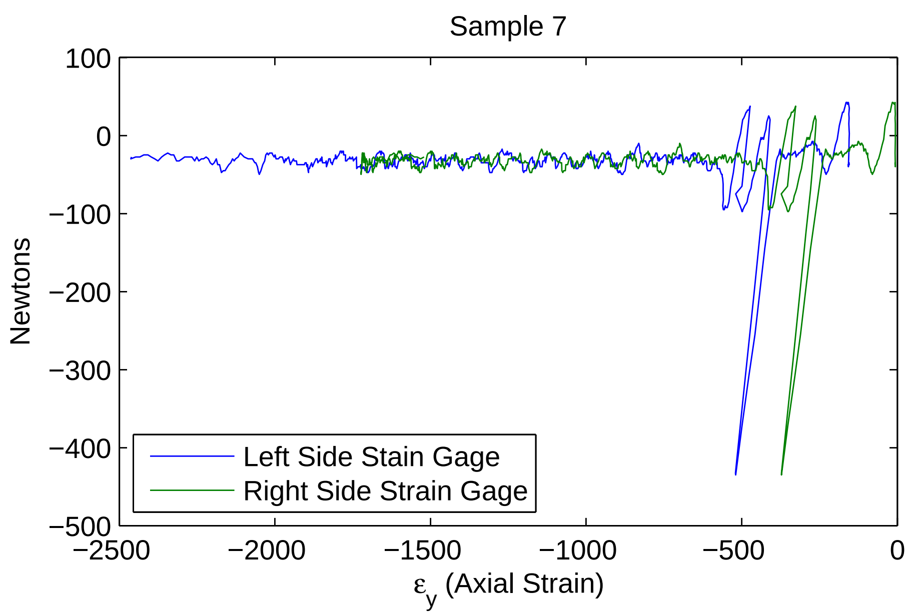

Figure 4.26: The axial load and the axial strain measured on 1018 Steel sample due to machine coupling during torque loading

However, the compressive strain on the sample suggests that there must be internal stress (akin to a residual stress) within the sample, even though the load cell reading is zero. This can be understood from the following simplification of the loads acting on the sample when the cross-head is moved-up to maintain zero load, as shown in Figure 4.27.

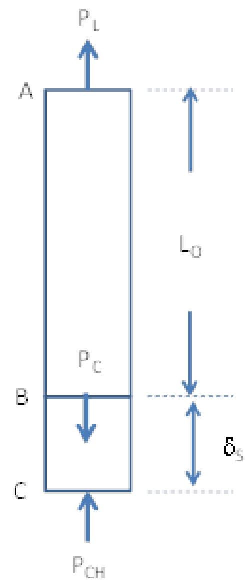

Figure 4.27: A free body diagram for the 1018 steel sample illustrating the introduction of axial compressive load due to machine coupling

Here, P_L is the load exerted by the sample on the load cell, P_C is the load due to coupling, P_{CH} is the compensating load applied by the linear actuator, L_0 is the original length of the sample, and δ_s is the deformation in the sample in response to P_C. A simple force balance will reveal that $P_L = 0$, $P_C = P_{CH}$, and the internal forces in sections AB and BC of the sample are $P_{AB} = 0$ and $P_{BC} = P_C$. Hence, although the load recorded by the load cell is zero, there will be internal force and stress within the sample.

The total deformation after application of P_{CH} is

$$\delta = \delta_{AB} + \delta_{BC} = \frac{P_{AB} L_0}{EA} + \frac{P_{BC} \delta_S}{EA} = -\frac{P_{BC} \delta_S}{EA} = -\frac{\sigma_{BC} \delta_S}{E} = -\frac{\delta_s \delta_s}{L_0} = -\frac{{\delta_s}^2}{L_0}. \quad (4.6)$$

The total strain on the sample as measured by the strain gage and ARAMIS (using the initial sample length of L_0) is

$$\epsilon = \frac{-\frac{\delta_s{}^2}{L_0}}{L_0} = -\frac{\delta_s{}^2}{L_0{}^2}. \tag{4.7}$$

This residual compressive strain is the same as the strain determined using Equation 4.5 by a slightly different analysis. Thus, this strain is proportional to the internal compressive stress in the sample (referred here afterwards as residual stress). This strain and internal stress are shown to be active in a portion of the sample in the above schematic, as the coupling stress and strain are assumed to be due to displacement within the bottom grip. However, if they are introduced due to the displacement within both the top and bottom grips, then the residual compressive strain and stress can be assumed to be acting over the entire length of the sample.

This residual stress has profound effect on the fatigue behavior of the composite under multiaxial loading as discussed in the next section.

This strain is recovered upon sample fracture, as observed in Figure 4.15.

Finally, such coupling, between applied axial load and induced rotational angle, was also observed. However, the magnitude was not significantly low as observed in Figure 4.15.

4.3.3 Type I Combined Tension/Torsion Test Results

Sample 9 and 11 were loaded proportionally in tension-torsion loading with a tension to torsion ratio of $\alpha = 3$. The stress-strain curves for Sample 9 are plotted in Figure 4.28 with the calculated values of G_{xy} and E_{yy} overlaid.

The difference in strain measured by the ARAMIS system and the strain gage, observed in Figure 4.28, are comparable to that observed in cases of pure tension and torsion loading discussed in Sections 4.3.1 and 4.3.2, and are due to the reasons discussed in those sections.

Failure of Sample 9 was in the grip section close to the chamfered edge of the steel plug. The failure surface showed clean fiber failure near the grip with some delamination as shown in Figure 4.29, suggesting a sudden failure. There were some snapping sounds recorded prior to the large acoustic emission (bang) corresponding to final failure. The permanent lateral contraction was not to the extent observed for pure tension loading; nevertheless, it confirmed the damage in the samples.

Sample 9 experienced a non-linear transition in global axial strain due to damage similar to that experienced by Sample 20, as discussed in Section 4.3.1. The axial modulus of Sample 9 was slightly lower than that of Sample 20. The stress-strain curve was simulated for Sample 9, using incremental analysis discussed in Appendix B, assuming no damage. The results are compared with experimental results in Figure 4.30. The predicted curves compare very well with experimental curves at lower strain values when there is no damage. Substantial deviation occurs at higher strain values, due to damage that accrues in the sample at higher strain values, as shown in Figure 4.30.

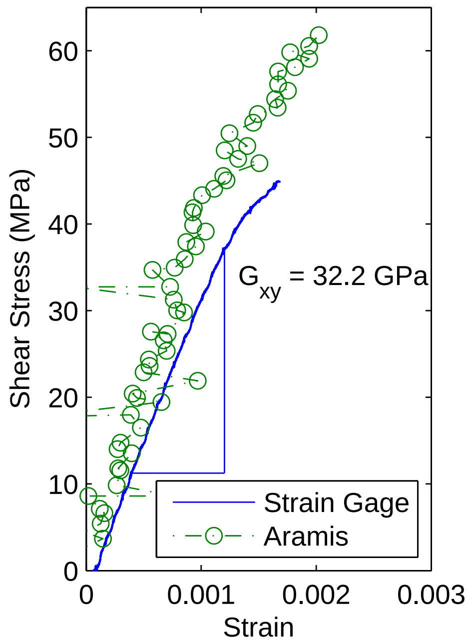

Figure 4.28: Shear and normal stress-strain plots for sample 9 under combined tension-torsion loading

(a) Upper Half

(b) Lower Half

Figure 4.29: Fractured halves of Sample 9 highlighting the fracture modes

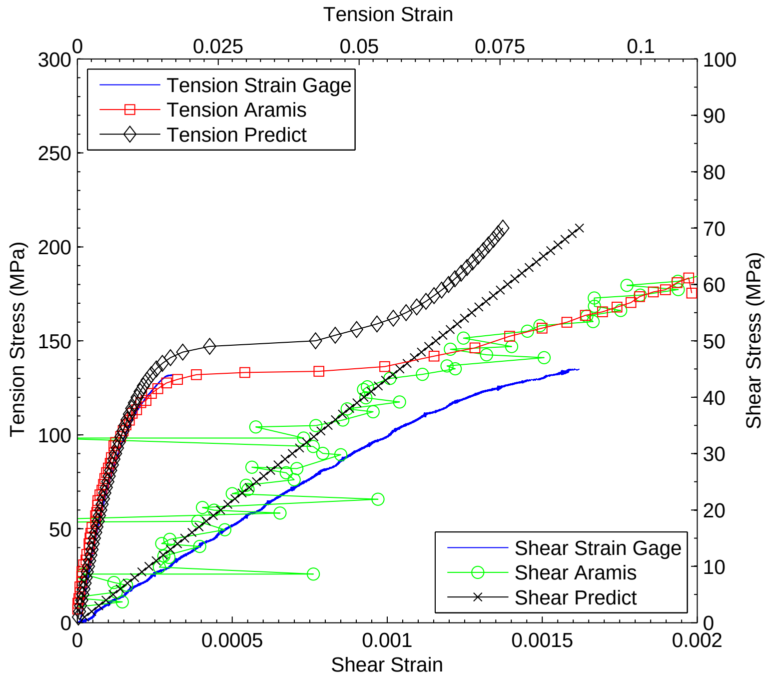

Figure 4.30: Comparison of experimental and predicted stress-strain curves, for Sample 9 subjected to combined tension - torsion quasi-static loading

4.4 Fatigue Test Results

Fatigue test results for various loading types are summarized in Table 4.5. Results for each loading type are discussed before comparing them to evaluate the effect of loading path. To start with, the results for uniaxial loading are discussed before discussing the multiaxial loading. The strain in the sample was recorded during fatigue to evaluate the damage progression. Due to the high frequency of testing (3 Hz), the strain could not be measured using ARAMIS at each distinct load and unload point during a single cycle. The strain gages that were attached to the samples debonded from the high strains involved (>2%). This necessitated the use of the Instron cross-head position to calculate the strains in order that the modulus degradation be tracked during testing. The difference in strains determined using ARAMIS and cross-head position has been discussed in the previous sections. Hence, the trend in the data is emphasized over the absolute values.

Fatigue testing for load path Types I-V has resulted in the S-N curve shown in Figure 4.31. The S-N curve is a tool for comparing varying stress states, denoted by S, to their respective fatigue life in cycles, denoted by N. The value S plotted on the ordinate of the graph is the alternating value of stress in the fatigue loading that is normalized by dividing by the ultimate strength for that loading. The value N plotted on the abscissa of the graph is the number of cycles the sample lasts. The chart plotted in Figure 4.31 shows different trends for each of the loading Types I-V giving an early indication of load path dependence.

The S-N curve shown in Figure 4.31 shows Type I, II, and IV following a similar linear trend, whereas, Type III (Out-of-Phase Torsion-Tension) and Type IV (Uniaxial Torsion) show extremely non-linear trends that depart from that of Type I, II, and V. This is a clear indication of load path dependence and the importance of evaluating the torsional loading and its import within damage mechanics.

Given that the strain gages were prone to failure early in the testing of the tubes,

Sample	Loading Type	Applied σ_{yy} (MPa)	Applied τ_{xy} (MPa)	Cycles	Comments
12	1 (Tension-Torsion)	177	59	400	Failure
13	1 (Tension-Torsion)	142	47	108055	Failure
14	1 (Tension-Torsion)	129	43	394749	Unloaded*
1	1 (Tension-Torsion)	79	27	1450000	Unloaded
21	2 (Tension then Torsion)	179	60	179	Failure
16	2 (Tension then Torsion)	145	48	30307	Failure
17	2 (Tension then Torsion)	127	42	545138	Failure
25	2 (Tension then Torsion)	129	43	1250135	Unloaded
23	3 (Torsion then Tension)	175	58	272	Failure
19	3 (Torsion then Tension)	147	49	5514	Failure
22	3 (Torsion then Tension)	100	33	12267	Failure
18	3 (Torsion then Tension)	130	43	29966	Failure
24	3 (Torsion then Tension)	105	35	46021	Failure
29	4 (Tension)	178	0	334	Failure
30	4 (Tension)	145	0	48256	Failure
27	4 (Tension)	121	0	2400000	Unloaded
28	5 (Torsion)	0	245	78210	Failure
31	5 (Torsion)	0	266	81790	Failure
32	5 (Torsion)	0	285	643155	Failure

*Sample 14 unloaded at 394749 cycles and failed from load spike during restart

Table 4.5: Fatigue Results of all Tube Samples

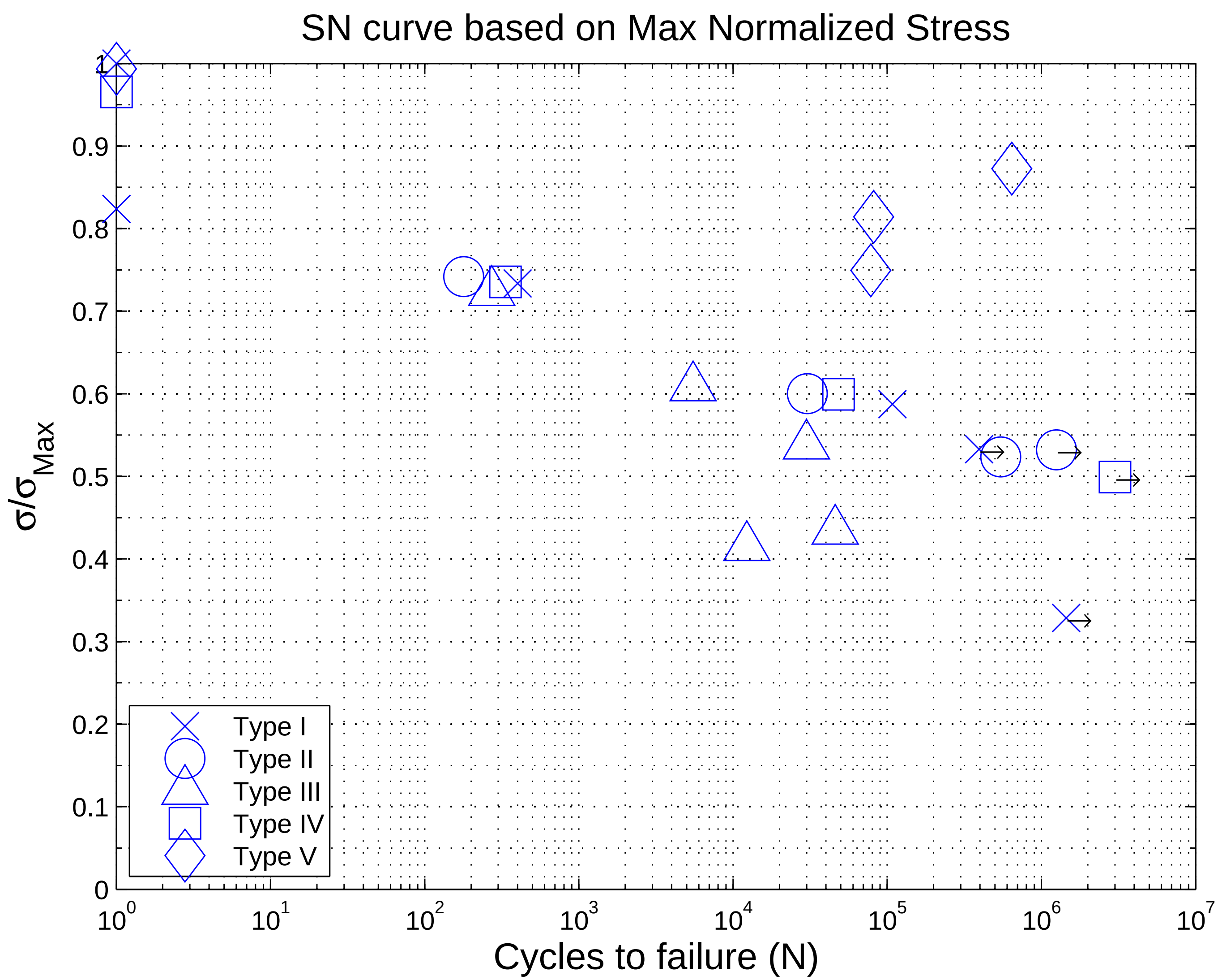

Figure 4.31: S-N curve for Type I, II, III, IV, and V loading

the displacement of the cross-head of the Instron system is used for the calculation of strains. This movement has been shown in Figure 4.7 to correlate well with strain values measured by strain gages. Using those strains, it is possible to track the values of E_{yy} and G_{xy} during the test. The results of this is shown in Figure 4.32 and 4.33. It is noted that G_{xy} is not calculated for Type IV loading and E_{yy} is not calculated for Type V loading, as those loading types did not apply an external force and thus the stress terms cannot be calculated. The values of E_{yy} and G_{xy} are being plotted against cycles to failure in an attempt to visualize damage progression during the test. As the fibers and/or matrix crack, the load distribution in the laminate will change and affect the values of E_{yy} and G_{xy}. It should be noted that stiffness of the load frame itself can affect positional measurements; while this might adjust the actual values of E_{yy} and G_{xy}, it is not the absolute value of E_{yy} and G_{xy} that is needed; rather it is the relative change in E_{yy} and G_{xy} over time that is of interest.

Arranging all of the samples tested in fatigue in order of loading type and load level (see Figure 4.34), allows the fracture pattern to emerge. In the photo, the first three columns are samples tested in biaxial fatigue and the samples across each row are tested at the same load level. The last two columns are the samples tested in uniaxial fatigue. Within each column the sample at the front is the lowest load level and the sample at the back is the highest load level.

Within the biaxial fatigue samples it is seen that samples tested fail by a combination of fiber failure, delamination, and matrix cracking as can be seen in Figure 4.35 for examples of each. Starting with Type I, the samples fail by a combination of fiber failure and delamination. As the load increases the amount of delamination increases. Then, when moving to Type II and III loading, the delamination increase starts at a lower load threshold; moving higher in loading results in matrix cracking without delamination occurring.

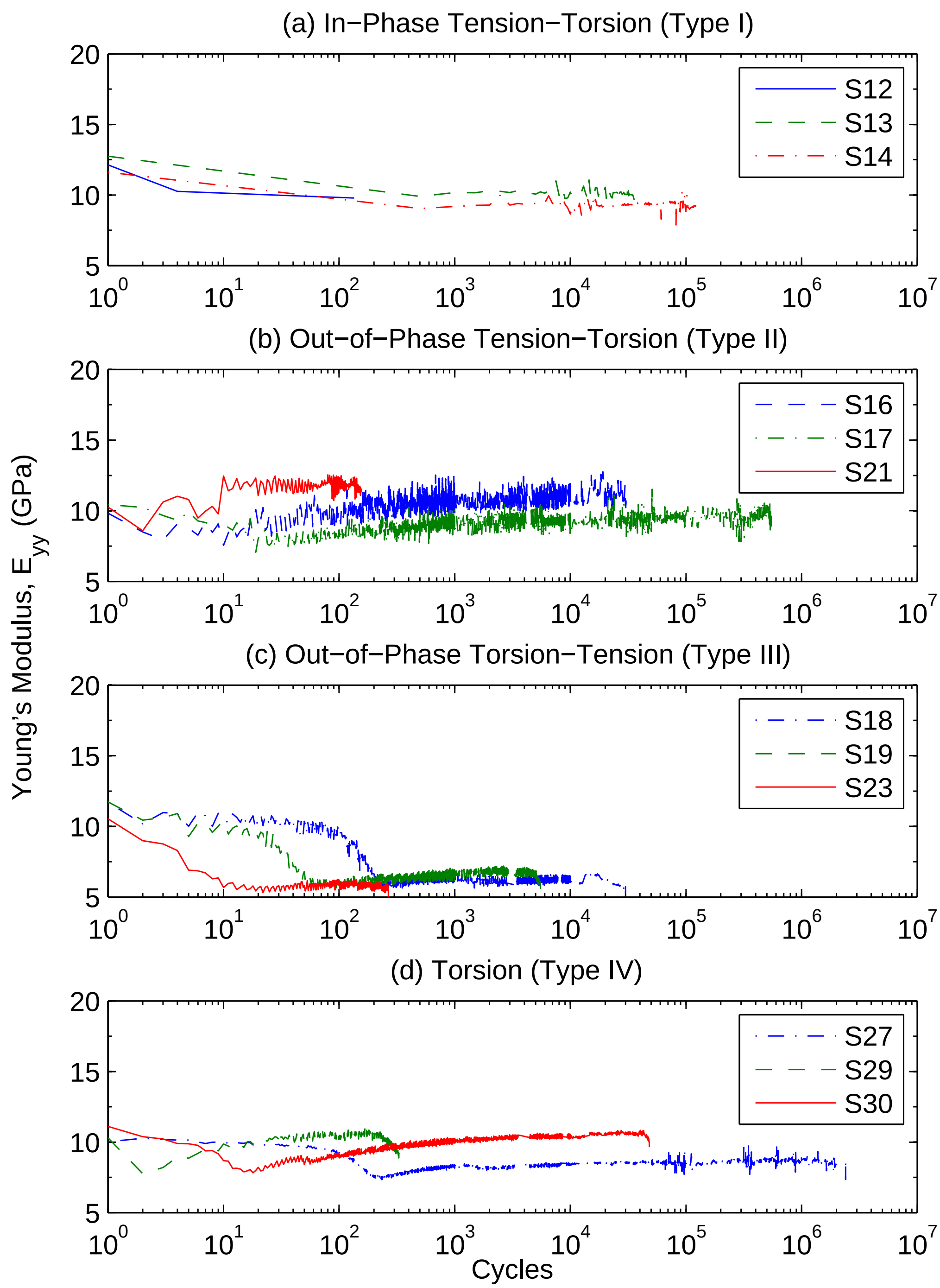

Figure 4.32: Variation of Young's Modulus, E_{yy}, during fatigue testing

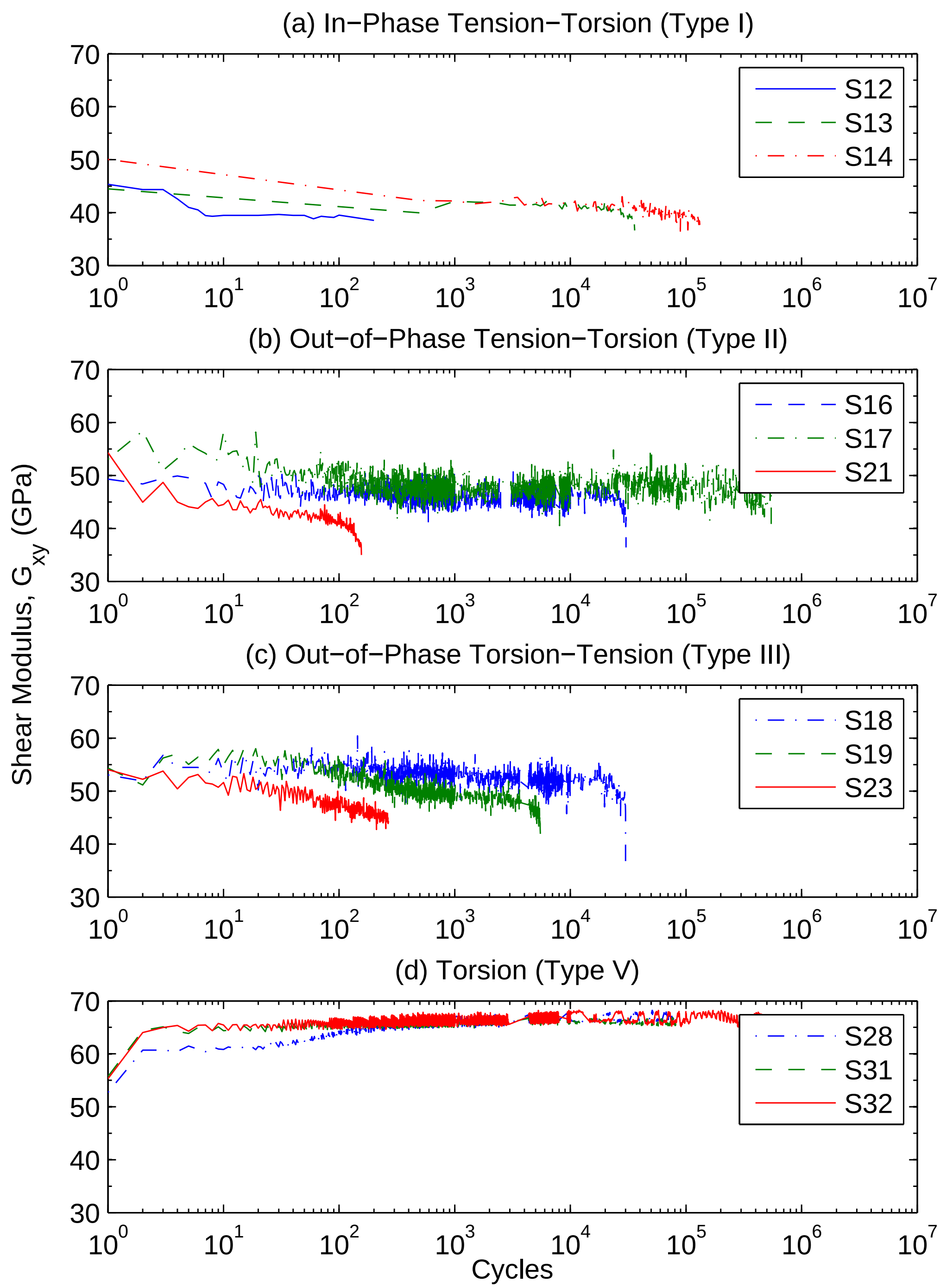

Figure 4.33: Variation of shear modulus, G_{xy}, during fatigue testing

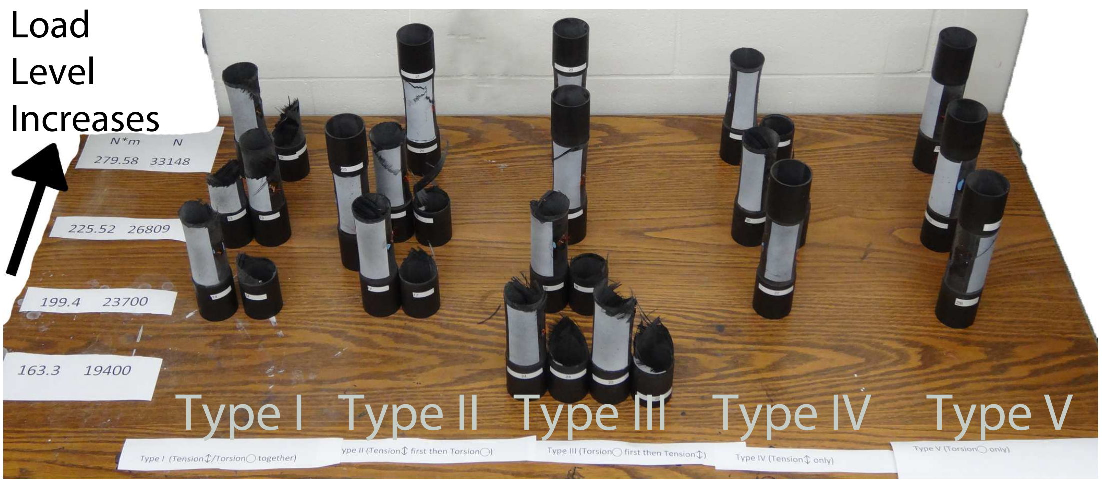

Figure 4.34: Fatigue sample failures grouped by loading type

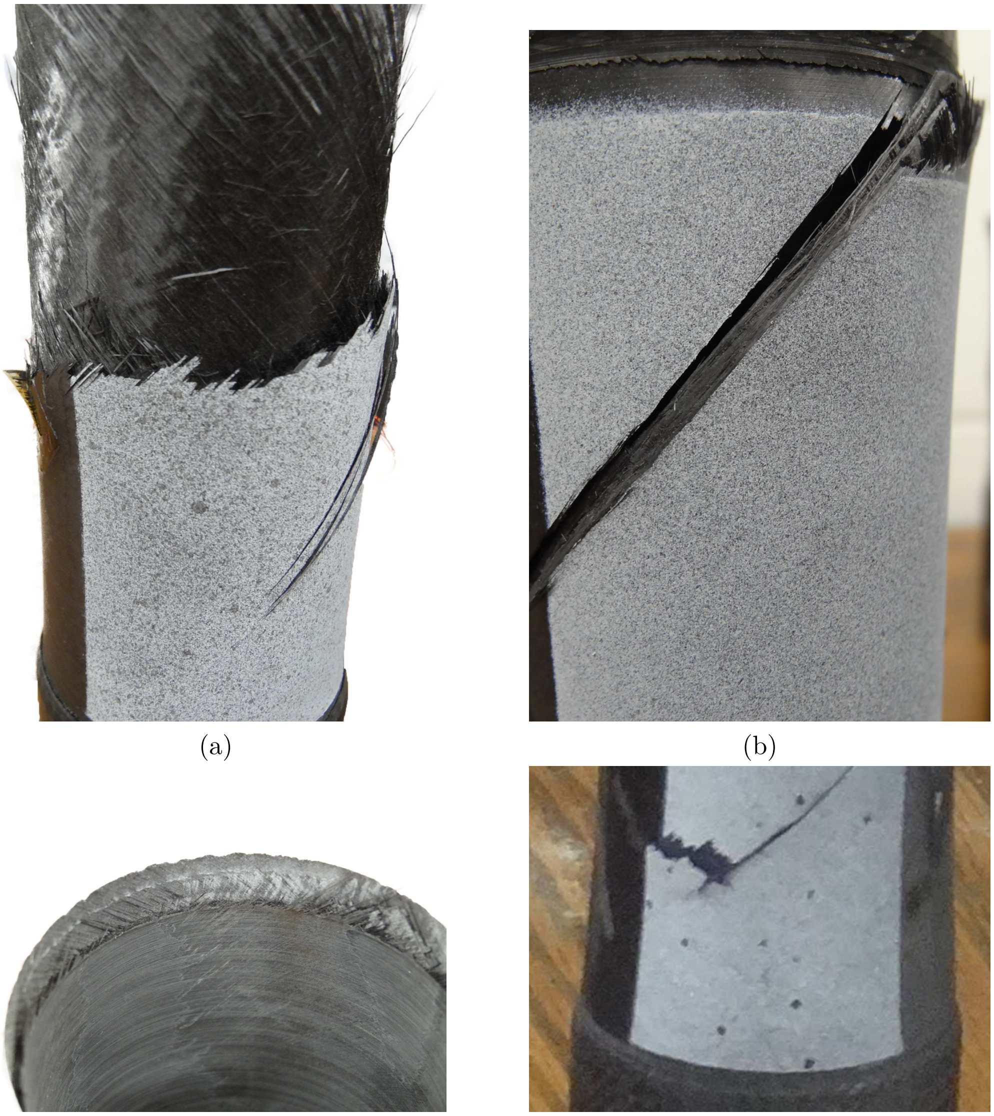

(a) (b) (c) (d)

Figure 4.35: Examples of failure modes: (a) Tube with partial delamination of top layers; (b) Tube failure under shear load; (c) Brittle failure at the gripped end caused by fiber failure under tension; and, (d) Transverse failure

4.5 Uniaxial Fatigue Data

The results of the uniaxial fatigue tests, Types IV and V, described in Section 3.3.3, are presented in more detail below in Section 4.5.1 and 4.5.2.

4.5.1 Type IV - Uniaxial Tension Fatigue Loading

The load levels at which the samples were tested are tabulated in Table 4.5 and can be visually seen in Figure 4.36. The cycles to failure are plotted in Figure 4.31 as a function of stress amplitude normalized to the ultimate tensile strength. The cycles to failure increased with decrease in stress, as expected. Sample 27, with a

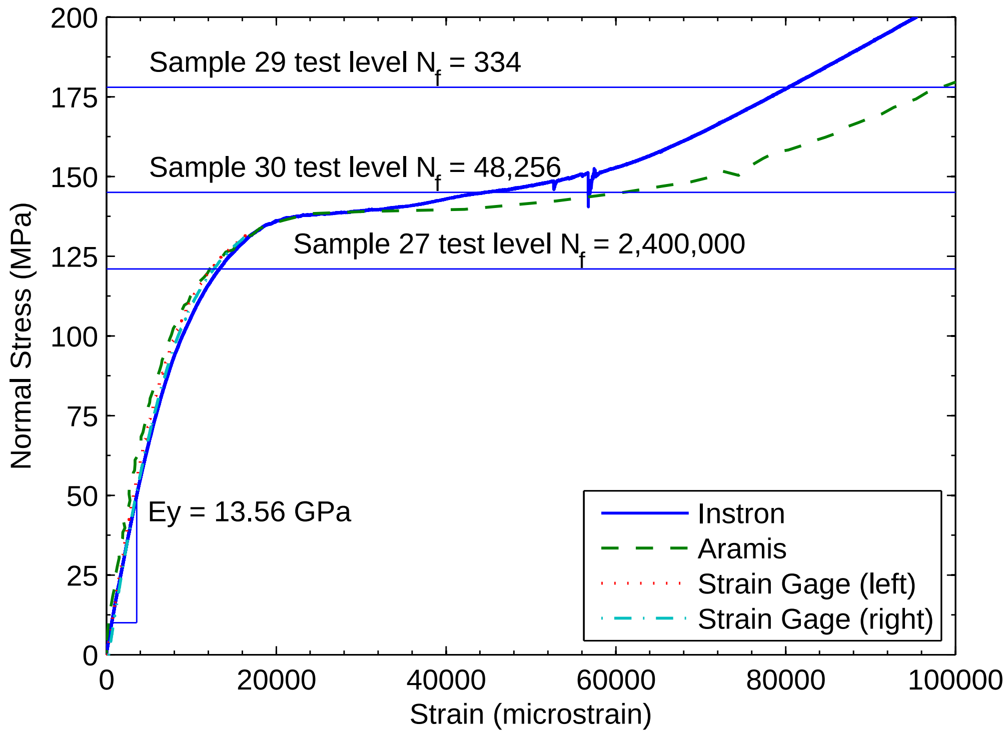

Figure 4.36: Type IV test levels overlaid on Sample 20 stress vs. strain graph

stress amplitude of 121 MPa just below the linear to non-linear transition in the stress-strain curve, did not fail even after 2.4 million cycles. However, the permanent axial strain increased with the number of cycles as shown in Figure 4.37. It should be noted that the permanent strain during the first cycle was negligible, suggesting that the increase in permanent strain was due to increase in damage with fatigue. In order to confirm this further, the change in the modulus of the specimen during fatigue was determined and is plotted in Figure 4.32. The degradation in the axial modulus of the composite started below 100 cycles; however, substantial degradation occurred between 100 and 1000 cycles, confirming the sudden jump in strain observed in Figure 4.37. Although the permanent strain continued to increase beyond 1000 cycles, the modulus increased marginally and remained constant for the rest of the fatigue cycles. With increase in the fatigue load, substantial degradation occurred at lower cycles; it can be inferred from Figure 4.32 that occurred between 10 and 100 cycles at 145 MPa (Sample 30) and between 1 and 10 cycles at 178 MPa (Sample 29). This is confirmed by a sudden jump in the permanent strain in Figures 4.38 and 4.39. Although the increase in the permanent strain during this sudden jump increased with increase in the fatigue load, the magnitude of degradation in axial modulus did not change with the fatigue load. These strain values correspond to the plateau region in the stress-strain curve in Figure 4.36.

Similar to Sample 27, the axial modulus increased after the sudden degradation for Samples 30 and 29; however, the rate of increase increased with fatigue load. The values at failure were equal to the starting value (i.e. first cycle). The strains at failure for samples 30 and 29 correspond to the region of the stress-strain curve where strain hardening is observed. Hence, the observed increase in the axial modulus during fatigue is due to the same reasoning given for strain hardening observed during quasi-static testing; i.e., rotation of the fiber orientation towards the loading axis, enabled by the matrix cracking in the plies.

During this test, the rotary actuator was commanded to maintain zero torque while the axial load was cycled. Therefore, zero shear load and stress are observed in Figures 4.37-4.39. However, a gradual increase in shear strain, with increase in fatigue

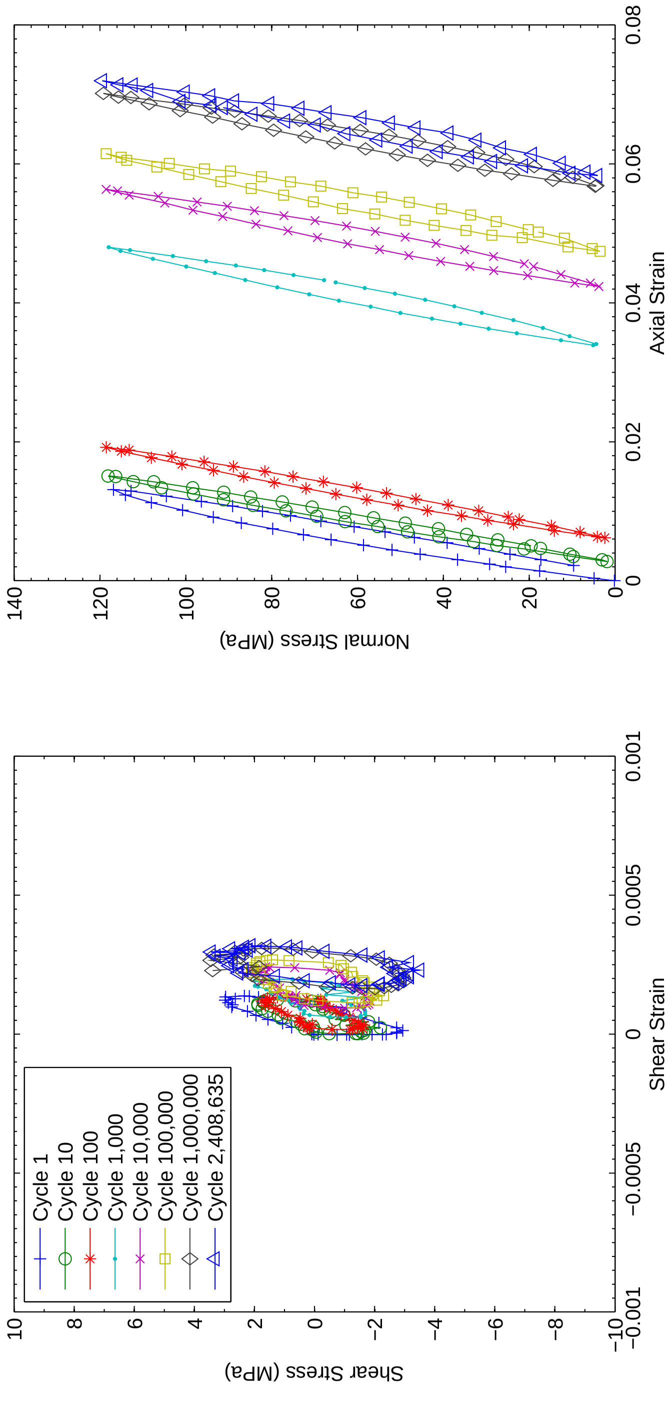

Figure 4.37: Sample 27 (Type IV [50% of σ_{yy}^{max}]) hysteresis

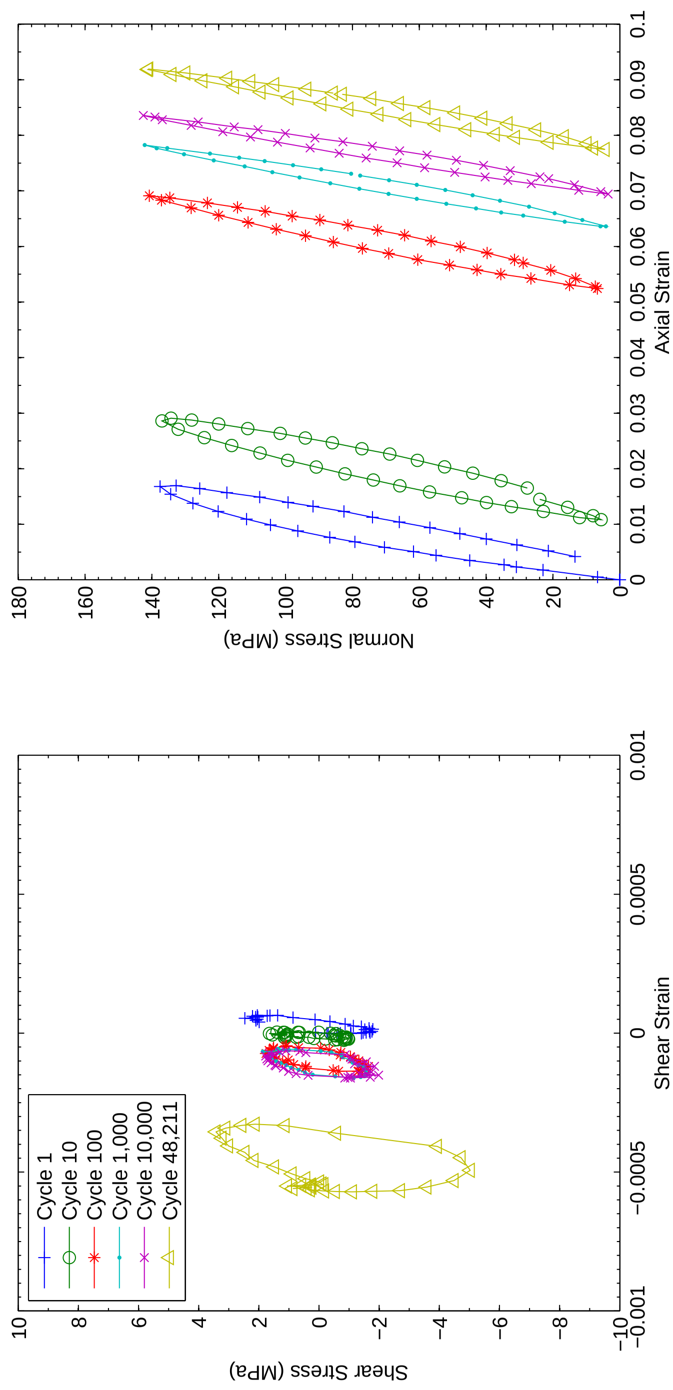

Figure 4.38: Sample 30 (Type IV [60% of σ_{yy}^{max}]) hysteresis

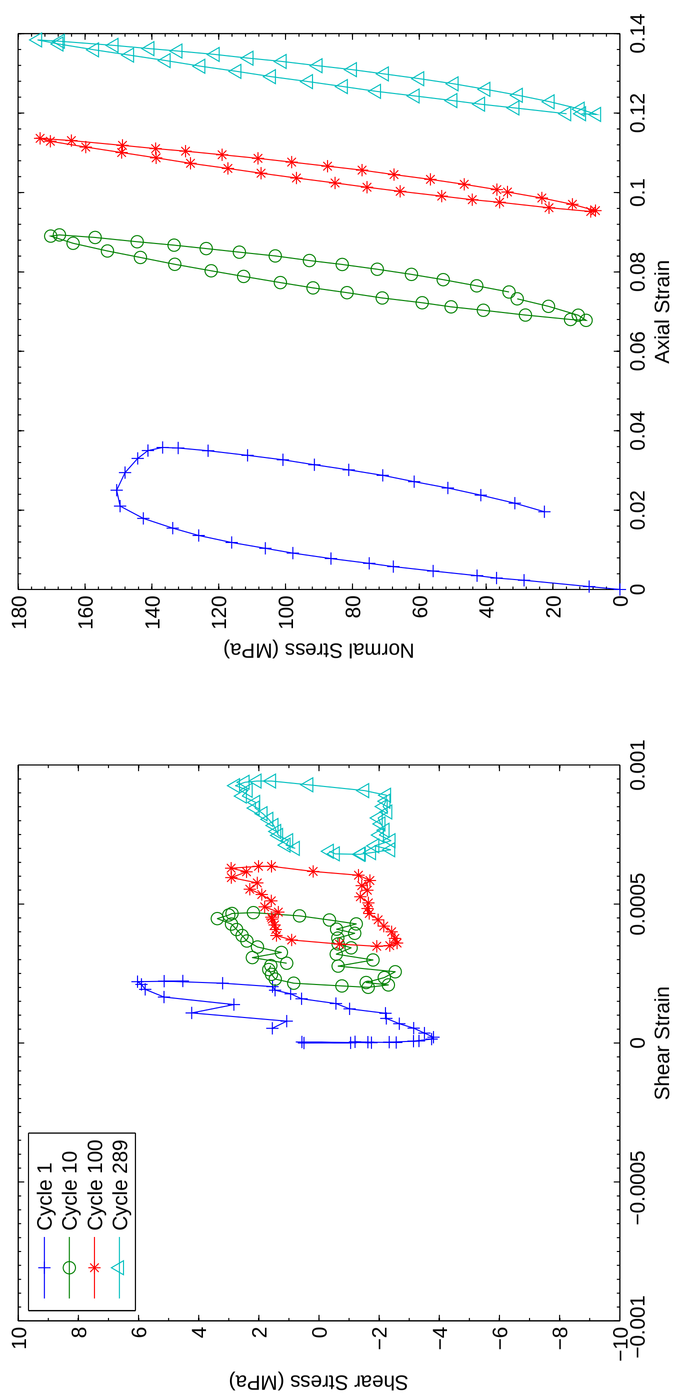

Figure 4.39: Sample 29 (Type IV [75% of σ_{yy}^{max}]) hysteresis

cycles, was observed. This is a sign of gradual loss in the balanced layup configuration of the composite; that is, the shear - normal coupling coefficient became non-zero due to cracking resulting in shear strain due to applied axial stress. The level of this material coupling, as indicated by the magnitude of shear strain in Figure 4.37-4.39, increased with increase in the fatigue load due to increase in the extent of damage. The shear strain in Sample 30 in Figure 4.38 is opposite in sign to the shear strain in Sample 29 in Figure 4.39. This is believed to be due to difference in the type of plies in which the maximum damage is occurring. For example, it could be [+45] plies in Sample 30 and [−45] plies in Sample 29.

An image of the failed / unloaded samples is given in Figure 4.40. Both Samples

Figure 4.40: Samples failed under tensile fatigue (Type IV loading)

29 and 30 failed near the grip, as shown in Figure 4.35c, due to stress concentration discussed in previous sections. The extent of apparent necking increased with increase in the fatigue load, confirming the observation made earlier about the increase in the extent of damage with increase in the fatigue load. This is believed to have resulted in higher strain to failure in Sample 29 when compared to Sample 30. The final failure mode is the same as that observed during quasi-static tensile testing; limited delamination (see Sample 30 in Figure 4.40) followed by fiber failure near the gripped

end. This was preceded by matrix cracking during fatigue cycles.

4.5.2 Type V - Uniaxial Torsion Fatigue Loading

The load levels at which the samples were tested are tabulated in Table 4.5 and can be visually seen in Figure 4.41. The magnitude of applied shear stresses were within 20% of the ultimate strength. The cycles to failure are plotted in Figure 4.31. Unlike the tension loading, wherein a monotonic decrease in fatigue stress amplitude with increase in fatigue cycles to failure was noticed, torsional loading resulted in samples loaded to higher stress amplitude lasting longer than those loaded to lower stress amplitudes.

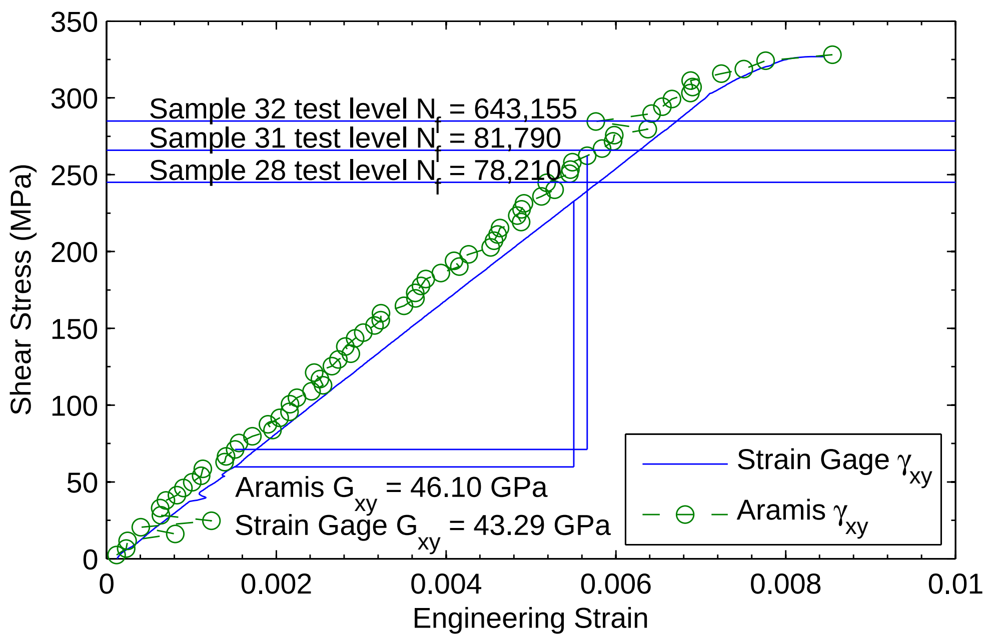

Figure 4.41: Type V test levels overlaid on Sample 7 stress vs. strain graph

A permanent strain of 0.001 was recorded after the first cycle for all specimens as shown in Figures 4.43-4.45, which increased gradually during subsequent cycles. Associated with this permanent strain was the sudden increase in the shear modulus, observed in Figure 4.33 after the first cycle. Since the fiber orientation in the composite [±45] resulted in maximum shear modulus, any rotation of fibers due to matrix cracking would likely to result in the reduction of shear modulus.

While the cause for this is not understood, one possible contributor is the matrix cracking. The permanent shear strain is believed to be due to matrix cracks forming parallel to fibers in both [+45] and [-45] layers. This, as well as coupling between linear actuator position and rotary actuation (discussed in Section 4.3.2), resulted in compressive axial strain observed in Figures 4.43-4.45. This reduction in the length of the sample would have caused a reduction in the angle of twist for a given torque since

$$\phi = \frac{TL}{JG}, \tag{4.8}$$

where T is the torque, L is the sample length, J is the polar moment of inertia, and G is the shear modulus. The measured angle of twist was used to determine the maximum shear strain

$$\epsilon_{\max} = \frac{c\phi}{L_0}, \tag{4.9}$$

which in turn was used to calculate the shear modulus. Since the original length was used, the maximum strain would have decreased with decrease in the measured ϕ, caused by the reduction in the length of the sample. This reduction in angle of twist can be seen in Figure 4.42.

Nevertheless, the axial strain of 0.0025 in Figures 4.43 - 4.45 is unlikely to have resulted in the level of increase in shear modulus observed in Figure 4.33. Another possible contributor is loss of balanced layup configuration due to cracking (i.e., the shear-normal coefficient becoming non-zero). Further investigation of this is necessary.

The odd trend observed in Figure 4.31 is also believed to be due to above-mentioned causes.

Figure 4.46 shows the failed samples. A close-up of failure is shown in Figure 4.47. Matrix cracks that develop in [+45] and [-45] plies are perpendicular to one another. The fibers in one of the plies must fracture in order for the sample to fail. For example, the matrix cracks in [+45] plies is seen in Figure 4.47. The fibers in [-45] plies below the matrix cracks in [+45] plies must fracture for the crack to pass through the entire thickness, resulting in the ultimate failure of the composite specimen. A similar failure mode was observed during quasi-static torsional testing.

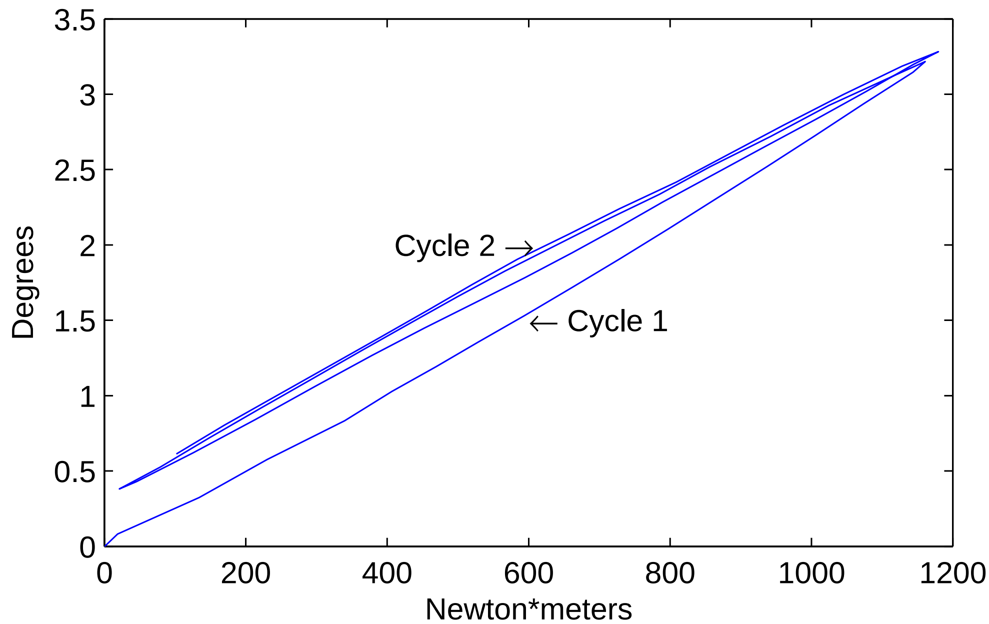

Figure 4.42: Sample 28 position plotted as a function of load applied during the first two loading cycles

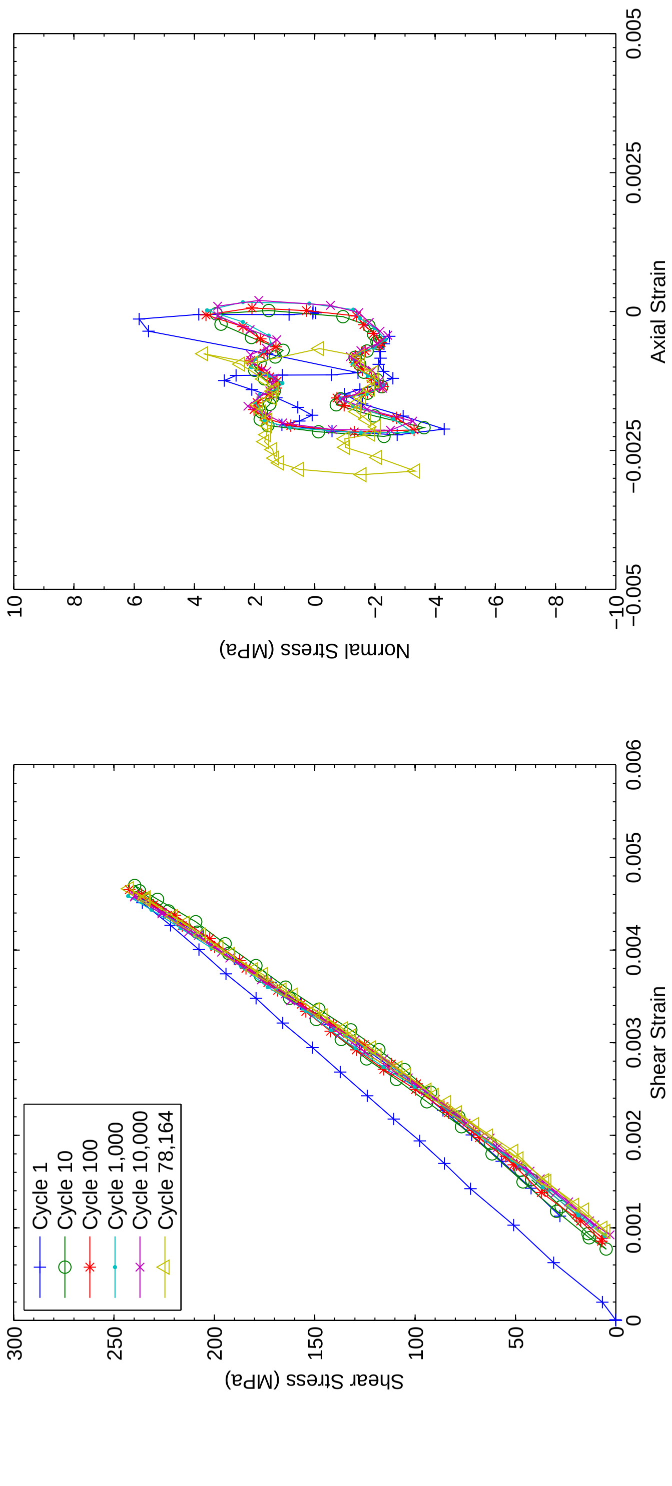

Figure 4.43: Sample 28 (Type V [75% of τ_{xy}^{max}]) hysteresis

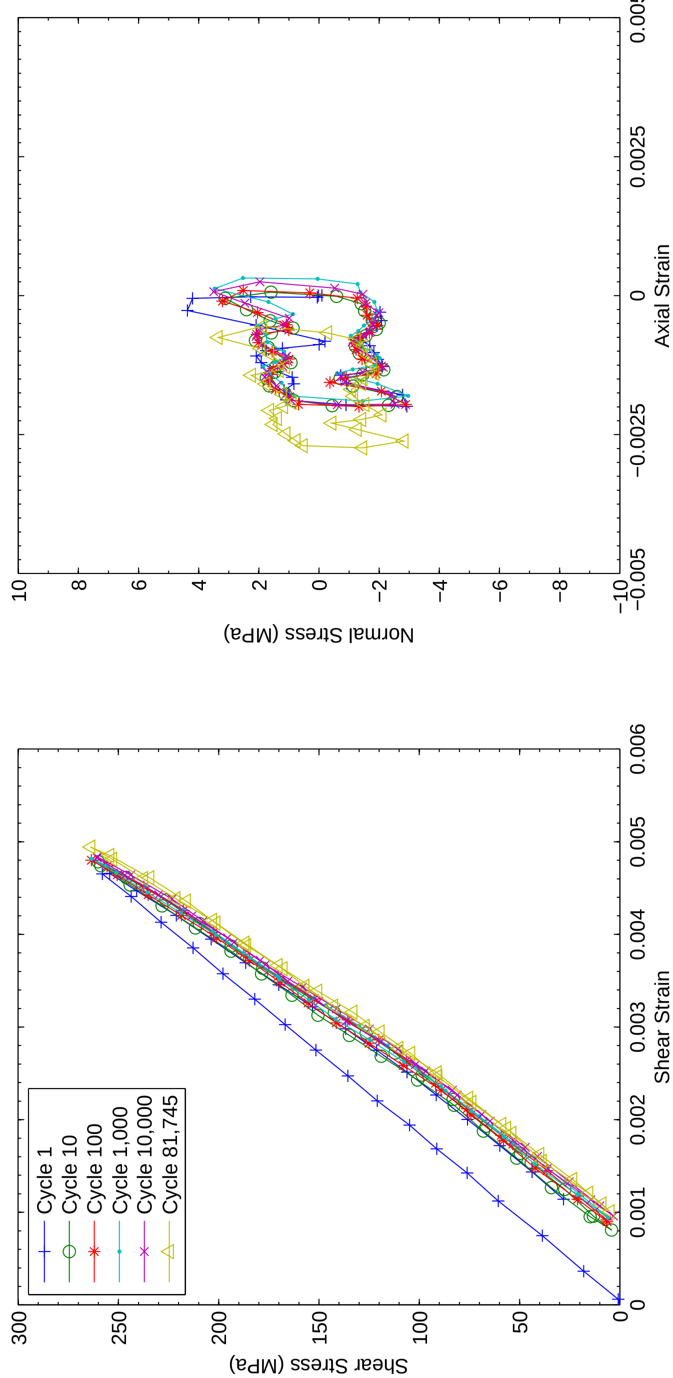

Figure 4.44: Sample 31 (Type V [80% of τ_{xy}^{max}]) hysteresis

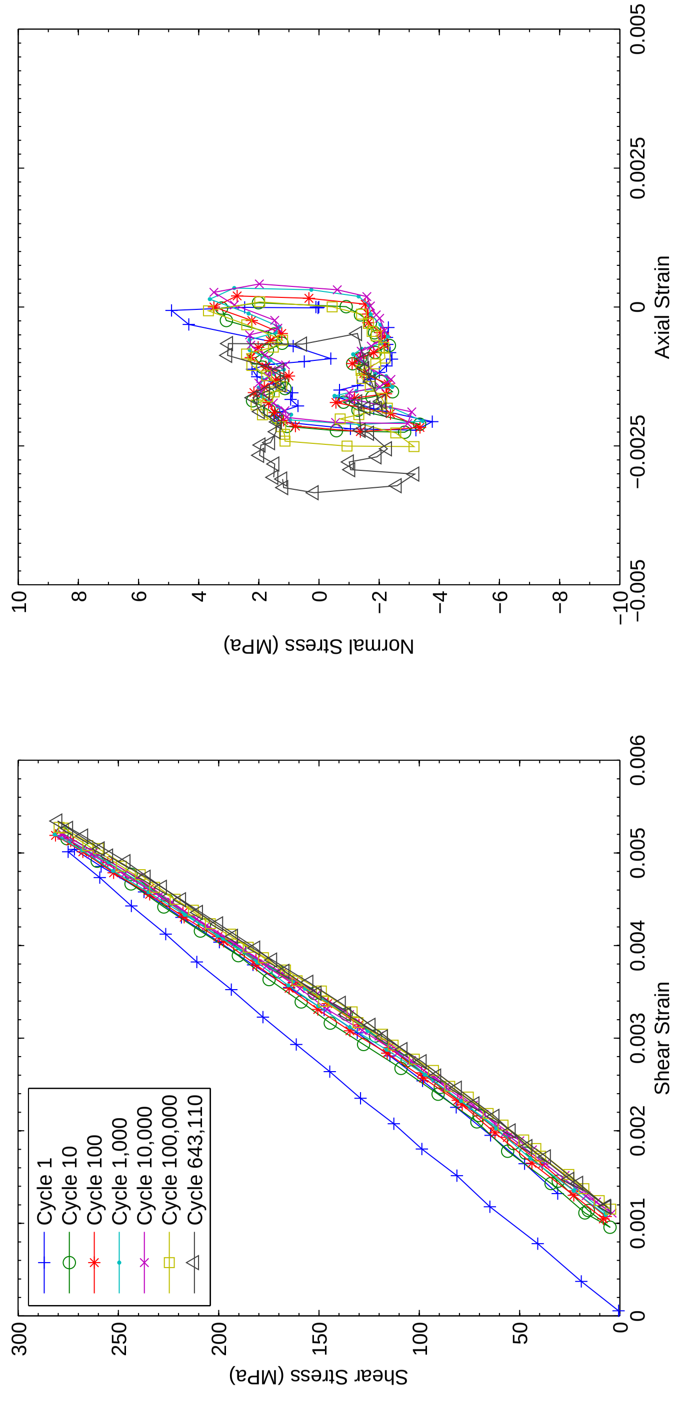

Figure 4.45: Sample 32 (Type V [90% of τ_{xy}^{max}]) hysteresis

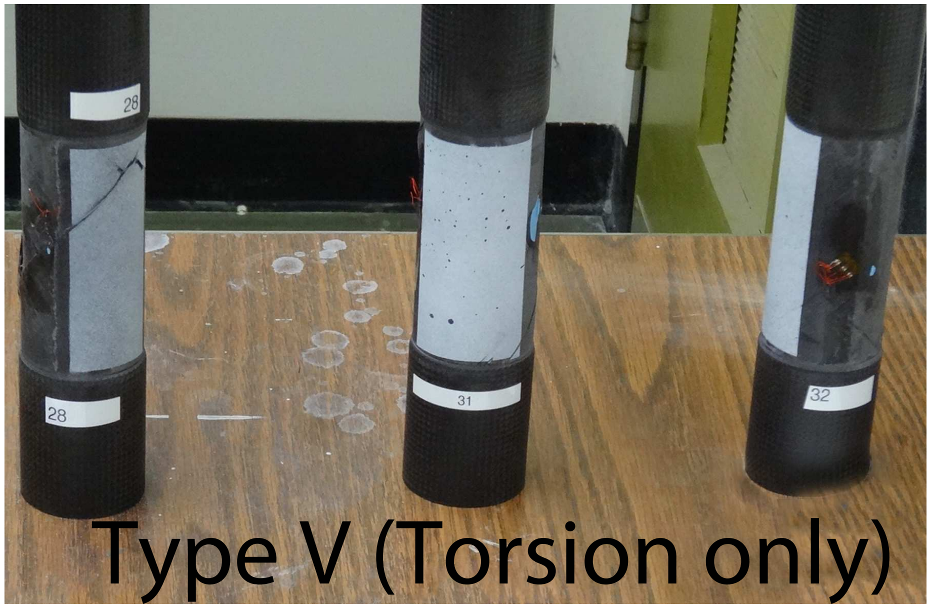

Figure 4.46: Samples failed under torsional fatigue (Type V Loading)

Figure 4.47: Tube failure under shear load

4.6 Biaxial Fatigue Data

The three loading types I, II, and III, described in Section 3.3.3, are presented in Sections 4.6.1-4.6.3.

4.6.1 Type I - Biaxial Tension-Torsion Fatigue Loading

The load levels at which the samples were tested are tabulated in Table 4.5. While Sample 1 was unloaded after 1.45 million cycles, Sample 14 had to be unloaded after 394,749 cycles due to power failure. During the unloading of Sample 14 the load frame restarted at a higher load value than what was used for the first 394,749 cycles and rapid failure of the sample occurred. Hence, Sample 14 was recorded as unloaded at 394,749 cycles. The cycles to failure are tabulated in Table 4.5 and plotted in Figure 4.31. The maximum axial stress amplitudes used in this loading are the same as those used in Type IV (tension) loading. However, the maximum shear stress amplitudes are less than those used in Type V (Torsion) loading; a ratio of 3:1 was maintained between the maximum tensile and shear stress amplitudes.

While the samples loaded in the linear region (Sample 1) or in the linear-non-linear transition region did not fail in reasonable time, the samples loaded in the non-linear region (Samples 12 and 13) failed quickly. It should be noted that the damage started at stresses in the linear to non-linear transition region and progressed rapidly. While a similar trend was observed in tension only loading case, the cycles to failure for a given stress amplitude, under in-phase tension - torsion loading was more than the cycles to failure under tension loading only.

While the permanent axial strain increased with fatigue cycles and stress amplitude as shown in Figures 4.48 - 4.50, its magnitude before failure, at a tensile stress amplitude, was lower than that observed for the case of tension loading in Figures 4.37 - 4.39. In addition, the samples subjected to this loading also exhibited permanent shear strain that increased with shear stress amplitude, similar to the case of tension loading only. These suggest increasing damage with fatigue and stress amplitude. Due to this damage, both the axial and the shear moduli decreased with increase in the number of fatigue cycles, as observed in Figures 4.32 and 4.33. This is in contrast to the pure tension case, wherein the axial modulus decreased during the initial 1000 cycles and increased subsequently, and to the pure torsion case, wherein the shear modulus increased to a plateau value.

In contrast to pure tension loading, the samples that failed under in-phase tension-torsion exhibited extensive delamination, as shown in Figure 4.51. While fiber failure in all layers were observed in pure tension loading (Figure 4.40), the fiber failure was observed in only few layers. For example, in Sample 13 shown in Figure 4.51, the fibers in the top [+45] layer failed; the exposed [-45] layers at the top of the sample suggests that delamination between the top [+45] and bottom [-45] layers preceded before the final failure of sample through fiber failure in [+45] layers. Transverse cracking that would have preceded the delamination is also observed in the top [+45] layer. The increased level of delamination is believed to be the reason for lower strain to failure observed in Figure 4.49 when compared to pure tension loading case. The increase in the amount of delamination is also believed to be the reason for the monotonic decrease in the axial and shear moduli with increase in the number of fatigue cycles. Comparing Figures 4.51 and 4.40, it can be observed that the amount of pseudo necking, at stress amplitude, is less for tension-torsion loading than for pure tension alone. This is consistent with increased delamination observed in the former when compared to the latter.

Therefore, it can be concluded that the addition of torsional loading in-phase with the tension loading increased fatigue life through reduction in transverse cracking due to increased delamination.

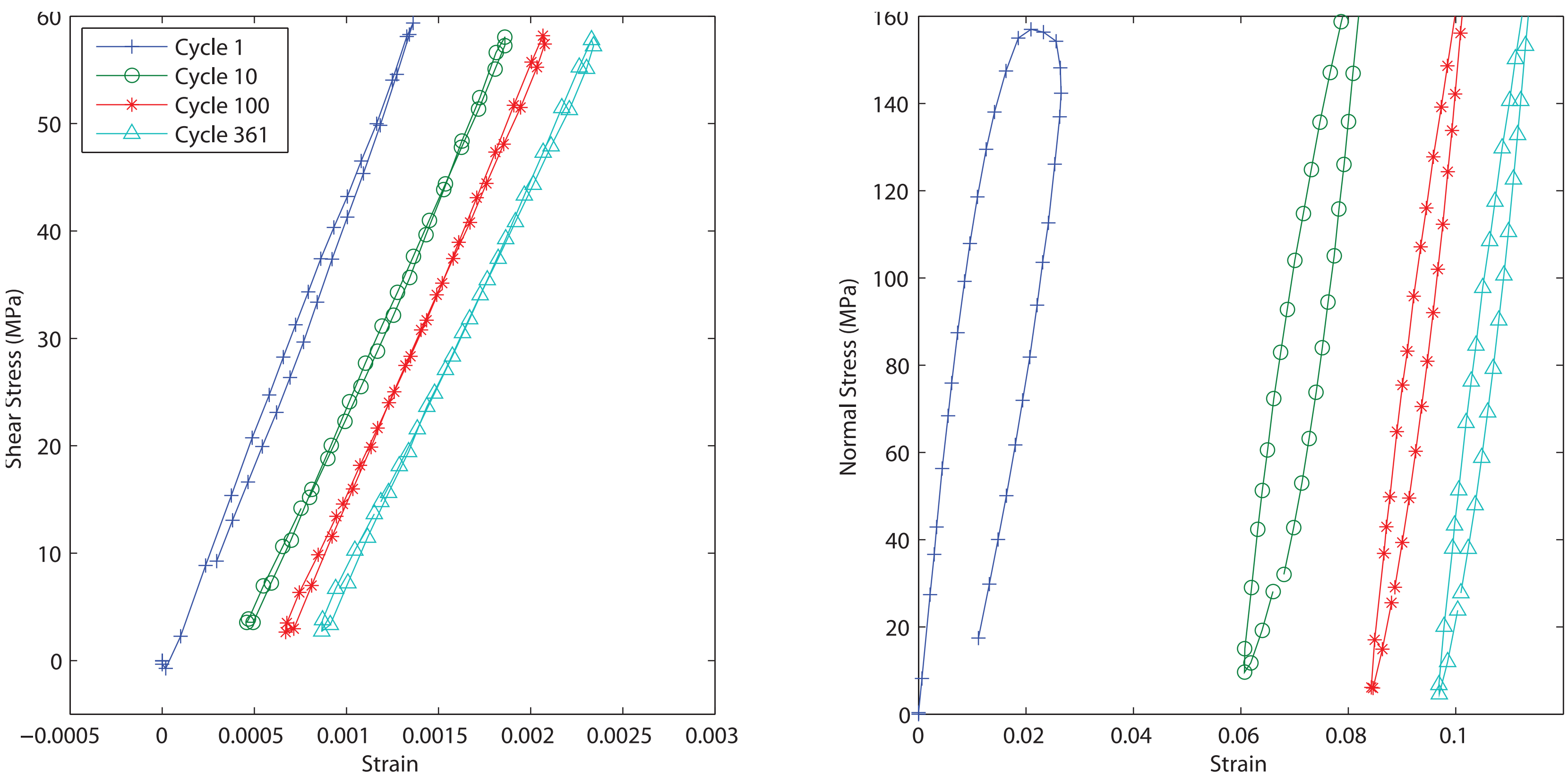

Figure 4.48: Sample 12 (Type I [75% of σ_{yy}^{max} and τ_{xy}^{max}]) hysteresis

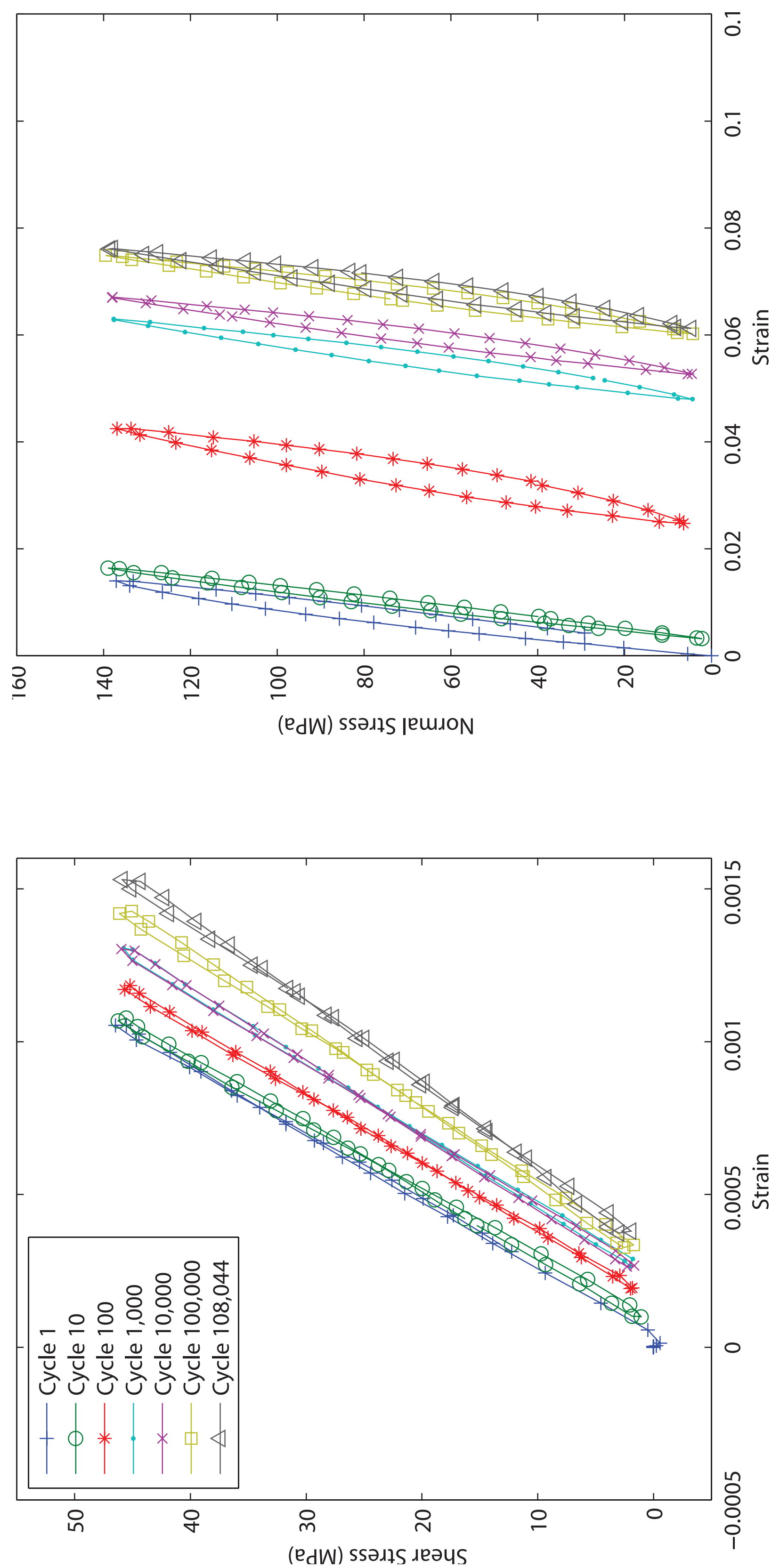

Figure 4.49: Sample 13 (Type I [60% of σ_{yy}^{max} and τ_{xy}^{max}]) hysteresis

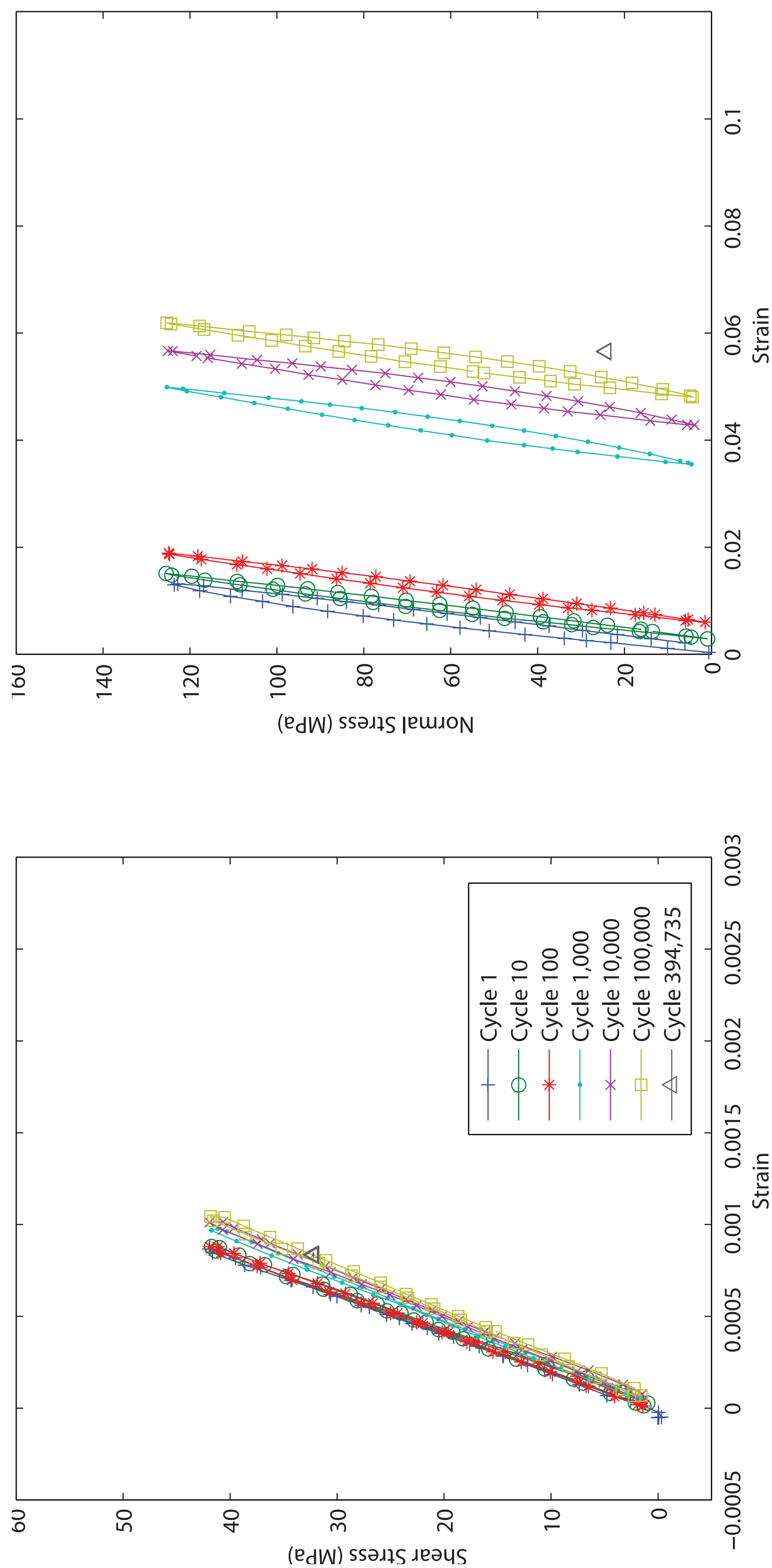

Figure 4.50: Sample 14 (Type I [50% of σ_{yy}^{max} and τ_{xy}^{max}]) hysteresis

Figure 4.51: Samples failed after in-phase tension-torsion fatigue (Type I loading)

4.6.2 Type II - Biaxial Out-of-Phase Tension-Torsion Fatigue Loading

The loads levels at which the samples were tested are tabulated in Table 4.5. Sample 25 was unloaded after 1.25 million cycles. The cycles to failure are tabulated in Table 4.5 and plotted in Figure 4.31. Despite the slightly smaller values for axial and shear stress amplitudes, Sample 17 fractured in much less cycles than Sample 25. Both samples were loaded to stress levels in the linear to non-linear transition zone. For load levels in the non-linear region in Figure 16, the cycles to failure was lower than that for tension only loading and hence, much lower than that for the Type II in-plane tension-torsion loading.

The magnitude of permanent axial strain was more than that recorded for the in-phase tension-torsion loading, as observed in Figures 4.52 – 4.54. However, it was either equal or greater than that recorded for tensile loading only. The magnitude of permanent shear strain was comparable or less that recorded for in-plane tension-torsion testing. During this testing, the axial stress was first applied and the torsion stress was applied subsequently while maintaining the axial stress constant. It was noticed in Section 4.5.2 that the axial compressive strain of the order of 0.0025 was introduced, due to rotary actuation, for shear stresses in the range of 245–285 MPa. Since the shear stress used in this loading mode was $^1/_6$th of the shear stress used in Type V loading, the induced axial strain would have been lower too and for this reason, not visible in Figure 4.55. Similarly, it was noticed in Type IV loading that the applied axial tensile load resulted in shear strain. The maximum permanent shear strain observed in this testing is comparable to that recorded during tension testing alone, as seen in Figure 4.37.

The change in axial and shear moduli is plotted as a function of fatigue cycles in Figures 4.32 and 4.33.

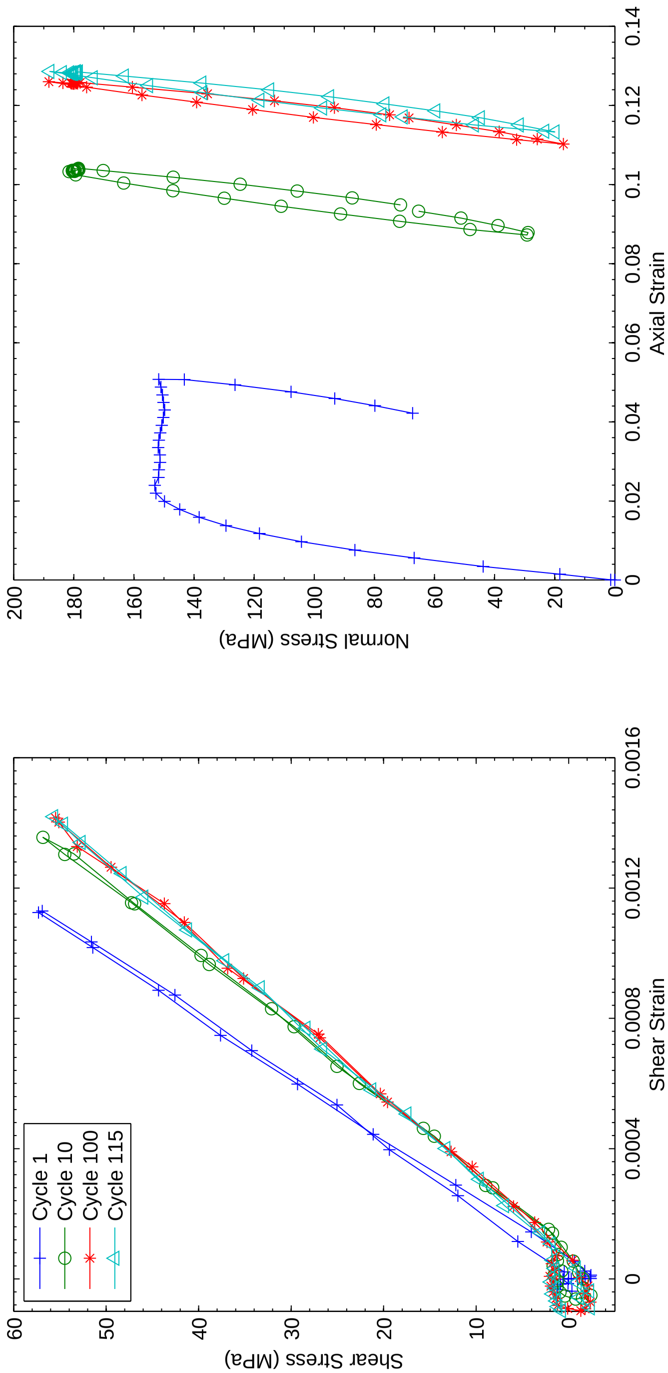

Figure 4.52: Sample 21 (Type II [75% of σ_{yy}^{max} then 75% of τ_{xy}^{max}]) hysteresis

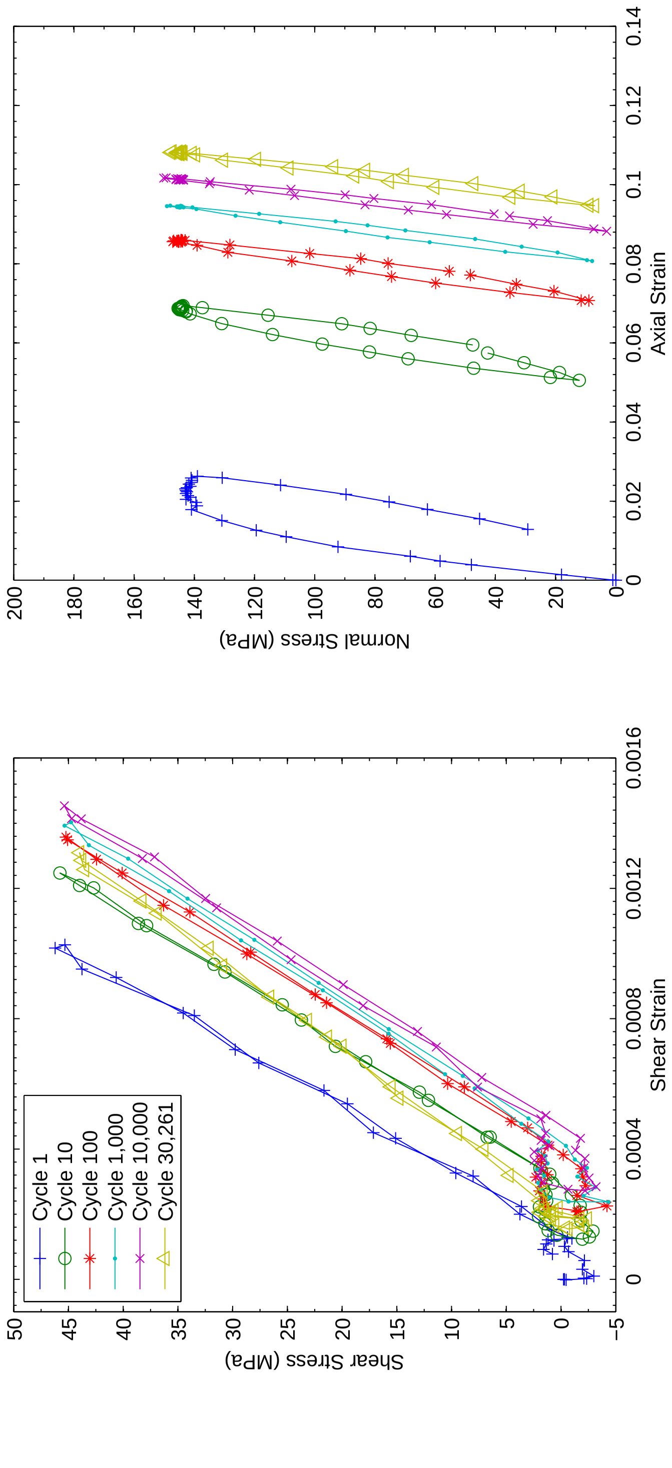

Figure 4.53: Sample 16 (Type II [60% of σ_{yy}^{max} then 60% of τ_{xy}^{max}]) hysteresis

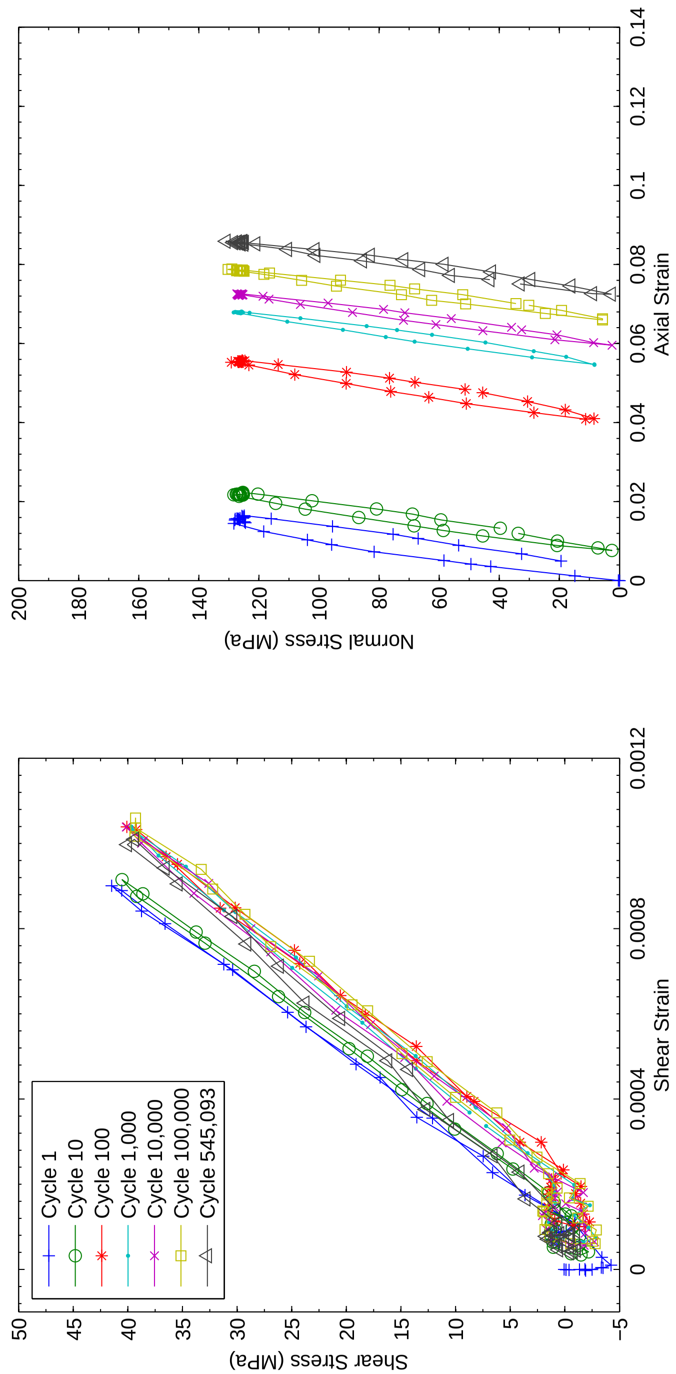

Figure 4.54: Sample 17 (Type II [50% of σ_{yy}^{max} then 50% of τ_{xy}^{max}]) hysteresis

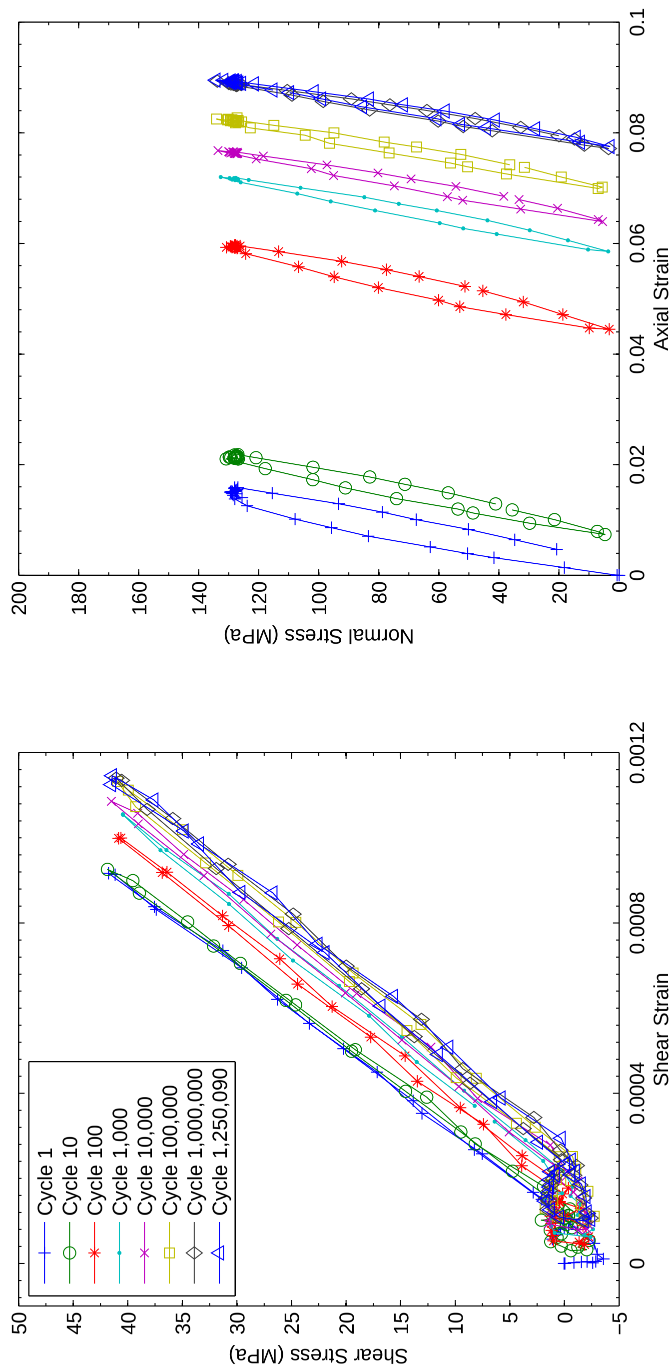

Figure 4.55: Sample 25 (Type II [50% of σ_{yy}^{max} then 50% of τ_{xy}^{max}]) hysteresis

The axial modulus exhibited a trend similar to that observed for tension loading only; evidenced by its decreasing during the first 1000 cycles and then increasing thereafter. The shear modulus decreased similar to that observed for in-phase tension-torsion testing. Unfortunately, shear modulus could not be measured during Type IV - tension testing. Had it been measured, it is believed it would have exhibited a behavior similar to that observed in out-of-phase tension-torsion loading.

The image of failed samples is provided in Figure 4.56. The fracture pattern in Samples 17 and 16 were similar to that observed in case of tensile loading only, given in Figure 4.40. Although the outer ply was [+45], the crack plane observed in Sample 21 was perpendicular to the orientation of the fibers in [+45] and irregular. This indicates that the fibers in [+45] plies of Sample 21 failed. The beginning of this fiber failure process is observed in Sample 16. While the final failure occurred by failure of fibers in all layers, it occurred closer to the grip in Samples 16 and 17. This failure mode is different from that observed for in-phase tension-torsion loading, in Figure 4.51, with fiber failure in some plies accompanied by delamination between plies.

Figure 4.56: Samples failed under out-of-phase tension-torsion fatigue (Type II loading)

Hence, it can be concluded that the transverse cracking influenced the fatigue life for this loading condition, similar to that observed for tension only loading. The fatigue life was lower than that observed for tension only, suggesting that the added out-of-phase torsion reduced the fatigue life.

The observed difference in fatigue life for in-phase and out-of-phase tension-torsion loading is indicative of the effect of load path on fatigue. Since machine coupling (between linear strain and rotary actuation and vice versa) was observed in both loadings, the observed difference is believed to be due to the effect of load path.

4.6.3 Type III - Biaxial Out-of-Phase Torsion-Tension Fatigue Loading

The load levels at which the samples were tested are tabulated in Table 4.5. Unlike other loading, the samples tested at low load levels in the linear region also failed quickly. The cycles to failure are tabulated in Table 4.5 and plotted in Figure 4.31. The cycles to failure are much lower than those recorded for other loading types.

The axial permanent strain was recorded at all load levels and it increased with increase in stress and the number of fatigue cycles, as shown in Figures 4.57 to 4.61. Its magnitude, at a stress level, was less than that observed for Type II — out-of-phase tension-torsion loading. The samples also exhibited permanent shear strain at higher load levels and closer to failure. While positive permanent shear strain was noticed at lower loads (Sample 24 and 18), negative permanent shear strain was noticed at higher loads (Samples 19 and 23), suggesting a difference in failure modes.

The reduction in the axial and the shear modulus during fatigue is plotted in Figures 4.32 and 4.33. While the trend observed in axial modulus is similar to the trend observed for uniaxial tensile (Type IV) loading, the reduction in the modulus was rapid and its magnitude much larger than that observed under pure tensile loading. While the magnitude of the reduction in the shear modulus is same for all biaxial

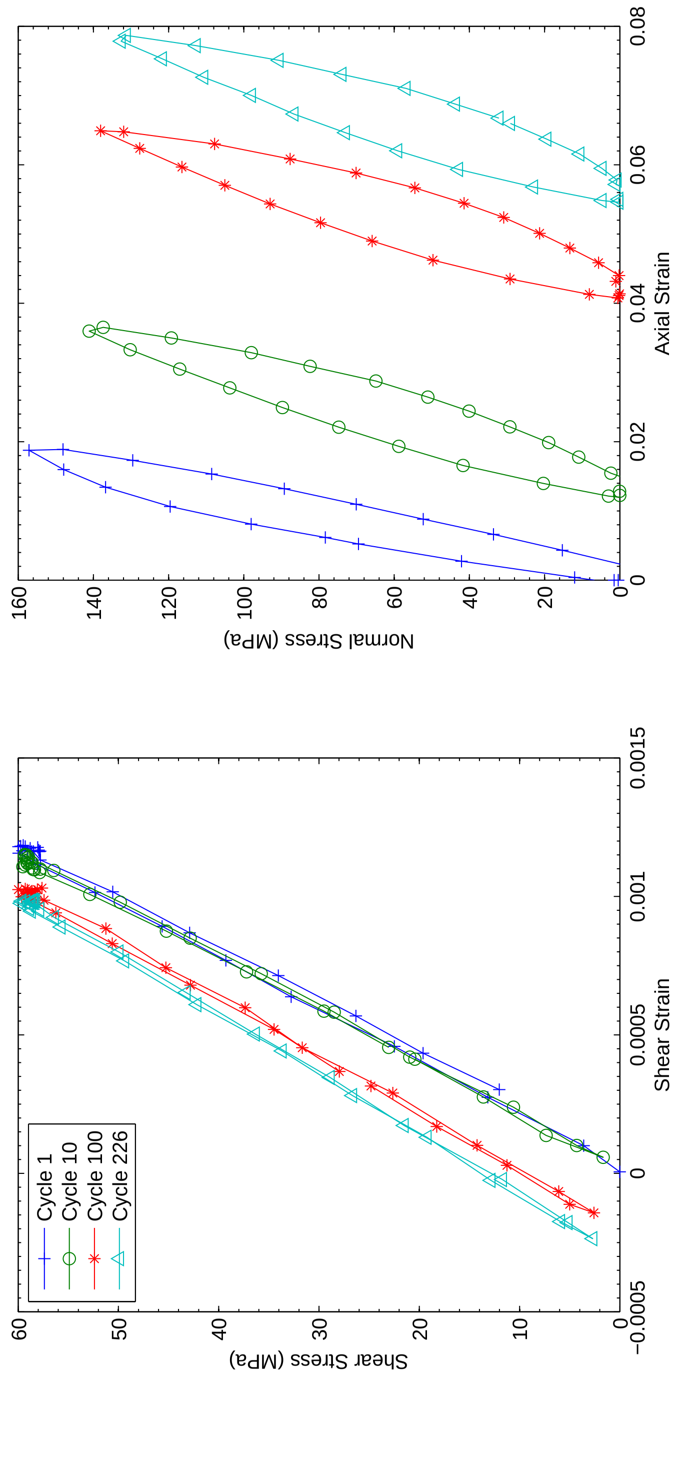

Figure 4.57: Sample 23 (Type III [75% of τ_{yy}^{max} then 75% of σ_{xy}^{max}]) hysteresis

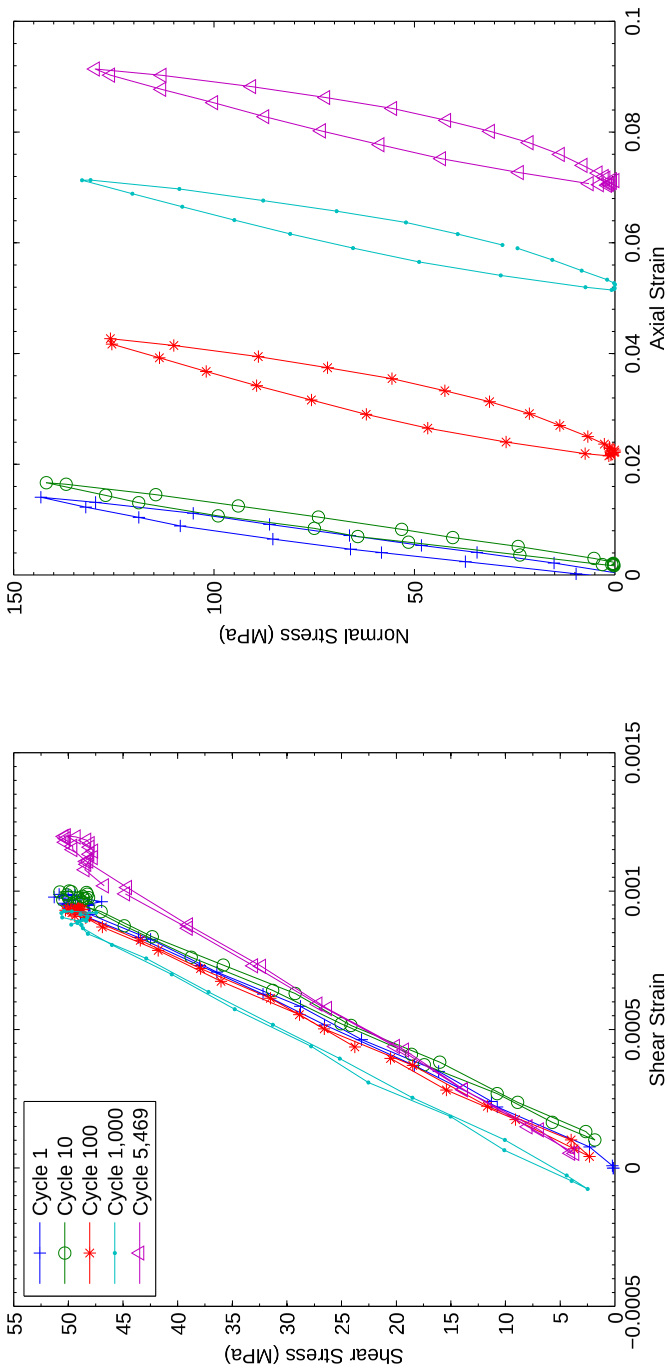

Figure 4.58: Sample 19 (Type III [60% of τ_{yy}^{max} then 60% of σ_{xy}^{max}]) hysteresis

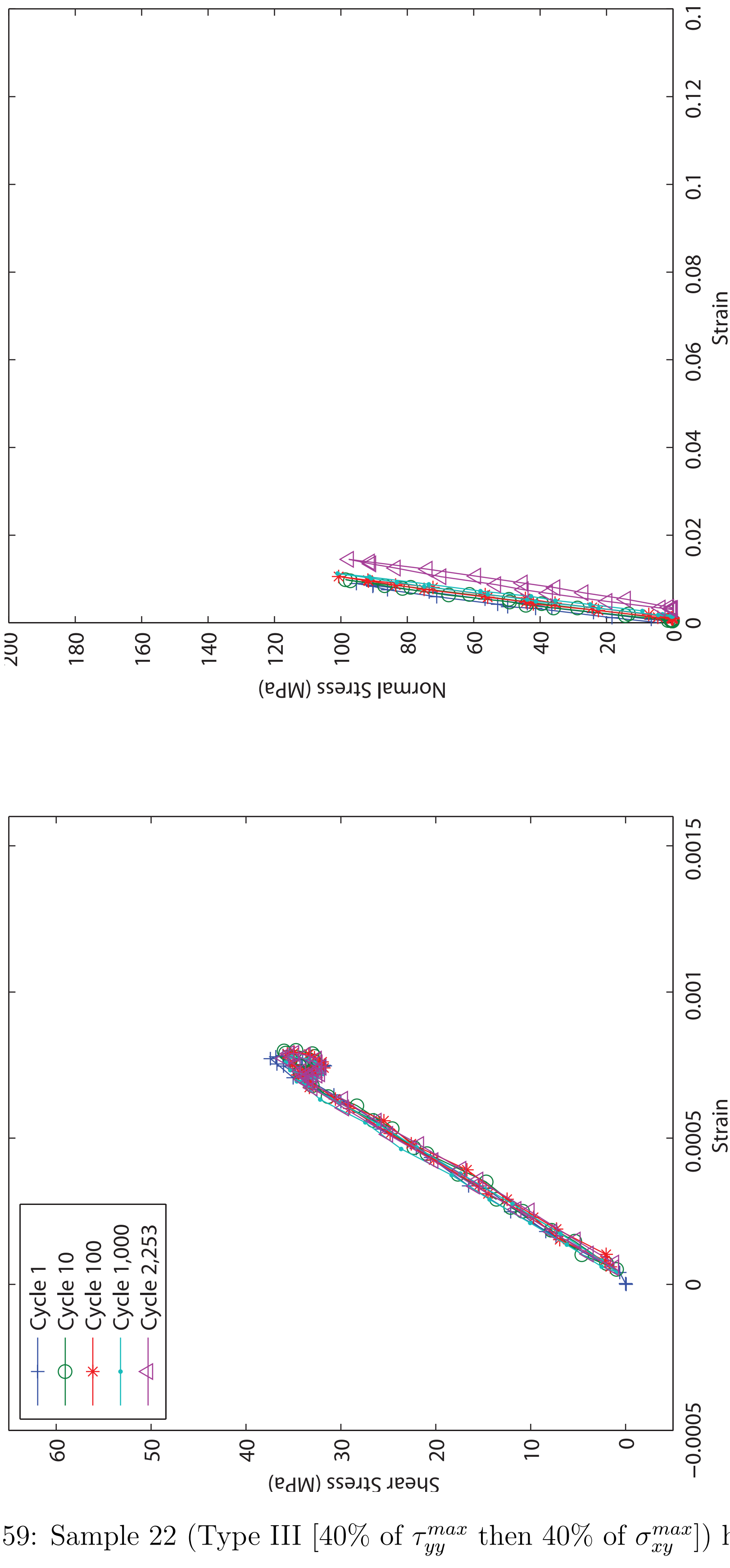

Figure 4.59: Sample 22 (Type III [40% of τ_{yy}^{max} then 40% of σ_{xy}^{max}]) hysteresis

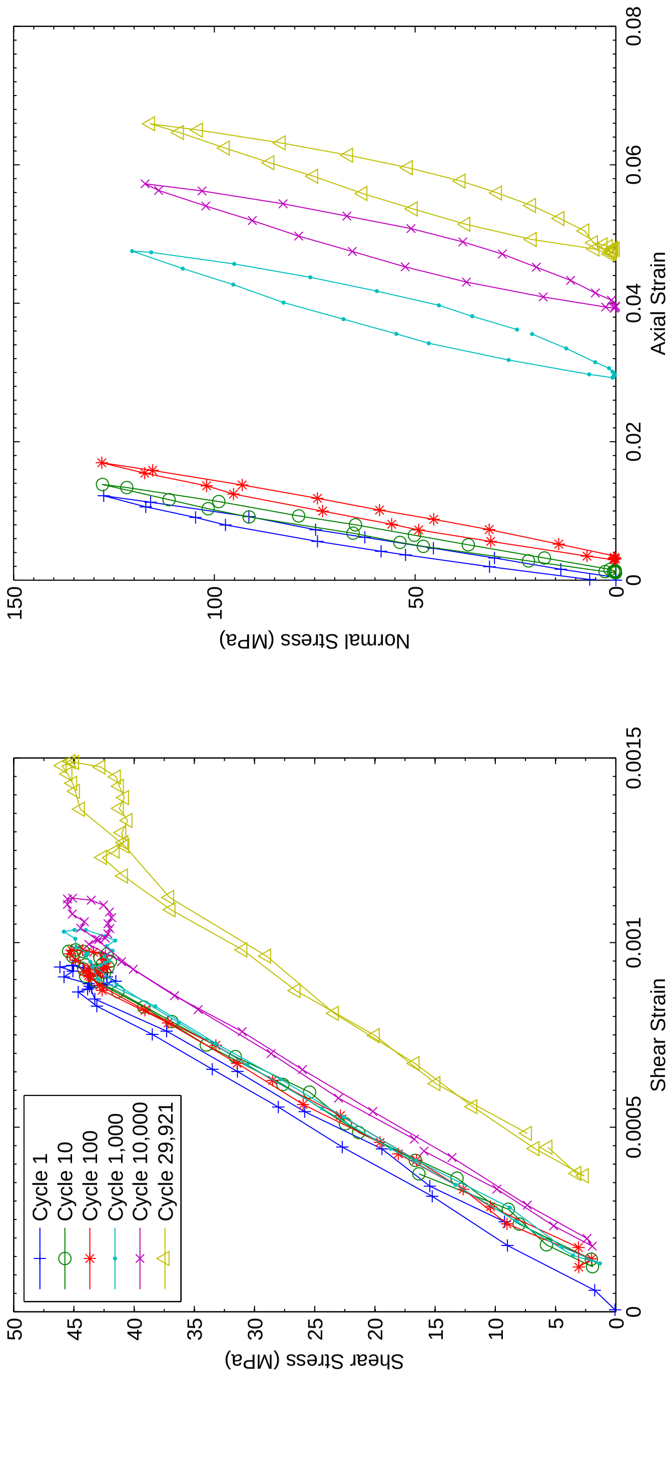

Figure 4.60: Sample 18 (Type III [50% of τ_{yy}^{max} then 50% of σ_{xy}^{max}]) hysteresis

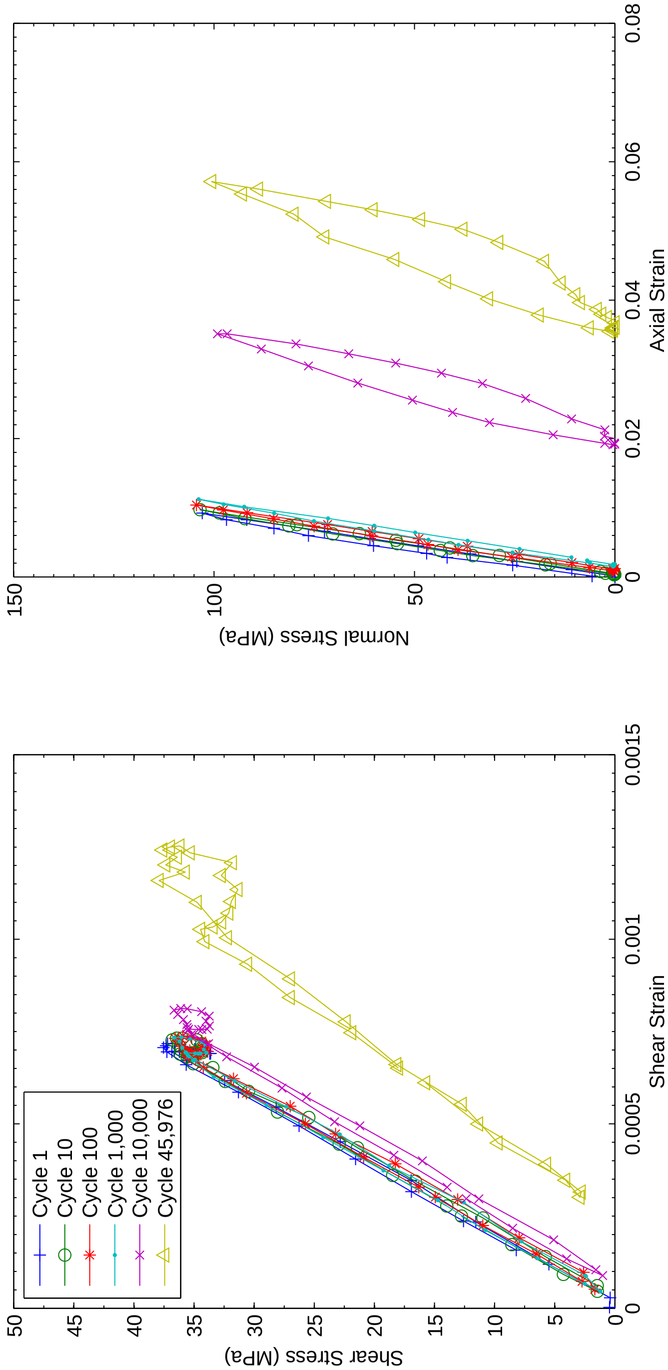

Figure 4.61: Sample 24 (Type III [40% of τ_{yy}^{max} then 40% of σ_{xy}^{max}]) hysteresis

loading types, it occurred rapidly for Type III when compared to Types I and II. These observations suggest a difference in the failure modes.

A photograph of the fractured samples is given in Figure 4.62. The failure pattern observed at lower stress levels (Samples 24, 22, and 18) is similar to that observed for in-phase tensile-torsion (Type I) loading. However, at higher load levels (Samples 19 and 23), the failure pattern is similar to pure torsion loading (Type V) and sample 21 of out-of-phase tension-torsion (Type II) loading. Additionally, pseudo-necking observed in uniaxial tension was also observed at higher loads.

Figure 4.62: Samples failed under out-of-phase torsion-tension fatigue (Type III loading)

These results clearly establish the effect of load path on fatigue behavior of $[\pm 45]_{2s}$ laminate.

4.7 Discussion

The calculated first-ply failure envelope, ABCD, indicated in Figure 3.14, is the stress space within which no failure should occur. If the boundaries of this space are crossed, then first ply failure would occur. It can be inferred from this Figure 3.14 that the first ply of the laminate to fail, under uniaxial tensile loading, would be either [45] or [−45] ply. The predicted failure mode would be in-plane shear that would result in cracks parallel to fibers and is referred to in this thesis as matrix cracks. The laminate load at which this would happen is predicted to be 25 kN (see Figure 3.14), which corresponds to a laminate axial stress of $\sim$ 128 MPa.

It was noted in Section 4.3.1 that the stress-strain curve for the laminate, under uniaxial loading, showed a transition from linear to non-linear behavior beyond 100 MPa. Accordingly, the matrix cracking caused by in-plane shear failure of the plies is believed to be one reason for the non-linearity. The other reason is the non-linearity in the shear response discussed in Section 4.3.1. These matrix cracks were more visible in the inner plies than in the outer [45] ply, which is to be expected since the outer [45] ply has less constraint than the inner plies. The density of these matrix cracks increased with fatigue cycles and stress amplitudes, resulting in the increase of the permanent axial strain observed in Figure 4.37. Other fracture modes, such as limited delamination initiating at these matrix cracks could be observed. The final failure of the laminate, under both quasi-static and fatigue loads, was due to tensile failure of the fiber in both plies, near the grip. Due to the matrix cracking, the Poisson's contraction was never recovered, resulting in pseudo-necking, whose magnitude increased with stress amplitude during uniaxial tensile fatigue in Figure 4.40. Therefore, the initiation and growth of this matrix crack density is believed to have influenced the fatigue life cycle under uniaxial tensile (Type IV) fatigue, observed in Figure 4.31. The reduction in the axial modulus observed in Figure 4.32 is due to this increase in the matrix crack density.

It can be inferred from this Figure 3.14 that the first ply of the laminate to fail, under uniaxial torsional loading, would be [−45] plies under positive torque and [+45] plies under negative torque. The predicted failure mode is longitudinal compressive failure due to compressive failure of the fibers. Since the applied torsion was positive, the [−45] plies are predicted to fail, which was observed during quasi-static and fatigue tests. For example, in Figures 4.13 and 4.51, a crack parallel to fibers in [+45] layers indicates that the fibers in [+45] plies did not fracture. This means the fibers in [−45] plies, which are perpendicular to the fibers in [+45] plies, should have fractured to result in the laminate failure. Note that the samples tested under torsion did not separate into two pieces, which is a typical laminate failure pattern under tensile loading. This suggests that the load bearing capacity of the laminate was suddenly reduced to zero, due to failure of the load-bearing fibers.

The predicted laminate shear stress for the first ply failure by longitudinal compressive failure, under torsional loading, is $\sim$ 697 MPa. However, the laminate failure under quasi-static torsional loading occurred at a laminate shear stress of $\sim$ 325 MPa. Even Tsai-Wu failure criterion allowing for the interaction of stresses, results in a laminate shear stress at failure of $\sim$ 502 MPa. There are three possible reasons for this discrepancy:

One possible reason is process-induced residual stress, due to mismatch in shear CTE between [+45] and [−45] layers and due to the effect of cure shrinkage. Due to lack of information on cure shrinkage for this material, the latter is ignored. Using the CTE of the lamina and a ΔT of $-113°C$ (the difference between the cure temperature of $135°C$ and room temperature of $22°C$), the process-induced residual stress along material directions in [−45] layers has been estimated to be −24 MPa along the longitudinal direction, and +24 MPa along the transverse direction. While the predicted laminate shear stress for first ply failure by longitudinal compressive failure reduces from 697 MPa to 691 MPa, the predicted laminate shear stress for transverse tensile stress reduces from 757 MPa to 303 MPa. If one considers the cure shrinkage, this stress is likely to reduce further. Hence, unlike the prediction shown in Figure 3.14, the first ply failure under torsional loading is likely to be due to transverse tensile failure from tensile transverse residual stress.

A second possible reason is the compressive load introduced in the sample due to rotational-axial coupling discussed in 4.3.2. This is estimated to introduce, in the principal material directions, a longitudinal compressive stress of ~ 35 MPa and a maximum in-plane shear stress of 19 MPa in the [−45] and [+45] plies. These stress levels are not high enough to change the first ply failure by transverse tensile failure, predicted in the previous paragraph.

A third possible reason is the error in the longitudinal compressive strength of −1340 MPa used in the prediction. Unfortunately, this property was not measured as a part of this thesis and was taken from the property data sheet provided by the material supplier. Normally, a huge scatter is observed in the experimentally measured compressive strength due to factors such as error in sample preparation (mis-orientation of the fibers with respect to loading axis), error in testing (lack of appropriate lateral support to prevent buckling), defects in the material (such as fiber waviness and voids), and process-induced residual stress. As well, it is not known whether the fiber volume fraction in the composite used to generate the data is identical to that in the composite used in this thesis. Using the experimental laminate shear strength of ~ 325 MPa, the lamina's longitudinal compressive strength was calculated to be −618 MPa, assuming a first ply failure by this failure mode, which is about 50% of the value used in the prediction.

Accordingly, the process-induced residual stress and possible error in the longitudinal compressive strength are believed to be the reasons for the observed discrepancy between the predicted and the experimental shear strength of the laminate under torsional loading. Based on this, and the failure mode observed in Figure 4.13, it is believed that the damage during uniaxial torsional loading was initiated by transverse tensile failure (i.e. matrix failure) and longitudinal compressive failure (i.e. fiber failure) within [−45] plies, followed by transverse or shear failure in [+45] plies, resulting in the final fracture of the laminate.

During in-phase biaxial tension-torsion testing (Type I), all three samples except Sample 1 were loaded beyond the critical laminate stress of 128 MPa (predicted to initiate the matrix cracks due to in-plane shear) during the first cycle itself. Thus, all these samples registered permanent axial strain after the first fatigue cycle, in Figures 4.37 to 4.39. The simultaneously applied torque would have introduced a residual axial compressive stress due to machine coupling, which would have reduced the overall tensile stress state in the samples. This is believed to be one reason for the slightly better fatigue life observed under Type I biaxial in-phase tension-torsion loading when compared to uniaxial tension (Type IV) loading. Influence of other damage modes such as delamination, as discussed in 4.6.1, is believed to be another contributor. The laminate shear stress, applied simultaneously on Samples 12, 13, and 14, was well below the predicted critical value of 697 MPa and 300 MPa for ply failure by longitudinal compressive failure and transverse tensile failure, respectively. For this reason, these damage modes could not have played a role in the first-ply failure in these samples. Yet, an increase in permanent shear strain with shear stress and fatigue cycles is observed in Figures 4.48 to 4.50. This is believed to be related to the extensive delamination observed in Figure 4.51. Therefore, the interactive role of in-phase shear stress in facilitating the extensive delamination requires further investigation. The gradual decrease in the axial and the shear moduli with fatigue cycles, observed in Figures 4.32 and 4.33, is due to increase in the matrix crack density and delamination.

The axial stress amplitudes applied to the laminate during biaxial out-of-phase tension-torsion (Type II) loading were also beyond the critical value of 128 MPa for the first ply failure by in-plane shear. Even so the applied shear stress amplitudes were much below that for the first ply failure by longitudinal compressive failure or transverse tensile failure. Unlike the samples subjected to Type I loading, discussed in the previous paragraph the samples that failed under Type II loading exhibited negligible delamination. The magnitude of permanent shear strain was much below that observed in Type I loading, supporting the suggestion made in the previous paragraph relating the permanent shear strain with delamination. The pseudo-necking observed in samples in Figure 4.56 suggest that the increase in the matrix crack density, due to in-plane shear failure, is the reason for the observed trend in the axial and the shear moduli, in Figures 4.32 and 4.33. This is similar to the trend observed for uniaxial tensile (Type IV) loading. However, the magnitude of axial permanent strain, for a given stress amplitude, was higher than that recorded for uniaxial tensile fatigue, suggesting a greater extent of damage. This appears to be corroborated by the difference in the failure pattern; while all samples, subjected to Type IV uniaxial tensile fatigue, failed near the grip (see Figure 4.40), the failure surface in samples subjected to Type II loading extended from the grip region towards the gage section with increase in stress amplitude (see Figure 4.56). For example, one half of the Sample 17 in Figure 4.56 exhibits a serrated failure surface, which is indicative of matrix cracking parallel to fibers in one ply group (say [−45] plies) and fiber fracture in another ply group (i.e. [+45] plies. Samples 18 and 21 exhibit matrix cracking and fiber failure on outer [+45] plies, which was not observed in Sample 17 subjected to lower stress levels, as well as in any of the samples subjected to uniaxial fatigue. The fiber failure on the outer [+45] plies observed in Figure 4.56 clearly points to tensile fiber failure.

While the applied out-of-phase shear stress amplitudes did not influence the first-ply failure, it appears to have influenced the subsequent damage progression and final failure, resulting in a fatigue life less than that for uniaxial tensile fatigue. This is in contrast to Type I loading wherein the applied in-phase shear stresses increased the fatigue life with respect to uniaxial tensile fatigue.

The axial stress amplitudes applied to the laminate during biaxial out-of-phase torsion-tension (Type III) loading were below as well as beyond the critical value of 128 MPa for the first ply failure by in-plane shear. However, the applied shear stress amplitudes were much below that for the first ply failure by longitudinal compressive failure or transverse tensile failure. Yet, applying the torsional stresses prior to applying the tensile stresses reduced the fatigue life for a given tensile stress amplitude to a substantially lower value than the fatigue life for the other four types of loading. The drastic degradation of the axial modulus observed in Figure 4.32 suggests a greater extent of damage than observed in other loading types, which appears to have reduced the fatigue life substantially. While the final fracture was concentrated along a single plane at higher loads (Samples 19 and 23 in Figure 4.62), the final fracture plane was relatively diffused over a larger area at lower stress values (Samples 18, 22, and 24 in Figure 4.62). While the axial permanent strain increased with applied tensile stress amplitude similar to Type I loading, it decreased suddenly at 175 MPa. Similarly, while the permanent shear strain increased with stress amplitude, similar to Type I loading, the sign of this shear strain suddenly reversed at higher stresses (Samples 19 and 23 in Figure 4.62). Application of torsion prior to tension appears to have influenced the damage progression and final failure the greatest and the reasons for this are not known.

In summary, the S-N curves for all five loading types are plotted together in Figure 4.31. The fatigue behavior under uniaxial torque is not as well-behaved as the fatigue behavior under other four loading types. This is believed to be a result of the longitudinal compressive failure, which can be influenced by a wide range of factors. While an in-phase torque, superposed on to the tensile load, extended the fatigue life, an out-of-phase torque, superposed onto the tensile load, reduced the fatigue life, with respect to uniaxial fatigue life. An out-of-phase torque applied prior to the tensile load had the most impact on the fatigue life, when compared to the torque applied after the tensile load. These results clearly establish the effect of load path on the fatigue life of composites under biaxial loading. A clear dependence of degradation in axial and shear modulus with load path is observed, which appears to be related to the difference in damage progression and final failure rather than the difference in damage initiation. The damage initiation for Type I to IV loading is through in-plane shear failure of the plies. However, other damage modes such as fiber failure, delamination, and transverse failure are likely to have been introduced during damage progression and final failure. Since the magnitude of shear stresses superposed onto the tensile stresses are less than the critical values for damage initiation through other modes, these stresses are believed to have influenced the damage progression and final failure. The exact role played by these shear stresses as well as the sequence of application of these shear stresses (i.e. load path) on the damage progression and final failure is not understood at this time and requires further investigation.

Chapter 5

Conclusions

The fatigue behavior of thin walled $[\pm 45]_{2s}$ graphite fiber composite tube was experimentally studied at room temperature under uniaxial and biaxial loading. The uniaxial fatigue tests determined the fatigue life of the tubes under various amplitudes of tensile and torsional loads. The biaxial fatigue studies determined the fatigue life of the tubes under various amplitudes of combined tension-torsion loads. While the proportion of tensile to torsional loads was maintained at $118m^{-1}$ (the corresponding ratio of tensile to shear stresses was 3), the loading path was varied by changing the sequence of application of the tensile and torsional loads and the phase difference between them. Type I loading involved in-phase tension-torsion loading. Type II loading involved out-of-phase tension-torsional loads. Type III loading involved out-of-phase torsion-tension loading. All fatigue tests were done at a R ratio of 0 and a frequency of 3 Hz. Damage progression during fatigue was monitored through the degradation, in the axial and the shear modulus of the laminate as well as the permanent axial and shear strains in the laminate, with fatigue cycles. Using this data on damage progression and uniaxial fatigue, the effect of load path on the biaxial fatigue of the chosen composite laminate was evaluated. Therefore, it is concluded that all the four objectives of the thesis, outlined in Section 2.1 have been successfully achieved.

5.1 Summary

A summary of accomplished tasks are presented below:

(1) Quasi-static testing of unidirectional lamina and the $[\pm 45]_{2s}$ laminate was completed to determine the tensile and the shear properties of the lamina and the laminate.

a. The lamina properties were used along with the lamination theory to predict the laminate stress-strain curve, which was compared with experimental results to delineate the critical laminate stress levels above which damage initiates and propagates.

b. These critical stress levels were used to define the fatigue stress amplitudes for uniaxial and biaxial fatigue testing

c. The lamina properties were also used with a maximum stress criterion to define the failure envelope and the first-ply failure modes under tension and torsion, which were subsequently used to interpret the damage progression during fatigue loads

d. The laminate fractured under tensile loading exhibited pseudo-necking that is indicative of damage within the plies of the laminate.

e. The fracture pattern observed in the failed laminate specimens under tensile loading was different from that observed under torsional loading due to difference in failure modes.

f. Axial compressive strain due to torsional loading of the laminate was observed due to machine coupling.

(2) Uniaxial fatigue testing of the tubes under tensile and torsional loading was completed to determine the S-N curve and the damage progression during fatigue.

a. While the fatigue life under tensile fatigue loading increased with decrease in the stress amplitude, the fatigue life under torsional loading did not follow a trend.

b. The axial permanent strain increased with increase in the tensile fatigue load amplitude and the number of fatigue cycles. The axial modulus degraded initially and then subsequently increased to a plateau value, with increase in the number of fatigue cycles. The rate of degradation increased with increase in stress levels. The failed samples exhibited pseudo-necking, the magnitude of which increased with increase in stress amplitude

c. An apparent increase in the shear modulus of the laminate, under shear loading, was observed with increase in the number of fatigue cycles.

d. The failure patterns observed in the failed samples were similar to that observed under quasi-static testing.

(3) Biaxial fatigue testing of the tubes under combined tensile and torsional loading was completed to determine the S-N curve and the damage progression during fatigue. The three loading paths were used.

a. The fatigue life, for a given fatigue stress amplitude, decreased with load path as follows

i. Type I >Type IV>Type II > Type III

It should be noted that the Type IV corresponds to uniaxial tensile fatigue loading while the rest corresponds to biaxial loading.

b. The maximum shear stress used in this test was 1/5th the shear strength of the laminate.

c. Permanent axial and shear strains as well as pseudo-necking were observed in the fractured samples for all load paths. However, their magnitude varied with load amplitude and load path.

d. The degradation in the axial modulus with increase in fatigue cycles was similar for all load paths and was similar to that observed for uniaxial tensile loading. However, the maximum degradation was observed for Type III loading.

e. . A monotonic decrease in the shear modulus with increase in the number of fatigue cycles was observed for all three load paths. However, a marginal increase in the shear modulus , similar to the trend observed in uniaxial torsional loading, was observed during early 10 - 20 cycles.

f. The fracture patterns, observed in the failed samples, differed with load path.

5.2 Final Conclusions

Based on the results detailed in the previous section, the following can be concluded.

(1) While an in-phase torque, superposed on to the tensile load, extended the fatigue life, an out-of-phase torque, superposed onto the tensile load, reduced the fatigue life, with respect to uniaxial fatigue life. An out-of-phase torque applied prior to the tensile load had the most impact on the fatigue life, when compared to the torque applied after the tensile load. These results clearly establish the effect of load path on the fatigue life of composites under biaxial loading.

(2) A clear dependence of degradation in the axial and the shear modulus with load path is observed, which appears to be related to the difference in damage progression and final failure rather than the difference in damage initiation.

(3) The damage initiation for Type I to IV loading is through in-plane shear failure of the plies. However, other damage modes such as fiber failure, delamination, and

transverse failure are likely to have been introduced during damage progression and final failure. Since the magnitude of shear stresses, superposed onto the tensile stresses were less than the critical values for damage initiation through other modes, these stresses are believed to have influenced the damage progression and final failure.

(4) The exact role played by these shear stresses as well as by the sequence of application of these shear stresses (i.e. load path) on the damage progression and final failure is not understood at this time and requires further investigation.

5.3 Recommended Future Work

Any future work should focus on the role played by the superposed shear stresses mentioned in the conclusion point 4 in Section 5.2. Subsequently, this study should be expanded to include other laminate types, since the laminate sequence would determine the First-Ply-Failure Mode as well as the sequence of initiation and growth of various damage modes.

Appendix A

Failure Envelope Calculations

A.1

Determination of Failure Envelope for $[\pm 45]_{2s}$ Laminate

Using the lamina properties given in Section 3.1.2 and the sample geometry shown in Section 3.1.3, the properties were calculated using lamination theory. The laminate was made up of 8 plies with a total thickness of 1.2 mm. These properties were used along with maximum stress failure criteria to determine the failure envelope.

A.1.1 Laminate Properties

To calculate the properties for the laminate we define the following terms: N_x, N_y, and N_{xy} are the forces in the X and Y directions; M_x, M_y, and M_{xy} are the moments in the X and Y directions; ϵ_x°, ϵ_y°, and γ_z° are the strains in the X and Y direction; κ_x, κ_y, and κ_z are the curvatures in the X, Y, and Z planes; and A_{ij}, B_{ij}, and Cij are the stiffness terms. Stress-Strain relation for a laminate, given by lamination theory is:

$$\begin{Bmatrix} N_x \\ N_y \\ N_{xy} \\ M_x \\ M_y \\ M_{xy} \end{Bmatrix} = \begin{bmatrix} \overline{A_{11}} & \overline{A_{12}} & \overline{A_{16}} & \overline{B_{11}} & \overline{B_{12}} & \overline{B_{16}} \\ \overline{A_{12}} & \overline{A_{22}} & \overline{A_{26}} & \overline{B_{12}} & \overline{B_{22}} & \overline{B_{26}} \\ \overline{A_{16}} & \overline{A_{26}} & \overline{A_{66}} & \overline{B_{16}} & \overline{B_{26}} & \overline{B_{66}} \\ \overline{B_{11}} & \overline{B_{12}} & \overline{B_{16}} & \overline{D_{11}} & \overline{D_{12}} & \overline{D_{16}} \\ \overline{B_{12}} & \overline{B_{22}} & \overline{B_{26}} & \overline{D_{12}} & \overline{D_{22}} & \overline{D_{26}} \\ \overline{B_{16}} & \overline{B_{26}} & \overline{B_{66}} & \overline{D_{16}} & \overline{D_{26}} & \overline{D_{66}} \end{bmatrix} \begin{Bmatrix} \epsilon_x^\circ \\ \epsilon_y^\circ \\ \gamma_z^\circ \\ \kappa_x \\ \kappa_y \\ \kappa_z \end{Bmatrix}. \tag{A.1}$$

Assuming that the laminate is symmetric

$$[B] = 0. \tag{A.2}$$

Also, given that the laminate is balanced

$$A_{16} = A_{26} = 0. \tag{A.3}$$

Substituting Equation (A.2) and (A.3) into Equation (A.1) yields

$$\begin{Bmatrix} N_x \\ N_y \\ N_{xy} \\ M_x \\ M_y \\ M_{xy} \end{Bmatrix} = \begin{bmatrix} \overline{A_{11}} & \overline{A_{12}} & 0 & 0 & 0 & 0 \\ \overline{A_{12}} & \overline{A_{22}} & 0 & 0 & 0 & 0 \\ 0 & 0 & \overline{A_{66}} & 0 & 0 & 0 \\ 0 & 0 & 0 & \overline{D_{11}} & \overline{D_{12}} & \overline{D_{16}} \\ 0 & 0 & 0 & \overline{D_{12}} & \overline{D_{22}} & \overline{D_{26}} \\ 0 & 0 & 0 & \overline{D_{16}} & \overline{D_{26}} & \overline{D_{66}} \end{bmatrix} \begin{Bmatrix} \epsilon_x^\circ \\ \epsilon_y^\circ \\ \gamma_z^\circ \\ \kappa_x \\ \kappa_y \\ \kappa_z \end{Bmatrix}. \tag{A.4}$$

Which reduces to

$$\begin{Bmatrix} N_x \\ N_y \\ N_{xy} \end{Bmatrix} = \begin{bmatrix} \overline{A_{11}} & \overline{A_{12}} & 0 \\ \overline{A_{12}} & \overline{A_{22}} & 0 \\ 0 & 0 & \overline{A_{66}} \end{bmatrix} \begin{Bmatrix} \epsilon_x^\circ \\ \epsilon_y^\circ \\ \gamma_{xy}^\circ \end{Bmatrix}, and \tag{A.5}$$

$$\begin{Bmatrix} M_x \\ M_y \\ M_{xy} \end{Bmatrix} = \begin{bmatrix} \overline{D_{11}} & \overline{D_{12}} & \overline{D_{16}} \\ \overline{D_{12}} & \overline{D_{22}} & \overline{D_{26}} \\ \overline{D_{16}} & \overline{D_{26}} & \overline{D_{66}} \end{bmatrix} \begin{Bmatrix} \kappa_x \\ \kappa_y \\ \kappa_{xy} \end{Bmatrix}. \tag{A.6}$$

The analysis is only concerned with loading the samples in tension and shear, and does not include any bending. This results in no curvatures, as in-plane and forces cannot induce curvatures since $[B] = 0$ and no moments are being applied; thus, only the $[A]$ matrix for the laminate needs to be calculated. Given that $\kappa_x = \kappa_y = \kappa_z = 0$ the Kirchhoff hypothesis reduces to

$$\begin{aligned}
\begin{Bmatrix} \epsilon_x \\ \epsilon_y \\ \gamma_{xy} \end{Bmatrix} &= \begin{Bmatrix} \epsilon_x^\circ \\ \epsilon_y^\circ \\ \gamma_z^\circ \end{Bmatrix} + z \begin{Bmatrix} \kappa_x \\ \kappa_y \\ \kappa_{xy} \end{Bmatrix}, \\
\begin{Bmatrix} \epsilon_x \\ \epsilon_y \\ \gamma_{xy} \end{Bmatrix} &= \begin{Bmatrix} \epsilon_x^\circ \\ \epsilon_y^\circ \\ \gamma_z^\circ \end{Bmatrix}.
\end{aligned} \tag{A.7}$$

It is important to note that Equation (A.1) can be inverted to get Equation (A.8)

$$\begin{Bmatrix} \epsilon_x^\circ \\ \epsilon_y^\circ \\ \gamma_z^\circ \\ \kappa_x^\circ \\ \kappa_y^\circ \\ \kappa_z^\circ \end{Bmatrix} = \begin{bmatrix} \overline{a_{11}} & \overline{a_{12}} & \overline{a_{16}} & \overline{b_{11}} & \overline{b_{12}} & \overline{b_{16}} \\ \overline{a_{12}} & \overline{a_{22}} & \overline{a_{26}} & \overline{b_{12}} & \overline{b_{22}} & \overline{b_{26}} \\ \overline{a_{16}} & \overline{a_{26}} & \overline{a_{66}} & \overline{b_{16}} & \overline{b_{26}} & \overline{b_{66}} \\ \overline{b_{11}} & \overline{b_{12}} & \overline{b_{16}} & \overline{d_{11}} & \overline{d_{12}} & \overline{d_{16}} \\ \overline{b_{12}} & \overline{b_{22}} & \overline{b_{26}} & \overline{d_{12}} & \overline{d_{22}} & \overline{d_{26}} \\ \overline{b_{16}} & \overline{b_{26}} & \overline{b_{66}} & \overline{d_{16}} & \overline{d_{26}} & \overline{d_{66}} \end{bmatrix} \begin{Bmatrix} N_x \\ N_y \\ N_{xy} \\ M_x \\ M_{xy} \\ M_y \end{Bmatrix}. \tag{A.8}$$

By the same math Equation (A.5) can be inverted and substituted into Equation (A.7) to get

$$\begin{Bmatrix} \epsilon_x \\ \epsilon_y \\ \gamma_{xy} \end{Bmatrix} = \begin{bmatrix} \overline{a_{11}} & \overline{a_{12}} & 0 \\ \overline{a_{12}} & \overline{a_{22}} & 0 \\ 0 & 0 & \overline{a_{66}} \end{bmatrix} \begin{Bmatrix} N_x \\ N_y \\ N_{xy} \end{Bmatrix}. \tag{A.9}$$

The $[A]$ matrix is calculated from the summation of the stiffness maxtrices, $[\overline{Q}]$ of each ply in the laminate.

$$[A] = \int_{-h_b}^{h_t} [\overline{Q}] dz. \tag{A.10}$$

As the properties of each ply are constant over the thickness, the integral in Equation (A.10) can be evaluated as a summation shown in Equation (A.11)

$$[A] = \sum_{k=1}^{K} [\overline{Q}]_k (z_k - z_{k-1}). \tag{A.11}$$

Assuming that each lamina is in plane stress, the $[\overline{Q}]$ matrix for each ply is calculated using

$$[Q] = \begin{bmatrix} \frac{E_1}{D} & \frac{\nu_{12}E_2}{D} & 0 \\ \frac{\nu_{12}E_2}{D} & \frac{E_2}{D} & 0 \\ 0 & 0 & G_{12} \end{bmatrix}, \text{ where } D = 1 - \frac{E_2}{E_1}\nu_{12}^2. \tag{A.12}$$

The stiffness matrix is calculated for the [0] ply by substituting values from Table 3.1 into Equation (A.12) and with $D = 1 - \frac{E_2}{E_1}\nu_{12}^2 = 0.9972$:

$$[\overline{Q}]^0 = [Q] = \begin{bmatrix} \frac{E_1}{D} & \frac{\nu_{12}E_2}{D} & 0 \\ \frac{\nu_{12}E_2}{D} & \frac{E_2}{D} & 0 \\ 0 & 0 & G_{12} \end{bmatrix} = \begin{bmatrix} 210.63 & 2.25 & 0 \\ 2.25 & 8.03 & 0 \\ 0 & 0 & 3.52 \end{bmatrix} \times 10^9 \frac{N}{m^2}. \tag{A.13}$$

The stiffness matrices for the [+45] and [−45] plies are calculated by transforming stiffness matrix of the [0] degree ply using Equation (A.14)

$$\begin{bmatrix} \overline{Q}_{11} & \overline{Q}_{12} & \overline{Q}_{16} \\ \overline{Q}_{12} & \overline{Q}_{22} & \overline{Q}_{26} \\ \overline{Q}_{16} & \overline{Q}_{26} & \overline{Q}_{66} \end{bmatrix} = [T_\sigma]^{-1} \begin{bmatrix} Q_{11} & Q_{12} & Q_{16} \\ Q_{12} & Q_{22} & Q_{26} \\ Q_{16} & Q_{26} & Q_{66} \end{bmatrix} [T_\epsilon] \tag{A.14}$$

where $[T_\sigma]$ and $[T_\epsilon]$ are given by

$$[T_\sigma] = \begin{bmatrix} c^2 & s^2 & 2cs \\ s^2 & c^2 & -2cs \\ -cs & cs & c^2 - s^2 \end{bmatrix} \quad [T_\epsilon] = \begin{bmatrix} c^2 & s^2 & cs \\ s^2 & c^2 & -cs \\ -2cs & 2cs & c^2 - s^2 \end{bmatrix}, \tag{A.15}$$

and c and s are defined as $c = \cos\Theta, s = \sin\Theta$. Θ is the transformation angle from the positive X axis measured positive counter-clockwise.

The $[\overline{Q}]^{45}$ matrix is calculated as:

$$[\overline{Q}]^{45} = [T_\sigma]^{-1}[\overline{Q}]^0[T_\epsilon] = \begin{bmatrix} 59.31 & 52.27 & 50.65 \\ 52.27 & 59.31 & 50.65 \\ 50.65 & 50.65 & 53.54 \end{bmatrix} \times 10^9 \frac{N}{m^2}. \tag{A.16}$$

The $[\overline{Q}]^{-45}$ matrix is calculated as:

$$[\overline{Q}]^{-45} = [T_\sigma]^{-1}[\overline{Q}]^0[T_\epsilon] = \begin{bmatrix} 59.31 & 52.27 & -50.65 \\ 52.27 & 59.31 & -50.65 \\ -50.65 & -50.65 & 53.54 \end{bmatrix} \times 10^9 \frac{N}{m^2}. \tag{A.17}$$

Thus the A matrix of the $[\pm 45]_{2s}$ laminate can be calculated via Equations (A.11), (A.16), and (A.17) and is given by:

$$[A] = \sum_{k=1}^{n} [\overline{Q}]_k (z_k - z_{k-1}) = \begin{bmatrix} 71.17 & 62.72 & 0 \\ 62.72 & 71.17 & 0 \\ 0 & 0 & 64.25 \end{bmatrix} \times 10^6 \frac{N}{m}. \tag{A.18}$$

Where $n = 8$, and $z_k - z_{k-1} = \frac{t}{n} = \frac{1.2}{8} mm.$

For the $[\pm 45]_{2s}$ laminate using Equation (A.18) in Equation (A.5) defines the force/displacement Equation:

$$\begin{Bmatrix} N_x \\ N_y \\ N_{xy} \end{Bmatrix} = \begin{bmatrix} 71.17 & 62.72 & 0 \\ 62.72 & 71.17 & 0 \\ 0 & 0 & 64.25 \end{bmatrix} \times 10^6 \frac{N}{m} \begin{Bmatrix} \epsilon_x \\ \epsilon_y \\ \gamma_{xy} \end{Bmatrix}. \tag{A.19}$$

Inverting Equation (A.19) yields Equation (A.20) as

$$\begin{Bmatrix} \epsilon_x \\ \epsilon_y \\ \gamma_{xy} \end{Bmatrix} = \begin{bmatrix} 62.92 & -55.45 & 0 \\ -55.45 & 62.92 & 0 \\ 0 & 0 & 15.56 \end{bmatrix} \times 10^{-9} \frac{m}{N} \begin{Bmatrix} N_x \\ N_y \\ N_{xy} \end{Bmatrix}. \tag{A.20}$$

To calculate the effective Young's modulus and shear modulus for the sample, Equations (A.21)-(A.23) are used as:

$$\overline{\sigma}_x = \frac{1}{H} N_x, \tag{A.21}$$

$$\overline{\sigma}_y = \frac{1}{H} N_y, \tag{A.22}$$

$$\overline{\sigma}_z = \frac{1}{H} N_z. \tag{A.23}$$

Solving for N_x, N_y, and N_z from Equations (A.21)-(A.23) and substituting them into Equation (A.9) yields:

$$\begin{Bmatrix} \epsilon_x^\circ \\ \epsilon_y^\circ \\ \gamma_{xy}^\circ \end{Bmatrix} = \begin{bmatrix} \overline{a_{11}}H & \overline{a_{12}}H & 0 \\ \overline{a_{12}}H & \overline{a_{22}}H & 0 \\ 0 & 0 & \overline{a_{66}}H \end{bmatrix} \begin{Bmatrix} \overline{\sigma}_x \\ \overline{\sigma}_y \\ \overline{\sigma}_z \end{Bmatrix}. \tag{A.24}$$

Using the general form of Young's Modulus, $E = \frac{\sigma}{\epsilon}$, it can be seen from Equation (A.24) that:

$$\overline{E}_x = \frac{1}{\overline{a_{11}}H}, \tag{A.25}$$

$$\overline{E}_y = \frac{1}{\overline{a_{22}}H}, \tag{A.26}$$

$$\overline{G}_{xy} = \frac{1}{\overline{a_{66}}H}, \tag{A.27}$$

$$\overline{\nu}_{xy} = -\frac{\overline{a_{12}}}{\overline{a_{11}}}, \tag{A.28}$$

$$\overline{\nu}_{yx} = -\frac{\overline{a_{12}}}{a_{22}}. \tag{A.29}$$

Substituting values from Equation (A.20) into Equations (A.25)-(A.29) yields:

$$\begin{aligned} \overline{E}_x &= \frac{1}{\overline{a_{11}}H} \\ \overline{E}_x &= 13.2GPa \end{aligned}, \tag{A.30}$$

$$\begin{aligned} \overline{E}_y &= \frac{1}{\overline{a_{22}}H} \\ \overline{E}_y &= 13.2GPa \end{aligned}, \tag{A.31}$$

$$\begin{aligned} \overline{G}_{xy} &= \frac{1}{\overline{a_{66}}H} \\ \overline{G}_{xy} &= 53.5GPa \end{aligned}, \tag{A.32}$$

$$\begin{aligned} \overline{\nu}_{xy} &= -\frac{\overline{a_{12}}}{\overline{a_{11}}}, \, and \\ \overline{\nu}_{xy} &= 0.881 \end{aligned} \tag{A.33}$$

$$\begin{aligned} \overline{\nu}_{yx} &= -\frac{\overline{a_{12}}}{\overline{a_{22}}}. \\ \overline{\nu}_{yx} &= 0.881 \end{aligned} \tag{A.34}$$

Note that the samples were tested in tension and torsion only. Thus, during tension testing in the global Y direction E_y and ν_{yx} were measured. However, as the sample was not tested in the hoop direction, i.e. internal pressure, E_x and ν_{xy} were not directly measured. It is noted that the sample is a symmetric cross-ply laminate and that it is expected that $E_x = E_y$ and that $\nu_{xy} = \nu_{yx}$.

A.1.2 Failure Envelope

The maximum load in tension and torsion that the sample can take was determined to select the test parameters. These were determined as follows for a unit tensile load

$$N_x = \frac{1Newton}{2\pi r} = 6.1498\frac{N}{m},$$

using this in Equation (A.20) yields

$$\begin{Bmatrix} \epsilon_x \\ \epsilon_y \\ \gamma_{xy} \end{Bmatrix} = \begin{bmatrix} 62.92 & -55.45 & 0 \\ -55.45 & 62.92 & 0 \\ 0 & 0 & 15.56 \end{bmatrix} \times 10^{-9} \frac{m}{N} \begin{Bmatrix} 6.1498 \\ 0 \\ 0 \end{Bmatrix} \frac{N}{m}$$

$$\begin{Bmatrix} \epsilon_x \\ \epsilon_y \\ \gamma_{xy} \end{Bmatrix} = \begin{Bmatrix} 388.1 \times 10^{-9} \\ -342.1 \times 10^{-9} \\ 0 \end{Bmatrix}. \tag{A.35}$$

For unit torsional load, setting:

$$N_{xy} = \frac{1 Newton \cdot meter}{2\pi r^2} = 239 \frac{N}{m}$$

using this in Equation (A.20) yields

$$\begin{Bmatrix} \epsilon_x \\ \epsilon_y \\ \gamma_{xy} \end{Bmatrix} = \begin{bmatrix} 62.92 & -55.45 & 0 \\ -55.45 & 62.92 & 0 \\ 0 & 0 & 15.56 \end{bmatrix} \times 10^{-9} \frac{m}{N} \begin{Bmatrix} 0 \\ 0 \\ 239 \end{Bmatrix} \frac{N}{m}, or$$

$$\begin{Bmatrix} \epsilon_x \\ \epsilon_y \\ \gamma_{xy} \end{Bmatrix} = \begin{Bmatrix} 0 \\ 0 \\ 3.721 \times 10^{-6} \end{Bmatrix}. \tag{A.36}$$

The global stresses in the [+45] plies due to unit tension load were calculated via Equation (A.37) and subsequently transformed to the material coordinate using Equation (A.38). Note that $[T_\sigma]$ is defined in Equation (A.15):

$$\begin{Bmatrix} \sigma_x \\ \sigma_y \\ \tau_{xy} \end{Bmatrix} = \begin{bmatrix} \overline{Q}_{11} & \overline{Q}_{12} & \overline{Q}_{16} \\ \overline{Q}_{12} & \overline{Q}_{22} & \overline{Q}_{26} \\ \overline{Q}_{16} & \overline{Q}_{26} & \overline{Q}_{66} \end{bmatrix} \begin{Bmatrix} \epsilon_x \\ \epsilon_y \\ \gamma_{xy} \end{Bmatrix}, or \tag{A.37}$$

$$\begin{Bmatrix} \sigma_1 \\ \sigma_2 \\ \tau_{12} \end{Bmatrix} = [T_\sigma] \begin{Bmatrix} \sigma_x \\ \sigma_y \\ \tau_{xy} \end{Bmatrix}. \tag{A.38}$$

For tensile loading, substitution of Equation (A.16) and (A.35) into Equation (A.37) yields

$$\begin{aligned} \begin{Bmatrix} \sigma_x \\ \sigma_y \\ \tau_{xy} \end{Bmatrix}^{45° ply} &= \begin{bmatrix} 59.31 & 52.27 & 50.65 \\ 52.27 & 59.31 & 50.65 \\ 50.65 & 50.65 & 53.54 \end{bmatrix} \times 10^9 \frac{N}{m^2} \begin{Bmatrix} 388.1 \times 10^{-9} \\ -342.1 \times 10^{-9} \\ 0 \end{Bmatrix} \\ \begin{Bmatrix} \sigma_x \\ \sigma_y \\ \tau_{xy} \end{Bmatrix}^{45° ply} &= \begin{Bmatrix} 5141 \\ 0 \\ 2333 \end{Bmatrix} Pa \end{aligned} \tag{A.39}$$

Transforming the global stresses in 45° ply stresses due to the 1 Newton load into material coordinates yields

$$
\begin{aligned}
\begin{Bmatrix} \sigma_1 \\ \sigma_2 \\ \tau_{12} \end{Bmatrix}^{45^\circ ply} &= \begin{bmatrix} 0.5 & 0.5 & 1 \\ 0.5 & 0.5 & -1 \\ -0.5 & 0.5 & 0 \end{bmatrix} \begin{Bmatrix} 5141 \\ 0 \\ 2333 \end{Bmatrix}, or \\
\begin{Bmatrix} \sigma_1 \\ \sigma_2 \\ \tau_{12} \end{Bmatrix}^{45^\circ ply} &= \begin{Bmatrix} 4903 \\ 236 \\ -2571 \end{Bmatrix} Pa
\end{aligned} \tag{A.40}
$$

Equation (A.40) implies that failure will not occur in the material 1 direction (i.e. longitudinal failure) due to the 1 Newton load in the 45° ply if:

$$
\begin{gathered}
S_1^- < 4903P < S_1^+ \\
-1340 \times 10^6 Pa < 4903P < 2920 \times 10^6 Pa \\
-273kN < P < 595kN
\end{gathered} \tag{A.41}
$$

Equation (A.40) implies that failure will not occur in the material 2 direction (i.e. transverse failure) due to the 1 Newton load in the 45° ply if:

$$
\begin{gathered}
S_2^- < 236P < S_2^+ \\
-169 \times 10^6 Pa < 236P < 60 \times 10^6 Pa \\
-716kN < P < 254kN
\end{gathered} \tag{A.42}
$$

From Equation (A.40) failure will not occur in the material 12 direction (i.e. in-plane shear failure) from the 1 Newton load in the 45° ply if:

$$
\begin{gathered}
S_{12}^{-} < -2571P < S_{12}^{+} \\
-70 \times 10^{6}Pa < -2571P < 70 \times 10^{6}Pa \\
27kN > P > -27kN
\end{gathered}
\tag{A.43}
$$

The above equality means that the 45° ply will fail by negative shear if tensile load is applied; it will fail by positive shear if compressive load is applied.

For the 45° ply substituting Equation (A.16) and (A.36) into Equation (A.37) yields:

$$
\begin{aligned}
\begin{Bmatrix} \sigma_x \\ \sigma_y \\ \tau_{xy} \end{Bmatrix}^{45^\circ ply} &= \begin{bmatrix} 59.31 & 52.27 & 50.65 \\ 52.27 & 59.31 & 50.65 \\ 50.65 & 50.65 & 53.54 \end{bmatrix} \times 10^{6}\frac{N}{m} \begin{Bmatrix} 0 \\ 0 \\ 3.721 \times 10^{-6} \end{Bmatrix} \\
\begin{Bmatrix} \sigma_x \\ \sigma_y \\ \tau_{xy} \end{Bmatrix}^{45^\circ ply} &= \begin{Bmatrix} 188487 \\ 188487 \\ 199250 \end{Bmatrix} Pa
\end{aligned}
\tag{A.44}
$$

Transforming the 45° ply stresses from the $1Newton \times meter$ load into material coordinates

$$
\begin{aligned}
\begin{Bmatrix} \sigma_1 \\ \sigma_2 \\ \tau_{12} \end{Bmatrix}^{45^\circ ply} &= \begin{bmatrix} 0.5 & 0.5 & 1 \\ 0.5 & 0.5 & -1 \\ -0.5 & 0.5 & 0 \end{bmatrix} \begin{Bmatrix} 188487 \\ 188487 \\ 199250 \end{Bmatrix} \\
\begin{Bmatrix} \sigma_1 \\ \sigma_2 \\ \tau_{12} \end{Bmatrix}^{45^\circ ply} &= \begin{Bmatrix} 387737 \\ -10764 \\ 0 \end{Bmatrix} Pa
\end{aligned}
\tag{A.45}
$$

Equation (A.45) implies that failure will not occur in the material 1 direction (i.e. longitudinal failure) due to the 1 Newton x meter load in the 45° ply if:

$$
\begin{gathered}
S_1^- < 387737T < S_1^+ \\
-1340 \times 10^6 Pa < 387737T < 2920 \times 10^6 Pa \\
-3456 N \cdot m < T < 7531 N \cdot m
\end{gathered}
\tag{A.46}
$$

Equation (A.40) implies that failure will not occur in the material 2 direction (i.e. transverse failure) due to the 1 Newton x meter load in the 45° ply if:

$$
\begin{gathered}
S_2^- < -10764T < S_2^+ \\
-169 \times 10^6 Pa < -10764T < 60 \times 10^6 Pa \\
15701 N \cdot m > T > -5574 N \cdot m
\end{gathered}
\tag{A.47}
$$

Equation (A.40) implies that failure will not occur in the material 12 direction (i.e. in-plane shear failure) due to the 1 Newton x meter load in the 45° ply if:

$$
\begin{gathered}
S_{12}^{-} < 0T < S_{12}^{+} \\
-70 \times 10^{6} Pa < 0T < 70 \times 10^{6} Pa \\
-\infty N \cdot m < T < \infty N \cdot m
\end{gathered}
\tag{A.48}
$$

Next, the global stresses in the $-45°$ plies due to unit tension load can be calculated using the procedure used for 45° ply. For unit tensile load, substitution of Equation (A.17) and (A.35) into Equation (A.37) yields

$$
\begin{aligned}
\begin{Bmatrix} \sigma_x \\ \sigma_y \\ \tau_{xy} \end{Bmatrix}^{-45° ply} &= \begin{bmatrix} 59.31 & 52.27 & -50.65 \\ 52.27 & 59.31 & -50.65 \\ -50.65 & -50.65 & 53.54 \end{bmatrix} \times 10^{9} \frac{N}{m^2} \begin{Bmatrix} 388.1 \times 10^{-9} \\ -342.1 \times 10^{-9} \\ 0 \end{Bmatrix} \\
\begin{Bmatrix} \sigma_x \\ \sigma_y \\ \tau_{xy} \end{Bmatrix}^{-45° ply} &= \begin{Bmatrix} 5141 \\ 0 \\ -2333 \end{Bmatrix} Pa
\end{aligned}
\tag{A.49}
$$

Transforming the global ply stresses due to the 1 Newton load into material coordinates

$$
\begin{aligned}
\begin{Bmatrix} \sigma_1 \\ \sigma_2 \\ \tau_{12} \end{Bmatrix}^{-45° ply} &= \begin{bmatrix} 0.5 & 0.5 & -1 \\ 0.5 & 0.5 & 1 \\ 0.5 & -0.5 & 0 \end{bmatrix} \begin{Bmatrix} 5141 \\ 0 \\ -2333 \end{Bmatrix} \\
\begin{Bmatrix} \sigma_1 \\ \sigma_2 \\ \tau_{12} \end{Bmatrix}^{-45° ply} &= \begin{Bmatrix} 4903 \\ 236 \\ 2571 \end{Bmatrix} Pa
\end{aligned}
\tag{A.50}
$$

Equation (A.50) implies that failure will not occur in the material 1 direction (i.e. longitudinal failure) due to the 1 Newton load in the $-45°$ ply if:

$$\begin{gathered} S_1^- < 4903P < S_1^+ \\ -1340 \times 10^6 Pa < 4903P < 2920 \times 10^6 Pa \\ -273kN < P < 595kN \end{gathered} \tag{A.51}$$

Equation (A.50) implies that failure will not occur in the material 2 direction (i.e. transverse failure) due to the 1 Newton load in the $-45°$ ply if:

$$\begin{gathered} S_2^- < 236P < S_2^+ \\ -169 \times 10^6 Pa < 236P < 60 \times 10^6 Pa \\ -713kN < P < 253kN \end{gathered} \tag{A.52}$$

Equation (A.50) implies that see that failure will not occur in the material 12 direction (i.e. in-plane shear failure) due to the 1 Newton load in the $-45°$ ply if:

$$\begin{gathered} S_{12}^- < 2570P < S_{12}^+ \\ -70 \times 10^6 Pa < 2553P < 70 \times 10^6 Pa \\ -27kN < P < 27kN \end{gathered} \tag{A.53}$$

For the unit torsional load, substitution of Equations (A.17) and (A.36) into Equation (A.37) yields

$$\begin{Bmatrix} \sigma_x \\ \sigma_y \\ \tau_{xy} \end{Bmatrix}^{-45^\circ ply} = \begin{bmatrix} 59.31 & 52.27 & -50.65 \\ 52.27 & 59.31 & -50.65 \\ -50.65 & -50.65 & 53.54 \end{bmatrix} \times 10^6 \frac{N}{m} \begin{Bmatrix} 0 \\ 0 \\ 3.721 \times 10^{-6} \end{Bmatrix}$$
$$\begin{Bmatrix} \sigma_x \\ \sigma_y \\ \tau_{xy} \end{Bmatrix}^{-45^\circ ply} = \begin{Bmatrix} -188488 \\ -188488 \\ 199250 \end{Bmatrix} Pa \tag{A.54}$$

Transforming the global stresses from the 1 Newton x meter load into material coordinates

$$\begin{Bmatrix} \sigma_1 \\ \sigma_2 \\ \tau_{12} \end{Bmatrix}^{-45^\circ ply} = \begin{bmatrix} 0.5 & 0.5 & -1 \\ 0.5 & 0.5 & 1 \\ 0.5 & -0.5 & 0 \end{bmatrix} \begin{Bmatrix} -188488 \\ -188488 \\ 199250 \end{Bmatrix}$$
$$\begin{Bmatrix} \sigma_1 \\ \sigma_2 \\ \tau_{12} \end{Bmatrix}^{-45^\circ ply} = \begin{Bmatrix} -387737 \\ 10764 \\ 0 \end{Bmatrix} Pa \tag{A.55}$$

Equation (A.55) implies that failure will not occur in the material 1 direction (i.e. longitudinal failure) due to the 1 Newton x meter load in the -45° ply if:

$$\begin{gathered} S_1^- < -387736T < S_1^+ \\ -1340 \times 10^6 Pa < -387736T < 2920 \times 10^6 Pa \\ 3456 N \cdot m > T > -7531 N \cdot m \end{gathered} \tag{A.56}$$

Equation (A.50) implies that failure will not occur in the material 2 direction (i.e.

transverse failure) due to the 1 Newton x meter load in the $-45°$ ply if:

$$\begin{gathered} S_2^- < 10763T < S_2^+ \\ -169 \times 10^6 Pa < 10763T < 60 \times 10^6 Pa \\ -15701 N \cdot m < T < 15701 N \cdot m \end{gathered} \tag{A.57}$$

Equation (A.50) implies that failure will not occur in the material 12 direction (i.e. in-plane shear failure) due to the 1 Newton x meter load in the $-45°$ ply if:

$$\begin{gathered} S_{12}^- < 0T < S_{12}^+ \\ -70 \times 10^6 Pa < 0T < 70 \times 10^6 Pa \\ -\infty N \cdot m < T < \infty N \cdot m \end{gathered} \tag{A.58}$$

A.1.3 Failure Mode and Loads for Uniaxial Loading of $45°$ ply and $-45°$ ply

Noting that all forces will remain positive in our testing.

Equations A.41, A.42, A.43, A.51, A.52, and A.53 suggest that the first ply failure would occur during tension in in the [±45] plies if the load exceeds

$$P > 27\ kN \tag{A.59}$$

The failure will occur by in-plane shear of [±45]; the [+45] ply will fail by negative shear and the [−45] ply will fail by positive shear.

Equations A.46, A.47, A.48, A.56, A.57, and A.58 suggest first ply failure would occur during torsion [−45] ply if the load exceeds:

$$T > 3456 \; Newton \cdot meters \tag{A.60}$$

The failure mode will be by longitudinal compression failure along the fiber direction. It should be noted that final laminate failure will be at loads higher than these. Nevertheless, these were used to determine test loads.

A.1.4 Failure Mode and Loads for Biaxial Loading of 45° ply and -45° ply

[+45] **plies**

Using Equations (A.43) and (A.48), and properties in Table 3.1.

For longitudinal compressive failure, $\sigma = \sigma_1^c$

$$4903P + 387737T = -1340 \times 10^6 Pa \tag{A.61}$$

Where P is in Newtons and T is in Newton x meters.

For longitudinal tensile failure, $\sigma = \sigma_1^t$

$$4903P + 387737T = 2920 \times 10^6 Pa \tag{A.62}$$

For transverse compressive failure, $\sigma = \sigma_2^c$

$$236P - 10764T = -169 \times 10^6 Pa \tag{A.63}$$

For transverse tensile failure, $\sigma = \sigma_2^t$

$$236P - 10764T = 60 \times 10^6 Pa \tag{A.64}$$

For negative shear failure, $\tau_{12} = \tau_{12}^{(-)}$

$$-2571P = -70 \times 10^6 Pa \tag{A.65}$$

For positive shear failure, $\tau_{12} = \tau_{12}^{(+)}$

$$-2571P = 70 \times 10^6 Pa \tag{A.66}$$

[−45] **plies**

Using Equations (A.50) and (A.58), and properties in Table 3.1.

For longitudinal compressive failure, $\sigma = \sigma_1^c$

$$4903P - 387737T = -1340 \times 10^6 Pa \tag{A.67}$$

Where P is in Newtons and T is in Newton x meters.

For longitudinal tensile failure, $\sigma = \sigma_1^t$

$$4903P - 387737T = 2920 \times 10^6 Pa \tag{A.68}$$

For transverse compressive failure, $\sigma = \sigma_2^c$

$$236P + 10764T = -169 \times 10^6 Pa \tag{A.69}$$

For transverse tensile failure, $\sigma = \sigma_2^t$

$$236P + 10764T = 60 \times 10^6 Pa \tag{A.70}$$

For negative shear failure, $\tau_{12} = \tau_{12}^{(-)}$

$$2571P = -70 \times 10^6 Pa \tag{A.71}$$

For positive shear failure, $\tau_{12} = \tau_{12}^{(+)}$

$$2571P = 70 \times 10^6 Pa \tag{A.72}$$

Using Equations (A.61)–(A.72) failure envelopes were generated and are used in Chapters 3 and 4.

Appendix B

Incremental Load Analysis

The incremental analysis was used to determine stress-strain behavior of the laminate to highlight the evolution of damage in the laminate during quasi-static loading. This incremental analysis determines strain in the laminate for a given applied load, which is incremented in steps, using lamination theory, lamina properties and assuming no damage in the plies. Incremental analysis was used since the shear modulus of the lamina was a function of strain. The steps of this analysis are discussed below.

Step 1 Read lamina properties, ply layup, ply thickness, Load increment (N)

Step 2 Initialize load per unit width, Ni(n=0), Aij(n=0), aij (n=0), ij(n=0) to be zero. Here i=x,y,s and n is the counter for load increments.

Step 3 Determine laminate stress

$\sigma_i(n) = \frac{N_i}{\text{Laminate thickness}}$

Step 4 Determine laminate compliance for the chosen laminate sequence

$A_{ij}(n) = \sum_{k=1}^{n} Q_{ij}(n)t_k$

$a_{ij}(n) = A_{ij}(n)^{-1}$

Step 5 Determine laminate strain $\begin{Bmatrix} \epsilon_x(n) \\ \epsilon_y(n) \\ \gamma_{xy}(n) \end{Bmatrix} = \begin{bmatrix} a_{xx}(n) & a_{xy}(n) & 0 \\ a_{xy}(n) & a_{yy}(n) & 0 \\ 0 & 0 & a_{ss}(n) \end{bmatrix} \begin{Bmatrix} N_x(n) \\ N_y(n) \\ N_s(n) \end{Bmatrix}$

Step 6 Is Ni(n) = N desired?

If No, $N_i(n+1) = N_i(n) + \Delta N$

If yes, output the stress and strain.

The load increment used in this analysis was calculated to provide a stress increment of 1 MPa.

Bibliography

[1] R. Talreja, "Damage and fatigue in composites - a personal account," *Composites Science and Technology*, vol. 68, no. 13, pp. 2585–2591, 2008.

[2] J. Sen, "Influence of a tension load on laminates under torsion," *Journal of the American Helicopter Society*, vol. 40, no. 4, pp. 71–78, 1995.

[3] T. Ogasawara, K. Onta, S. Ogihara, T. Yokozeki, and E. Hara, "Torsion fatigue behavior of unidirectional carbon/epoxy and glass/epoxy composites," *Composite Structures*, vol. 90, no. 4, pp. 482–489, 2009.

[4] M. A. Wafa, A. H. Hamdy, and A. A. El-Midany, "Combined bending and torsional fatigue of woven roving grp," *Journal of Engineering Materials and Technology*, vol. 119, no. 2, pp. 180–187, 1997.

[5] A. Inoue, T. Fujii, and H. Kawakami, "Effect of loading path on mechanical response of a glass fabric composite at low cyclic fatigue under tension/torsion biaxial loading," *Journal of Reinforced Plastics and Composites*, vol. 19, pp. 111–123, 2000.

[6] A. S. D7078, "Standard test method for shear properties of composite materials by v-notched rail shear method," 2005.

[7] T. Fujii and T. Shiina, "Fatigue notch sensitivity of glass woven fabric composites having a circular hole under tension/torsion biaxial loading," *Journal of Composite Materials*, vol. 28, no. 3, pp. 234–251, 1994.

[8] M. Quaresimin, L. Susmel, and R. Talreja, "Fatigue behaviour and life assessment of composite laminates under multiaxial loadings," *International Journal of Fatigue*, vol. 32, no. 1, pp. 2–16, 2010.

[9] C. K. H. Dharan, *Fatigue failure mechanisms in a unidirectionally reinforced composite material*, pp. 171–188. Philadelphia: American Society for Testing and Materials, 1975.

[10] R. Talreja, "Fatigue of composite materials: damage mechanisms and fatigue life diagrams," in *Proc Roy Soc Lond*, vol. A378, pp. 461–475, 1981.

[11] R. Talreja, "A continuum mechanics characterization of damage in composite materials," *Proc Roy Soc Lond*, vol. A399, pp. 355–375, 1985.

[12] J. Aveston, G. Cooper, and A. Kelly, *Single and multiple fracture.*, pp. 15–26. Guilford, Surrey: IPC Sci and Tech Press, 1971.

[13] D. Krajcinoc, "Continuous damage mechanics," *Appl Mech Rev*, vol. 37, pp. 1–5, 1984.

[14] T. Ogasawara, T. Yokozeki, K. Onta, and S. Ogihara, "Linear and nonlinear torsional behavior of unidirectional cfrp and gfrp," *Composites Science and Technology*, vol. 67, no. 15-16, pp. 3457–3464, 2007.

[15] T. Ogasawara, K. Onta, S. Ogihara, and T. Yokozeki, "Tension/torsion behavior of unidirectional cfrp and gfrp," in *AIAA/ASME/ASCE/AHS Structures, Structural Dynamics, and Materials Conference*, vol. 8, 2007.

[16] F. Ellyin, K. Golos, and Z. Xia, "In-phase and out-of-phase multiaxial fatigue," *Journal of Engineering Materials and Technology*, vol. 113, no. 1, pp. 112–118, 1991.

[17] T. Fujii and F. Lin, "Fatigue behavior of a plain-woven glass fabric laminate under tension/torsion biaxial loading," *Journal of Composite Materials*, vol. 29, no. 5, pp. 573–590, 1995.

[18] Z. Hashin and A. Rotem, "A fatigue failure criterion for fibre reinforced materials," *Journal of Composite Materials*, vol. 7, no. 448–464, 1973.

[19] E. H. and F. Ellyin, "Effect of stress ratio on the fatigue of unidirectional fiberglass-epoxy composite laminae," *Composites*, vol. 25, no. 10, pp. 917–24, 1994.

[20] Z. Fawaz and F. Ellyin, "Fatigue failure model for fibre-reinforced materials under general loading conditions," *Journal of Composite Materials*, vol. 28, no. 15, pp. 1432–1451, 1994.

[21] E. W. Smith and K. J. Pascoe, *Biaxial Fatigue of a Glass-Fibre Reinforced Composite, Part 1: Fatigue and Fracture Behaviour*, pp. 367–396. London: Mechanical Engineering Publications, 1989.

[22] I. De Baere, W. Van Paepegem, and J. Degrieck, "Electrical resistance measurement for in situ monitoring of fatigue of carbon fabric composites," *International Journal of Fatigue*, vol. 32, no. 1, pp. 197–207, 2010.

[23] W. Van Paepegem, I. De Baere, E. Lamkanfi, and J. Degrieck, "Monitoring quasi-static and cyclic fatigue damage in fibre-reinforced plastics by Poisson's ratio evolution," *International Journal of Fatigue*, vol. 32, no. 1, pp. 184–196, 2010.

[24] S. Amijima, T. Fujii, and T. Sagami, "Nonlinear behavior of plain woven gfrp under repeated biaxial tension/torsion loading," *Journal of Energy Resources Technology*, vol. 113, no. 4, pp. 235–240, 1991.

[25] T. Fujii, S. Amijima, L. Fan, and T. Sagami, "Study on strength and nonlinear stress-strain response of plain woven glass fiber laminates under biaxial loading," *Journal of Composite Materials*, vol. 26, no. 17, pp. 2493–2510, 1992.

[26] E. K. Krempl and T. M. Niu, "Graphite/epoxy $[\pm 45]_s$ tubes. their static axial and shear properties and their fatigue behavior under completely reversed load controlled loading," *Journal of Composite Materials*, vol. 16, no. 3, pp. 172–187, 1982.

[27] E. K. Krempl, D. Elzey, B. Hog, and T. Ayar, "Uniaxial and biaxial fatiuge properties of thin-walled composite tubes," *Journal of the American Helicopter Society*, vol. 33, no. 3, pp. 3–10, 1988.

[28] P. H. Francis, D. E. Walrath, D. F. Sims, and D. N. Weed, "Biaxial fatigue loading of notched composites," *Journal of Composite Materials*, vol. 11, no. 4, pp. 488–501, 1977.

[29] A. Vicario and R. Rizzo, "Effect of length on laminated thin tubes under combined loading," *Journal of Composite Materials*, vol. 4, no. 2, pp. 273–277, 1970.

[30] N. Pagano and J. M. Whitney, "Geometric design of composite cylindrical characterization specimens," *Journal of Composite Materials*, vol. 4, pp. 360–378, 1970.

[31] A. S. D3039, "Standard test method for tensile properties of polymer matrix composite materials," 2008.

[32] I. C. Engineering, "Ice - company information." http://innovativecomposite.com/company-information. Accessed: 2013-07-11.

[33] Instron, Norwood, MA, *Instron 8800 Materials Test Control System*, m21-10011-en ed., 1998.

[34] Instron, Norwood, MA, *Fast Track 2 Software User Manual*, m22-11133-en ed., 1999.

[35] GOM mbH, "Aramis - optical 3d deformation analysis." http://www.gom.com/metrology-systems/system-overview/aramis.html. Accessed: 2013-07-11.

[36] U. D. of Defense, *MIL-HDBK-17-2F Composites Materials HandBook: Volume 2. Polymer Matrix Composites Materials Properties*. United States Government, 2002.

[37] C. T. Herakovich, *Mechanics of Fibrous Composites*. New York: John Wiley & Sons, Inc., 1998.

[38] J. M. Whitney, G. C. Grimes, and P. H. Francis, "Effect of end attachment on the strength of fiber-reinforced composite cylinders," May 23–26 1972.